DISSERTATION
SUBMITTED TO THE
COMBINED FACULTIES FOR THE NATURAL SCIENCES AND FOR MATHEMATICS
OF THE RUPERTO-CAROLA UNIVERSITY OF HEIDELBERG, GERMANY
FOR THE DEGREE OF
DOCTOR OF NATURAL SCIENCES

Put forward by

Diplom-Ingenieur:	Gregor Kasieczka
Born in:	Wels, Austria

Oral examination: May 2, 2013

SEARCH FOR RESONANCES DECAYING INTO TOP QUARK PAIRS USING FULLY HADRONIC DECAYS IN pp COLLISIONS WITH ATLAS AT $\sqrt{\mathbf{s}} = 7\,\mathrm{TeV}$

Referees:

Prof. Dr. André Schöning

Prof. Dr. Tilman Plehn

Kurzfassung

Eine Suche nach neuen Teilchen welche zu Top-Quarks zerfallen und dabei zwei schwere *Jets* mit hohen Transversalimpulsen erzeugen wird vorgestellt. Für diese Analyse werden Daten, aufgenommen mit dem ATLAS Detektor am Large Hadron Collider während der Proton-Proton Kollisionen bei $\sqrt{\mathbf{s}} = 7\,\mathrm{TeV}$ im Jahr 2011, verwendet.

Um von Top-Quarks stammende Jets von solchen zu unterscheiden, die von leichten Quarks oder Gluonen initiiert wurden, wird der substruktur-basierte HEPTopTagger Algorithmus verwendet. Die Leistungsfähigkeit dieser Methode wird mithilfe eines statistisch unabhängigen Datensatzes validiert. Zur weiteren Unterdrückung von Untergründen wird der Nachweis eines dem Top-Quark-Kandidaten zugeordneten Bottom-Quark-Zerfalls verlangt. Die Untergründe werden unter Benutzung der gemessenen Daten abgeschätzt.

In der invarianten Massverteilung des Di-Top-Quark Systems wird keine signifikante Abweichung zwischen Daten und der Summe der vom Standard Modell vorhergesagten Untergrundprozesse — wie zum Beispiel $t\bar{t}$- oder Multijet-Ereignissen — beobachtet. Es ist daher möglich Grenzwerte auf das Produkt aus Wirkungsquerschnitt und Verzweigungsverhältnis für bestimmte Modelle von Z'-Bosonen und Kaluza-Klein-Gluonen zu bestimmen. Die Erzeugung von Z'-Bosonen mit einer Masse zwischen 0.70 und 1.00 TeV sowie zwischen 1.28 und 1.32 TeV und Kaluza-Klein-Gluonen mit Massen zwischen 0.70 und 1.48 TeV wird mit 95% C.L. ausgeschlossen.

Abstract

A search for new particles that decay into top-quark pairs producing two massive jets with high transverse momentum is presented. Data collected with the ATLAS detector at the Large Hadron Collider during the proton-proton collision run at $\sqrt{\mathbf{s}} = 7\,\mathrm{TeV}$ in 2011 is analysed.

The substructure-based HEPTopTagger technique is used to separate top-quark jets from those arising from light quarks or gluons. The performance of this method is evaluated using a statistically independent sample. Top-quark candidates are also required to have a bottom-quark decay associated with them. The backgrounds are estimated using data-driven techniques.

No significant deviation between data and the sum of Standard Model background processes, such as $t\bar{t}$ production and multijet production, is observed in the di-top invariant mass spectrum $m_{t\bar{t}}$. Therefore limits on the production cross section times branching fractions of certain models of Z' boson and a Kaluza-Klein gluon resonances are set. The production of Z' bosons with masses between 0.70 and 1.00 TeV as well as 1.28 and 1.32 TeV and Kaluza-Klein gluons with masses between 0.70 and 1.48 TeV is excluded at 95% C.L.

Contents

Chapter 1

Introduction

The Standard Model [1–4] summarizes our current understanding of the fundamental laws governing physical processes at the smallest scales. It describes how elementary particles interact via the electromagnetic, weak and strong forces. Its constituents are two different specii of particles: fermions — the building blocks of matter, namely leptons (like the electron) and quarks (like the up and down quark which form the proton); and bosons — mediators of forces (the photon, the heavy W and Z boson and gluons) as well as the Higgs boson.

The structure of interactions in the Standard Model is governed by mathematical symmetry laws. At energies above $\approx 100\,\mathrm{GeV}$ (the electroweak scale) the interactions of electrically neutral photons and Z bosons and charged W bosons can be described in a unified fashion. However, the photon is massless whereas the Z boson is very masssive: this indicates that the symmetry is broken. According to our current understanding the breaking of electroweak symmetry is achieved by the Higgs mechanism [5–7] which also predicts a Higgs boson.

Over the last decades, overwhelming evidence has been collected in support of the Standard Model. Recent examples include the discovery of previously predicted particles such as a Higgs-like boson in 2012 [8, 9], the τ neutrino in 2000 [10] and the top quark in 1995 [11, 12]. Additional credibility is provided by the good agreement observed in precision tests of the electroweak sector [13, 14]. However, as our understanding deepens, it becomes clear that the Standard Model is incomplete.

Some shortcomings of the Standard Model are interesting because they are intrinsically connected to the largest scales of nature. The Standard Model cannot account for the observed baryon asymmetry in the universe (why is there more matter than antimatter?) or explain the origins of dark matter. Some issues are more subtle: the hierarchy problem (the apparent fine tuning that stabilizes the mass of the Higgs boson at the electroweak scale) or the large number of free parameters (such as particle masses and couplings) are philosophically unstatisfactory. And some are more speculative: are there additional symmetries or space-time dimensions which can only be accessed at higher energies?

The top quark[1] is the heaviest particle in the Standard Model and, because of its

---

[1] In the following "top quark" stands for both the top quark and its anti-particle.

mass of $\approx 172\,\mathrm{GeV}$ [15] at the electroweak scale, is expected to play an important role in a deeper understanding of electroweak symmetry breaking. Top quarks have a very short lifetime of $\approx 5 \cdot 10^{-25}\,\mathrm{s}$ and almost exclusively decay into a b quark and a W boson. The W boson can then either decay into two quarks (hadronic decay) or a charged lepton and a neutrino (leptonic decay). As a large fraction of the higher-order corrections to the Higgs-boson mass is due to the top quark, it is natural to assume that possible solutions to the hierarchy problem will involve the top quark. Many models of new physics beyond the Standard Model predict resonances with masses at the TeV scale decaying primarily into top-quark pairs. A detailed account of the Standard Model as well as selected models beyond the Standard Model is given in Section 2.

The Large Hadron Collider [16] (LHC) was designed to gain understanding on all open points of the Standard Model and to lead to a more fundamental theory of nature. This is done by colliding beams of protons (or heavy ions) at unprecedentedly high energies and rates and analyzing the resulting decay particles using particle detectors. The LHC is described in Section 3.

The two large multi-purpose experiments at the LHC are the ATLAS [17] and CMS [18] detectors. The design of such an experiment comprises an inner layer of silicon pixel and silicon microstrip detectors immeresed in a strong magnetic field for the determination of the postition of the interaction vertices and the measurement of charged particle tracks. Further outwards a hermetic calorimter is built with the purpose of stopping particles (except muons and neutrinos) and measuring their energy in the process. The outermost layer provides a dedicated muon tracking system. The ATLAS detector, used for this measurement, is introduced in greater detail in Section 4.

Decays of strongly interacting particles lead to collimated showers — called jets — consisting mostly of light hadrons, electrons and photons that are measured with the calorimeters. Jet reconstruction is an algorithmic problem — how to cluster the discrete measurements in the calorimeter so that the energy and direction of the original particle that initated the shower is best approximated? In recent years progress has been made on understanding jet clustering algorithms and calibrations in greater detail. Performance studies that supported the upgrade to modern jet algorithms in the ATLAS trigger system are documented in Section 5.

The quality of reconstruction can be improved by extracting additional information from jets. Different particles — gluons, light quarks or top quarks — will produce different kinds of showers and therefore a detailed study of the clustering process or substructure of jets can be used for particle identification [19]. A novel method to identify hadronically decaying top quarks and to reconstruct their four-momentum is the HEPTopTagger [20, 21] algorithm. This method tests the substructure of a jet reconstructed with the Cambridge/Aachen (C/A) algorithm [22] with a large distance parameter $R = 1.5$ (“fat jets”) for its compatibility with a hadronic top-quark decay. The algorithm is also designed to be robust against the effects of multiple interactions per bunch-crossing. Studies of the performance of the HEPTopTagger algorithm using LHC collision events recorded with the ATLAS detector in 2011 are presented in Section 6.

Due to the reasons discussed above, the search for heavy resonances in the $t\bar{t}$ invariant mass spectrum is interesting. Such resonances will lead to top quarks with a high transverse momentum (p_{T}). Three different final states are possible: di-leptonic (both intermediate W bosons decay leptonically), lepton+jets (one W boson decays leptonically, the other hadronically) and fully hadronic (both W bosons decay hadronically).

In the di-leptonic channel backgrounds can be well surpressed by requiring two isolated leptons. However the branching fraction into this final state is low and, due to the two neutrinos escaping detection, the reconstruction of the invariant mass is difficult. In the semi-leptonic channel these problems are less pronounced, but the collimation of top-quark decay products at high transverse momenta can make the reconstruction difficult as the lepton is no longer isolated. Searches in the fully hadronic channel obviously do not require isolated leptons and benefit from the higher branching fraction. The main challenge of this channel is the surpression of large backgrounds from QCD multijet production.

A search in the fully hadronic final state — also published in Ref. [23] — is presented in Section 7. For top quarks with a p_{T} above 200 GeV the decay products of each top quark are collimated and can be reconstructed as one jet with a large invariant mass. A combination of b-tagging and the HEPTopTagger algorithm is used to reduce the backgrounds. Two specific models that predict resonances with narrow and broad decay widths Γ are considered: leptophobic topcolor Z' bosons and Kaluza–Klein (KK) gluons from a bulk Randall–Sundrum model (RS) [24–26].

Chapter 2

Theory

Before presenting the results of a search for new particles we will briefly survey the current state of theory. We begin with a review of the Standard Model (SM) in Sec. 2.1 and the physics of proton-proton collisions in Sec. 2.2. Despite its extraordinary success the Standard Model has some shortcomings: these — together with new models designed to correct them — are discussed in Sec. 2.3. There, special attention is given to models providing resonances decaying to top-quark pairs. Since the analysis will focus on fully hadronic final states, the basics of jet physics are explained in Sec. 2.4 and a technique for the reconstruction of hadronically decaying top quarks, the HEPTopTagger algorithm, is presented in Sec. 2.5. Finally, the necessary tools for statistical analysis of the data are summarized in Sec. 2.6.

2.1 Standard Model

The Standard Model (SM) [1–4] is a quantum field theory that summarizes our understanding of the interactions of elementary particles. Three of the four known fundamental forces (the electromagnetic, weak and strong forces) are explained by the SM. The Lagrangian is invariant under transformation of the group $\mathrm{SU(3)_C} \times \mathrm{SU(2)_L} \times \mathrm{U(1)_Y}$. However, the ground state is only symmetric under $SU(2)_\mathrm{L} \times U(1)_\mathrm{QED}$ transformations. Here $\mathrm{SU(3)_C}$, $\mathrm{SU(2)_L}$, $\mathrm{U(1)_Y}$ and $U(1)_\mathrm{QED}$ are the gauge groups of strong interactions, the weak isospin, the hypercharge and of quantum electrodynamics (QED), respectively. The description of the SM follows Refs. [27, 28].

2.1.1 Particle Content

Two different kinds of particles are included in the SM. Mediators of interactions — bosons — and elementary particles of matter — fermions. The bosonic sector consists of the massless photon and eight gluons — responsible for the electromagnetic and strong interaction respectively — and the massive W^+, W^- and Z bosons which mediate the weak interaction. The Higgs boson is an excitation of the Higgs field which gives masses to the other particles [5–7]. The fermionic sector consists of three generations of quarks and leptons:

$$\begin{bmatrix} \nu_e & u \\ e^- & d \end{bmatrix}, \begin{bmatrix} \nu_\mu & c \\ \mu^- & s \end{bmatrix}, \begin{bmatrix} \nu_\tau & t \\ \tau^- & b \end{bmatrix}$$

where the matter content of each generation equals:

$$\begin{bmatrix} \nu_l & q_u \\ l^- & q_d \end{bmatrix} \equiv \begin{pmatrix} \nu_l \\ l^- \end{pmatrix}_{\mathrm{L}}, \begin{pmatrix} q_u \\ q_d \end{pmatrix}_{\mathrm{L}}, l^-_{\mathrm{R}}, q_{u\mathrm{R}}, q_{d\mathrm{R}}$$

corresponding to the left-handed SU(2) weak isospin doublets for leptons and quarks and the right-handed singlets for the charged lepton and up- (q_u) as well as down-type (q_d) quarks . Up-type quarks are up, charm and top; down-type quarks are down, stange and bottom. The weak isospin T of the doublet is $\frac{1}{2}$, with a value of $T_3 = +(-)\frac{1}{2}$ for the upper (lower) component. The isospin of the singlet is zero. For each fermion the anti-particle — which carries the opposite additive quantum numbers — is contained in the SM and quarks exist with three different color charges. Particles at the same position but of different generations, like the electron and the muon, transform identically under gauge transformations but have different masses and flavor quantum numbers. The electrical charges of the fermions are:

$$\begin{aligned} Q(\nu) &= 0 \\ Q(l^-) &= -1 \\ Q(q_U) &= +\frac{2}{3} \\ Q(q_d) &= -\frac{1}{3} \end{aligned}$$

where all charges are given in multiples of the elementary charge. The elementary charge is the electric charge of a proton: $e \approx 1.602 \cdot 10^{-19}$ C. The weak hypercharge Y_W is an additional, conserved quantum number. It can be expressed as

$$Y_W = 2(Q - T_3)$$

with the third component of the weak isospin T_3. Y_W corresponds to the $U(1)$ gauge symmetry.

2.1.2 Gauge Principle

Before going into the details of the Lagrangian density of the SM, it will be useful to review how the principle of gauge invariance leads to the Lagrangian of QED. We start with the Lagrangian for a free electron of mass m:

$$\mathscr{L}_0 = i\overline{\psi}\gamma^\mu \partial_\mu \psi - m\overline{\psi}\psi$$

where the field depends on the four-dimensional space-time position: $\psi \equiv \psi(x)$. The Dirac matrices γ^μ in the Dirac basis are defined as:

$$\gamma^0 = \begin{pmatrix} \mathbb{1}_2 & 0 \\ 0 & \mathbb{1}_2 \end{pmatrix}, \gamma^k = \begin{pmatrix} 0 & \sigma^k \\ -\sigma^k & 0 \end{pmatrix}$$

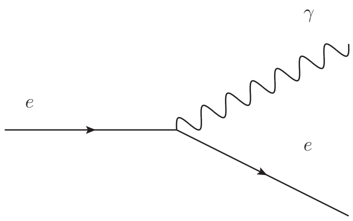

Figure 2.1: Feynman diagram showing the coupling of electrons and photons.

for $k = 1, 2, 3$ with the Pauli matrices σ^k. This Lagrangian is invariant under global U(1) transformations:

$$\psi \to \psi' \equiv e^{iQ\theta}\psi$$

where θ is the transformation parameter and Q an additional, arbitrary, charge. If the transformation is local instead of global, i.e. $\theta \to \theta(x)$, then $\mathscr{L}_0$ will no longer be invariant because of terms involving the derivative of the field:

$$\partial_\mu\psi \to e^{eQ\theta}(\partial_\mu + iQ\partial_\mu\theta)\psi.$$

Restoring the invariance also under local transformations is possible by adding a new (gauge) field (A_μ) to $\mathscr{L}_0$ which is required to transform as:

$$A_\mu \to A'_\mu \equiv A_\mu - \frac{1}{e}\partial_\mu\theta.$$

This field is used to define the covariant derivative through the so-called minimal coupling:

$$D_\mu \equiv \partial_\mu + ieQA_\mu$$

which transforms as the field does. Replacing the partial derivative with the covariant derivative in $\mathscr{L}_0$ yields a Lagrangian invariant under local U(1) transformations:

$$\mathscr{L} \equiv i\overline{\psi}\gamma^\mu D_\mu\psi - m\overline{\psi}\psi.$$

The difference $\mathscr{L}_0 - \mathscr{L} = eQA_\mu\overline{\psi}\gamma^\mu\psi$ represents the interaction between the electron and the gauge field. The Feynman diagram is shown in Fig. 2.1. The only ingredient missing with respect to the complete Lagrangian of QED is the kinetic term for the new field which is given by

$$\mathscr{L}_{\text{Kin}} \equiv -\frac{1}{4}F_{\mu\nu}F^{\mu\nu},$$

where $F_{\mu\nu} \equiv \partial_\mu A_\nu - \partial_\nu A_\mu$ is the electromagnetic field strength tensor. A mass term proportional to $A_\mu A^\mu$ for the gauge field is forbidden by gauge invariance and therefore the photon is expected to be massless. This agrees very well with the experimental observation of $m_\gamma < 1 \cdot 10^{-18}\,\text{eV}$ [15].

2.1.3 Electroweak Interactions

The Lagrangian for the electroweak (EW) sector of the SM will necessarily be more complicated: it has to accommodate the interactions of the heavy gauge bosons in addition to the photon. An important experimental input is that the left- and right-handed fermion chiralities interact differently with the heavy gauge bosons. These states are obtained by applying the helicity projectors L and R:

$$L \equiv \frac{1}{2}(1-\gamma^5),\ R \equiv \frac{1}{2}(1+\gamma^5),$$

with the properties

$$L^2 = L,\ R^2 = R,\ RL = 0,\ R + L = 1,$$

and

$$\gamma^5 = i\gamma^0\gamma^1\gamma^2\gamma^3$$

to the fermion fields. Only left-handed fermions and right-handed anti-fermions couple to the W boson as these are the only weak isospin-doublets. The coupling strength of the W boson is universal. The Z couples to Y_W and therefore differently to left-handed and right-handed fields and not to right-handed neutrinos (because $Q = 0$ and $T_3 = 0$ implies $Y_W = 0$).

The simplest group that fulfills these requirements is $\mathrm{SU(2)_L \times U(1)_Y}$. As the gauge structure is repeated for each generation of leptons and quarks it suffices to look at three fields:

$$\psi_1 \equiv \begin{pmatrix} u \\ d \end{pmatrix}_{\mathrm{L}}, \psi_2 \equiv u_{\mathrm{R}}, \psi_3 \equiv d_{\mathrm{R}}.$$

With the substitutions $u \leftrightarrow \nu_e$ and $d \leftrightarrow e^-$ the above can also represent the leptonic fields. The free Lagrangian can then be written in analogy to the QED Lagrangian as:

$$\mathscr{L}_0 = \sum_{j=1}^{3} i\overline{\psi_j}\gamma^\mu\partial_\mu\psi_j$$

and is invariant under the global transformations in flavor space:

$$\begin{aligned} \psi_1 &\to \psi_1' \equiv e^{iy_1\beta}U_{\mathrm{L}}\psi_1, \\ \psi_2 &\to \psi_2' \equiv e^{iy_2\beta}\psi_2, \\ \psi_3 &\to \psi_3' \equiv e^{iy_3\beta}\psi_3. \end{aligned}$$

The free constants y_i $(i = 1, 2, 3)$ are called — analogous to QED — hypercharges. The $\mathrm{SU(2)_L}$ transformation acts only on the doublet ψ_1 and is defined in terms of the Pauli matrices σ_i as

$$U_{\mathrm{L}} \equiv e^{i\frac{\sigma_i}{2}\alpha^i}.$$

If we require that $\mathscr{L}_0$ is also invariant under local gauge transformations $\alpha \to \alpha(x)$ and $\beta \to \beta(x)$ the partial derivatives have to be replaced with the covariant derivatives:

$$D_\mu\psi_1 \equiv (\partial_\mu + ig\widetilde{W}_\mu + ig'y_1B_\mu)\psi_1,$$

$$D_\mu\psi_2 \equiv (\partial_\mu + ig'y_2B_\mu)\psi_2,$$

$$D_\mu\psi_3 \equiv (\partial_\mu + ig'y_3B_\mu)\psi_2$$

with

$$\widetilde{W_\mu} \equiv \frac{\sigma_i}{2}W_\mu^i = \frac{1}{2}\begin{pmatrix} W_\mu^3 & \sqrt{2}W_\mu^\dagger \\ \sqrt{2}W_\mu & -W_\mu^3 \end{pmatrix}$$

where $W_\mu \equiv \frac{W_\mu^1+iW_\mu^2}{\sqrt{2}}$.

Because there are four free gauge parameters (α^i and β), four gauge fields are needed in the covariant derivative. To make sure that the covariant derivative transforms as the fermion field does, the transformations of the gauge fields need to be set to:

$$B_\mu \to B'_\mu \equiv B_\mu - \frac{1}{g'}\partial_\mu\beta,$$

$$\widetilde{W_\mu} \to \widetilde{W'_\mu} \equiv U_\mathrm{L}\widetilde{W_\mu}U_\mathrm{L}^\dagger + \frac{i}{g}\partial_\mu U_\mathrm{L}U_\mathrm{L}^\dagger.$$

The hypercharges y_i are, as in QED, completely arbitrary. The non-abelian nature of the SU(2) group allows only one coupling constant g which will give rise to the universal coupling of fermions and leptons to the weak gauge bosons.

The Lagrangian

$$\mathscr{L} = \sum_{j=1}^{3} i\overline{\psi_j}\gamma^\mu D_\mu\psi_j$$

has been made invariant under local gauge transformations. The kinetic field strength tensors can be defined as:

$$B_{\mu\nu} \equiv \partial_\mu B_\nu - \partial_\nu B_\mu$$

and

$$\widetilde{W_{\mu\nu}} \equiv \partial_\mu\widetilde{W_\nu} - \partial_\nu\widetilde{W_\mu} + ig[W_\mu, W_\nu].$$

This leads to the kinetic Lagrangian:

$$\mathscr{L}_\mathrm{Kin} = -\frac{1}{4}B_{\mu\nu}B^{\mu\nu} - \frac{1}{2}\,\mathrm{Tr}[\widetilde{W_{\mu\nu}}\widetilde{W^{\mu\nu}}].$$

This Lagrangian also contains higher powers of the gauge fields which implies a self-coupling of the gauge fields. Some examples for interactions among gauge fields are presented in Fig. 2.2. The two neutral gauge fields B_μ and W_μ^3 cannot be directly identified with the photon and the Z boson but are a mixture of these states:

$$\begin{pmatrix} Z_\mu \\ A_\mu \end{pmatrix} \equiv \begin{pmatrix} \cos\theta_W & -\sin\theta_W \\ \sin\theta_W & \cos\theta_W \end{pmatrix}\begin{pmatrix} W_\mu^3 \\ B_\mu \end{pmatrix},$$

where θ_W is the Weinberg angle with $\sin^2\theta_W \approx 0.2312$ [15].

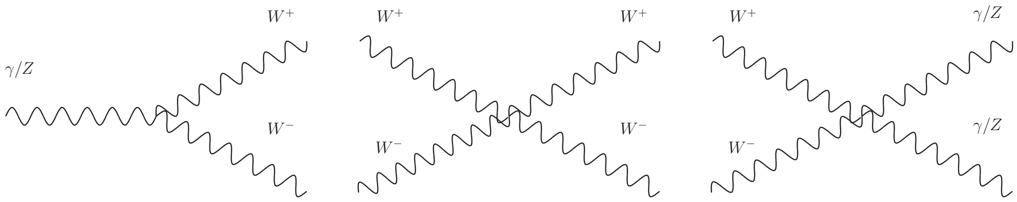

Figure 2.2: Examples of Feynman diagrams for the self-interaction of Gauge bosons.

2.1.4 Spontaneous Symmetry Breaking

The SM Lagrangian derived so far includes all the necessary particles and weak interactions but no masses are assigned to either fermions or bosons. Masses can be included via the mechanism of spontaneous symmetry breaking: the Lagrangian is symmetric under transformations of a group G but the vacuum is not.

This mechanism can be most easily understood for a complex scalar field ϕ. The Lagrangian

$$\mathscr{L} = \partial_\mu \phi^\dagger \partial^\mu \phi - \mu^2 \phi^\dagger \phi - \lambda(\phi^\dagger \phi)^2,$$

with a mass term μ and a positive quartic coupling λ, is invariant under phase transformations of ϕ. If $\mu^2 > 0$ only the trivial vacuum at $\phi = 0$ exists. For $\mu^2 < 0$ there exists an infinite number of states ϕ_0 with minimal energy:

$$|\phi_0| = \sqrt{\frac{-\mu^2}{2\lambda}} \equiv \frac{v}{\sqrt{2}},\ \phi_0 = \frac{v}{\sqrt{2}} e^{i\theta}.$$

The potential for the field is illustrated in Fig. 2.3. Choosing a specific value (for example $\theta = 0$) as the ground state of the theory spontaneously breaks the symmetry. The other states can then be parametrized around ϕ_0 as

$$\phi = \frac{1}{\sqrt{2}}(v + \varphi_1 + i\varphi_2)$$

with the real fields φ_1 and φ_2. Inserting these into the Lagrangian yields:

$$\mathscr{L} = \frac{1}{2}\partial_\mu(\varphi_1 - i\varphi_2)\partial^\mu(\varphi_1 + i\varphi_2) - \mu^2\phi_0^2 - \lambda\phi_0^4 + \mu^2\varphi_1^2 - \lambda v \varphi_1(\varphi_1^2 + \varphi_2^2) - \frac{\lambda}{4}(\varphi_1^2 + \varphi_2^2)^2.$$

The masses of the fields φ_1 and φ_2 can be calculated as

$$m_{\varphi_1}^2 = -\left.\frac{\partial^2}{\partial \varphi_1^2}\mathscr{L}\right|_{\varphi_1 = \varphi_2 = 0} = -2\mu^2$$

and

$$m_{\varphi_2}^2 = -\left.\frac{\partial^2}{\partial \varphi_2^2}\mathscr{L}\right|_{\varphi_1 = \varphi_2 = 0} = 0.$$

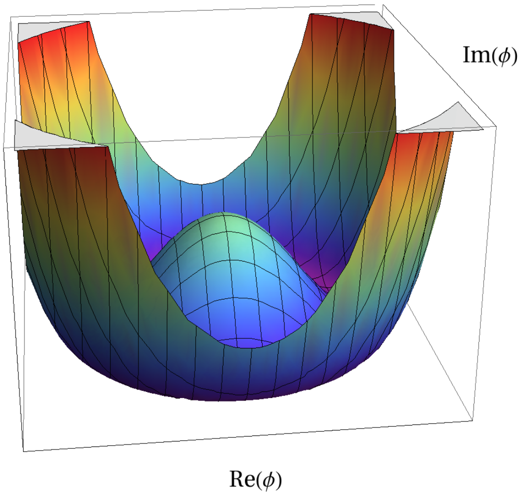

Figure 2.3: Shape of the potential for Higgs field as a function of the real and imaginary component of the field φ.

The field φ_1 acquires a mass whereas the field φ_2 is massless. This result is more generally known as the Goldstone theorem [29]: When a Lagrangian is invariant under transformations of a group G, but the ground state is only invariant under a sub-group $H \subset G$ then there will exist a mass-less spin-0 boson (Goldstone boson) for each generator in G which does not belong to H.

2.1.5 Higgs Mechanism

Next we will show that in the case of local-gauge symmetries the Goldstone bosons give masses to the gauge fields. Starting with an SU(2) doublet of complex scalar fields:

$$\phi \equiv \begin{pmatrix} \phi^{(+)} \\ \phi^{(0)} \end{pmatrix}.$$

The Lagrangian is then:

$$\mathscr{L}_S = (D_\mu\phi)^\dagger D^\mu\phi - \mu^2\phi^\dagger\phi - \lambda(\phi^\dagger\phi)^2$$

with the covariant derivative

$$D^\mu\phi = (\partial^\mu + ig\widetilde{W}^\mu + ig' y_\phi B^\mu)\phi,$$

where $y_\phi = \frac{1}{2}$ is chosen to give the correct couplings between ϕ and the photon field. Again requiring $\lambda > 0$ and $\mu^2 < 0$ yields an infinite number of degenerate states with minimal energy. By choosing a ground state it is possible to spontaneously break $\mathrm{SU(2)_L \times U(1)_Y}$ so that only $\mathrm{U(1)_{QED}}$ remains. After parametrising the fields as

$$\phi = e^{i\frac{\sigma_i}{2}\theta^i(x)}\frac{1}{\sqrt{2}}\begin{pmatrix} 0 \\ v + H(x) \end{pmatrix},$$

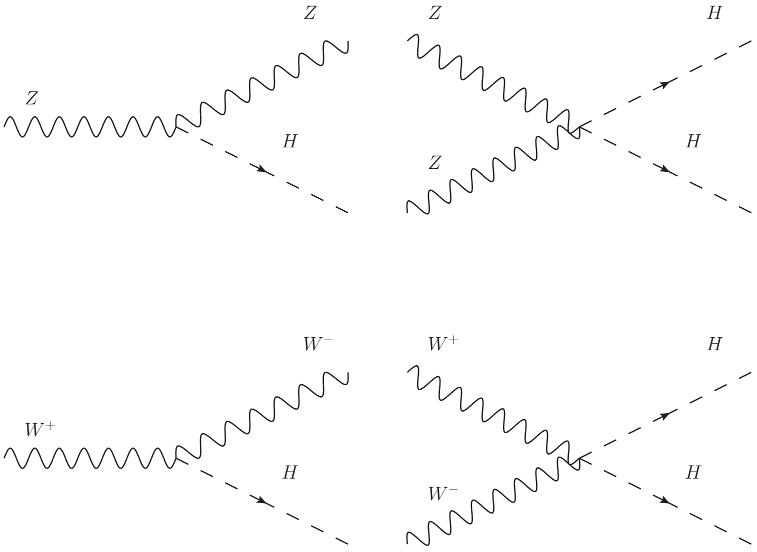

Figure 2.4: Feynman diagrams showing the coupling between the Higgs boson and gauge bosons.

the local gauge freedom can then be used to set $\theta^i(x) \to 0$ which yields:

$$\phi = \frac{1}{\sqrt{2}} \begin{pmatrix} 0 \\ v + H(x) \end{pmatrix}.$$

With this the kinetic part of the Lagrangian reads:

$$(D_\mu \phi)^\dagger D^\mu \phi = \frac{1}{2} \partial_\mu H \partial^\mu H + (v + H)^2 \left(\frac{g^2}{4} W_\mu^\dagger W^\mu + \frac{g^2}{8 \cos^2 \theta_W} Z_\mu Z^\mu \right).$$

This leads to interactions between the gauge bosons and the Higgs boson which are shown in Fig. 2.4. The masses of the W and Z boson can be read off as:

$$M_Z \cos \theta_W = M_W = \frac{1}{2} v g.$$

The measured mass of the W (Z) boson is 80.385 ± 0.015 GeV (91.1876 ± 0.0021 GeV).

It is not possible to directly add a fermion mass term $m\psi\overline{\psi}$ to the Lagrangian because it would mix left- and right-handed states and break the SU(2) gauge symmetry. Adding an interaction between fermions and the Higgs boson (Yukawa coupling) circumvents this problem and leads to (after spontaneous symmetry breaking):

$$\mathscr{L}_Y = -\frac{1}{\sqrt{2}} (v + H)(c_f f \overline{f})$$

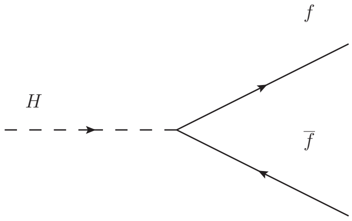

Figure 2.5: Feynman diagram showing the coupling of the Higgs boson to fermions.

which gives fermion masses proportional to the Yukawa coupling constant c_f and the vacuum expectation value of the Higgs field:

$$m_f = c_f \frac{v}{\sqrt{2}}.$$

The c_f are independent parameters and can be different for all fermions. The interaction of fermions with the Higgs boson is illustrated in in Fig. 2.5.

So far no conclusive evidence for the existence of the Higgs boson has been found. However in 2012 a *Higgs like* particle has been measured with a mass of $m_H \approx 125\,\text{GeV}$ [8, 9]. Identification of this particle with the Higgs boson will only be possible after more detailed measurements of its coupling to other particles have been performed.

2.1.6 Strong Interactions

The fundamental theory of strong interactions is quantum chromodynamics (QCD) [30–33]. The large number of hadronic resonances observed so far can be explained by the quark model. There exist six different flavors of quarks: up (u), charm (c), and top (t) quarks (up-type quarks) and down (d), strange (s) and bottom (b) quarks (down-type quarks). Quarks (anti-quarks) have a baryon number $\mathcal{B}$ of $\frac{1}{3}$ ($-\frac{1}{3}$). The up and down quark form an (strong) isospin doublet (with the third component of the isospin $I_Z = -\frac{1}{2}$ for d and $I_Z = \frac{1}{2}$ for u). This is possible because the masses of the up and down quark are very close. The other quarks form singlet states. There are four additional additive quantum numbers associated with the different flavors:

- strangeness $S = -1$ for the s quark;
- charm $C = +1$ for the c quark;
- bottomness $B = -1$ for the b quark;
- topness $T = 1$ for the t quark and
- zero for all other quarks.

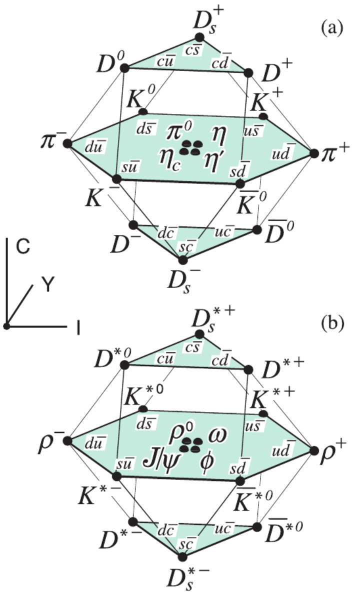

Figure 2.6: Diagram of (a) the pseudoscalar and (b) the vector meson multiplet. The meson states are arranged by their charm C, isospin I and hypercharge $Y = S + \mathcal{B} - \frac{C}{3}$ quantum numbers [15].

The extended Gell-Mann-Nishijima formula can be used to calculate the electric charge (Q) as a function of the other quantum numbers:

$$Q = I_z + \frac{\mathcal{B} + S + C + B + T}{2}.$$

All observed hadrons — mesons and baryons — consist of quarks and gluons.

Mesons are bound states of a quark and an anti-quark (of possibly different flavor) with a total baryon number $\mathcal{B} = 0$. The eigenvalues of the parity P, meson spin J and charge conjugation C operators for mesons are given by

$$\begin{aligned} P &= (-1)^{l+1} \\ |l-s| \leq & J \leq |l+s| \\ C &= (-1)^{l+s} \end{aligned}$$

where l is the orbital angular momentum and $s = 1$ ($s = 0$) implies parallel (anti-parallel) quark spins. Mesons are then classified in J^{PC} states such as the $l = 0$ pseudoscalar (0^{-+}) and vector (1^{--}) states as well as the $l = 1$ scalar (0^{++}), axial vector (1^{++} and 1^{+-}) and tensor (2^{++}) states. Using the flavor symmetry group $\mathrm{SU}(3)_F$ of u, d and s quarks, meson states for theses quarks can be constructed. The inclusion of the heavier c quark is also possible by extending the group to a (broken) SU(4) symmetry. The pseudoscalar and vector meson SU(4) multiplets are shown in Figure 2.6.

Baryons are bound states with $\mathcal{B} = 1$ and all baryons observed so far consist of three quarks. These too can be arranged in SU(n) multiplets. Figure 2.7 shows two examples:

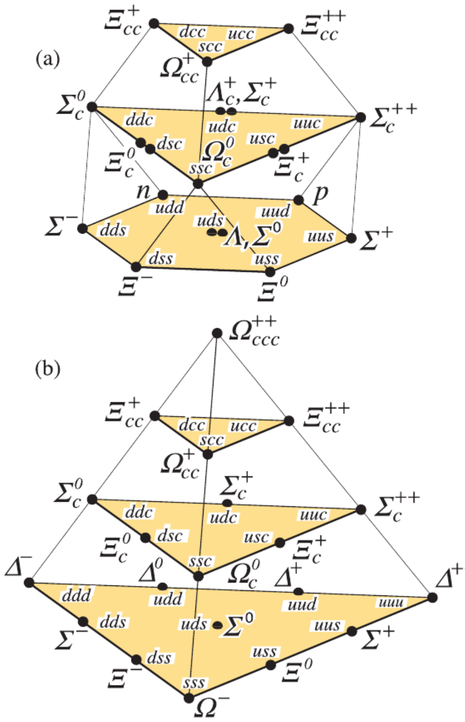

Figure 2.7: Diagram of the 20-plet containing (a) the $J^P = \frac{1}{2}^+$ octet and (b) the $J^P = \frac{3}{2}^+$ decuplet for baryon states made from u, d, s and c quarks [15].

the SU(4) multiplet containing with the $J^P = \frac{1}{2}^+$ octet as a base and the multiplet with the $J^P = \frac{3}{2}^+$ decuplet as base.

Quarks have an additional quantum number: the color charge. Historically this additional charge was first needed to explain [34, 35] the existence of the Δ^{++} particle (shown in the upper-right corner of the decuplet in Fig. 2.7b). A fermion, comprised of three up quarks with parallel spins and no relative angular momentum would violate the Pauli principle. Introducing three different color charges solves this problem because the otherwise symmetric wave-function can be made asymmetric in color-space. The ratio

$$R \equiv \frac{\sigma(e^+e^- \to \text{hadrons})}{\sigma(e^+e^- \to \mu^+\mu^-)}$$

is sensitive to the number of colors which determines the number of hadronic final states:

$$R \approx N_C \sum_{f=1}^{N_f} Q_f^2 = \begin{cases} \frac{2}{3} N_C = 2, (N_f = 3 : u, d, s) \\ \frac{10}{9} N_C = \frac{10}{3}, (N_f = 4 : u, d, s, c) \\ \frac{11}{9} N_C = \frac{11}{3}, (N_f = 5 : u, d, s, c, b) \end{cases}$$

where N_C is the number of colors, N_f the number of flavors and Q_f is the electric charge of the quark f. The agreement between data and the prediction using a simple quark model, as shown in Fig. 2.8, is very good. The Feynman diagram for the process

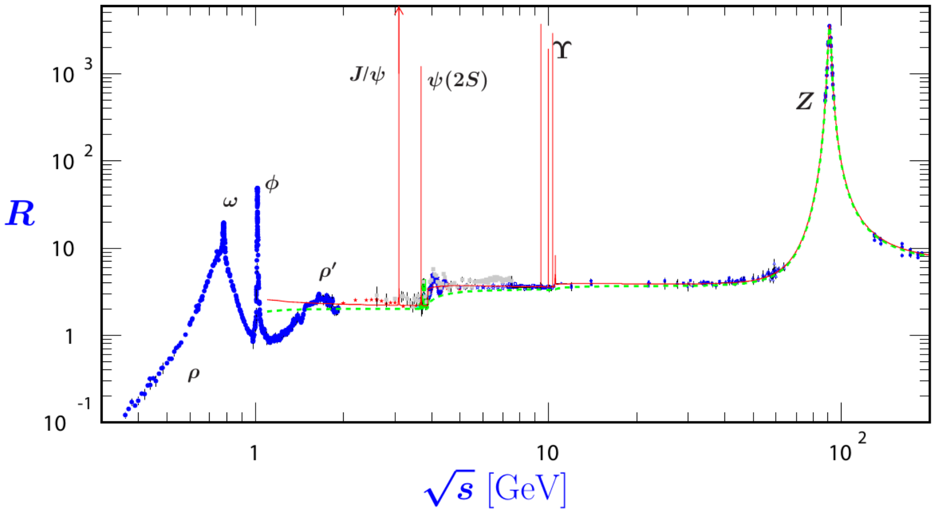

Figure 2.8: Distribution of the the hadronic ratio R in e^+e^- collisions as a function of the center-of-mass energy $\sqrt{s}$ overlayed with the prediction from a simple quark model in green [15].

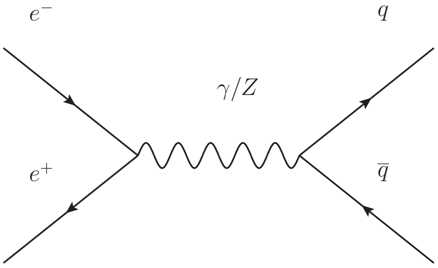

Figure 2.9: Feynman diagram showing the annihilation of electrons and positrons to quarks.

$e^+e^- \rightarrow qq$ is presented in Fig. 2.9. All observable states are colorless which implies that free quarks cannot be observed. This is also known as the confinement hypothesis.

Measurements of the proton structure-functions show that partons (the constituents of the hadron: quarks and gluons) behave as free particles at high energies but are strongly bound otherwise (asymptotic freedom).

Color is the charge associated with strong interactions. The requirements that three colors exist, asymptotic states are color-singlets, and quarks are different states than antiquarks imply that the symmetry group for the color sector is SU(3).

In the same way as for QED and the electroweak sector, the full Lagrangian of strong interactions can be derived starting from the free Lagrangian:

$$\mathscr{L}_0 = \sum_f i\overline{q_f}\gamma^\mu \partial_\mu q_f - m_f \overline{q_f} q_f$$

where f are the different flavors and q_f^α is a three-vector in color-space.

This Lagrangian is invariant under global transformations of the form:

$$q_f^\alpha \to q_f'^\alpha \equiv U^\alpha_\beta q_f^\beta$$

with the transformation matrix

$$U = e^{-g_s \frac{\lambda^a}{2}\theta_a}.$$

The θ_a are arbitrary transformation parameters and λ^a the eight Gell-Mann matrices:

$$\lambda^1 = \begin{pmatrix} 0 & 1 & 0 \\ 1 & 0 & 0 \\ 0 & 0 & 0 \end{pmatrix} \; \lambda^2 = \begin{pmatrix} 0 & -i & 0 \\ i & 0 & 0 \\ 0 & 0 & 0 \end{pmatrix} \; \lambda^3 = \begin{pmatrix} 1 & 0 & 0 \\ 0 & -1 & 0 \\ 0 & 0 & 0 \end{pmatrix}$$

$$\lambda^4 = \begin{pmatrix} 0 & 0 & 1 \\ 0 & 0 & 0 \\ 1 & 0 & 0 \end{pmatrix} \; \lambda^5 = \begin{pmatrix} 0 & 0 & -i \\ 0 & 0 & 0 \\ i & 0 & 0 \end{pmatrix}$$

$$\lambda^6 = \begin{pmatrix} 0 & 0 & 0 \\ 0 & 0 & 1 \\ 0 & 1 & 0 \end{pmatrix} \; \lambda^7 = \begin{pmatrix} 0 & 0 & 0 \\ 0 & 0 & -i \\ 0 & i & 0 \end{pmatrix} \; \lambda^8 = \frac{1}{\sqrt{3}} \begin{pmatrix} 1 & 0 & 0 \\ 0 & 1 & 0 \\ 0 & 0 & -2 \end{pmatrix}.$$

Again, to achieve invariance under local transformations $\theta \to \theta(x)$, additional gauge fields have to be added to the covariant derivative:

$$D^\mu q_f \equiv (\partial^\mu - i g_s \frac{\lambda_a}{2} G^\mu_a) q_f.$$

The G^μ_a represents the field for the eight gauge bosons — gluons — of QCD. Using the short-hand notation

$$G^\mu = \frac{\lambda^a}{2} G^\mu_a$$

the field-strength tensor for the gluon field can be written as:

$$G^{\mu\nu} = \partial^\mu G^\nu - \partial^\nu G^\mu - i g_s [G^\mu, G^\nu].$$

The full Lagrangian of QCD reads then:

$$\mathscr{L}_{\mathrm{QCD}} \equiv -\frac{1}{4}\,\mathrm{Tr}[G^{\mu\nu}G_{\mu\nu}] + \sum_f \left(i\overline{q_f}\gamma^\mu \partial_\mu q_f + g_s \overline{q_f}\gamma^\mu G_\mu q_f - m_f \overline{q_f} q_f \right).$$

The non-commutative nature of SU(3) gives rise to gauge self interactions. The coupling constant g_S (strong coupling constant) is universal.

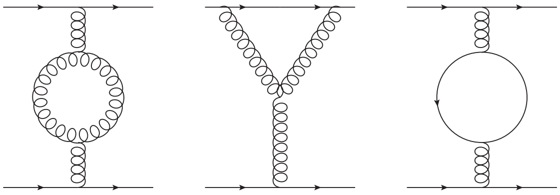

Figure 2.10: Feynman diagrams showing contributions to the running coupling of α_S.

To understand the observed asymptotic freedom of QCD it is necessary to investigate higher-order quantum corrections. These higher-order loop diagrams can lead to contributions approaching infinity for high energies. Examples for such Feynman diagrams are shown in Fig. 2.10. A quantum theory is called renormalizable if these high-energy divergences can be a removed by a redefinition of the fields and couplings. This leads to the renormalization equation of α_S:

$$\frac{d}{d\ln\mu^2}\alpha_s(\mu) = \beta(\alpha_s) = -\sum_i \beta_i \left(\frac{\alpha_s}{4\pi}\right)^{i+1}$$

where μ is the scale and β_i are the expansion coefficients for the β-function, starting with

$$\beta_0 = \frac{11}{3}N_C - \frac{2}{3}n_F$$

The positive factor $\frac{11}{3}N_C$ is mostly due to the contributions from gluon radiation which are illustrated by the left and center diagrams in Fig. 2.10. It is proportional to the number of colors N_C. Loop corrections from gluon self-interaction lead to a vanishing coupling constant at high energies (anti-screening). The asymptotic freedom is weakened ($-\frac{2}{3}n_F$) linearly with the number of flavors n_F due to fermion loops (Fig. 2.10, right). Measurements of α_S are presented in Fig. 2.11. The value of α_S at the scale of the mass of the Z boson is $\alpha_S(M_Z) = 0.1184 \pm 0.0007$ [15].

2.2 Proton-Proton Collisions

To go from the understanding of the QCD Lagrangian to meaningful predictions for the final state of *pp*-collision events some additional ingredients are necessary. One important feature of QCD is factorization: the dynamics of the hard (high energy, short distance) interaction and the later, softer (low energy, long distance) processes can be considered separately. This allows calculating the hard process using perturbative techniques (since α_S will be small) and using a separate prediction for the transformation of the partons into colorless hadrons (*fragmentation*).

The cross section $\sigma_{pp\to X}$ for an arbitrary final state X to be produced in *pp* collisions

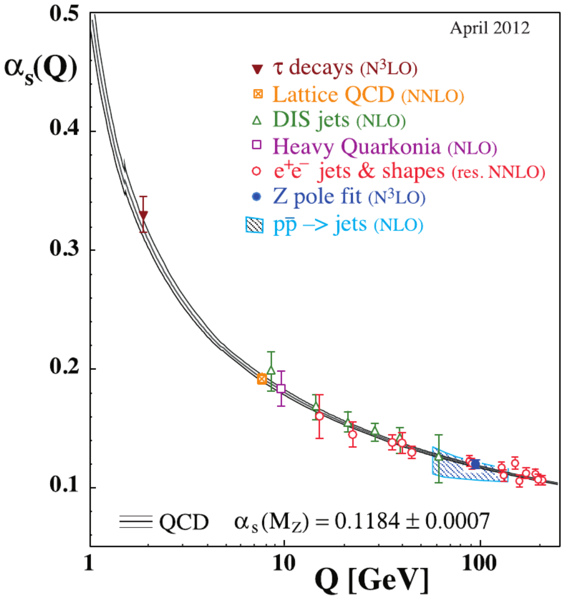

Figure 2.11: Overview of measurements of α_S at different energy scales Q [15].

with a momentum transfer Q^2 can then be written as:

$$\sigma_{pp\to X} = \sum_{ijk} \int dx_1 dx_2 dz\, f_i(x_1,\mu)\, f_j(x_2,\mu)\, \hat{\sigma}_{ij\to k}\left(x_1, x_2, z, Q^2, \alpha_S(\mu), \mu\right) D_{k\to X}(z,\mu).$$

Here the indices i, j, k go over the gluon, quark- and anti-quark-flavors in the proton, the parton distribution functions (PDF) f_i is a function of x — the fraction of the proton momentum carried by the quark or gluon. The cross-section of the hard process $\hat{\sigma}_{ij\to k}$ can be calculated perturbatively and $D_{k\to X}$ are the fragmentation functions relating the parton from the hard process k with the final state X.

Since the proton is a complex bound state, the calculation of PDFs from first principles is not feasible. However PDFs at different energy scales are related by differential equations. These *evolution functions* can be used to transfer observed PDFs to the scale of new collider measurements. Current PDFs are obtained from deep inelastic scattering experiments (HERA), fixed-target experiments as well as measurements of $p\bar{p}$ collisions at the Tevatron. PDF sets are provided by e.g. the MWST [36], CTEQ [37], NNPDF [38] and HERAPDF [39] groups. Parton distributions from the MWST PDF set for two different values of Q are presented in Fig. 2.12. The high fraction of u and d valence quarks at high values of x and the dominance of gluons at very low x can be read off in these diagrams.

The fragmentation functions obey similar evolution equations as the PDFs and are mainly determined in e^+e^- collisions.

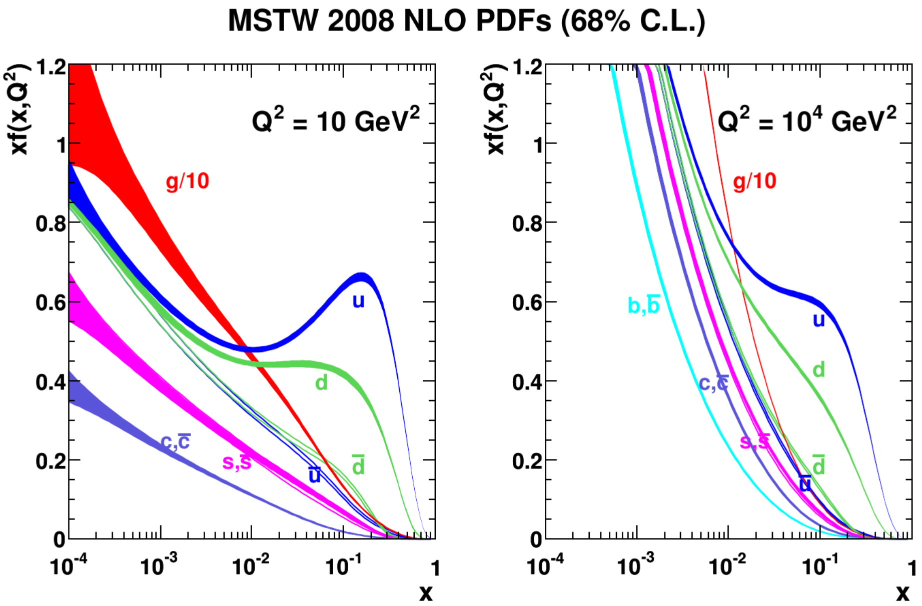

Figure 2.12: Proton parton distribution $x \cdot f(x)$ for the MSTW PDF set at (a) $Q = 10$ GeV and (b) $Q = 10^4$ GeV for different partons together with uncertainties at 68% confidence level [36].

2.3 Beyond the Standard Model

In the following, an overview of some shortcomings of the SM will be given and new theories that can correct them will be discussed. The most prominent of these issues is the so called hierarchy problem. Corrections to the Higgs boson mass due to fermion loops can be written as:

$$\Delta m_H^2 = -\frac{|\lambda_f^2|}{8\pi^2}\Lambda_{\mathrm{UV}}^2$$

where λ_f is the Yukawa coupling of the fermion and Λ_{UV} the high-energy cut-off of the theory — i.e. the highest energy at which the SM is valid. The Feynman diagram for the leading loop correction is shown in Fig. 2.13. If Λ_{UV} is taken to be the Planck scale $\approx 10^{19}$ GeV then the corrections become much larger than the physical mass of the Higgs boson of $\approx 10^2$ GeV.

There are different explanations for observing a Higgs boson mass much smaller than the corrections imply. Contributions by fermions and bosons enter with opposite sign. Therefore the couplings of the SM particles could be fine-tuned such that the corrections cancel.

A more statisfactory explanation can be provided by supersymmetry (SUSY) [40]. The correction to the Higgs mass due to scalars can be written as:

$$\Delta m_H^2 = +\frac{\lambda_s}{16\pi^2}\Lambda_{\mathrm{UV}}^2.$$

If supersymmetric partners (superpartners) with $\Delta J = \frac{1}{2}$ and $\lambda_s = \lambda_f^2$ are added for all SM particles — scalar (bosonic) partners for the fermions and fermionic partners for the

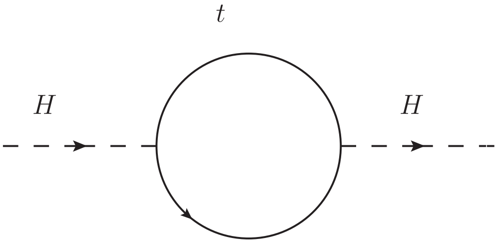

Figure 2.13: Feynman diagram for the leading top quark correction to the Higgs boson mass.

SM bosons — their contributions will exactly cancel. All quantum numbers except the spin are equal for SM particles and their superpartners. If supersymmetry was an exact symmetry, the masses of particles and their superpartners would also be equal. However, as no superpartners have been observed so far, the symmetry has to be broken creating higher masses for the superpartners. SUSY is a widely studied model of new physics and intensely looked for by collider experiments. However, so far no sign of SUSY has been found.

In Technicolor models [41] the Higgs boson is not an elementary but a composite particle. There exist new dynamics at high energies that condensate at lower energies, a process which breaks the EW symmetry. A specific model — topcolor-assisted-technicolor — will be described in more detail in Sec. 2.3.1 as it predicts resonances in the $m_{t\bar{t}}$ spectrum.

Finally, the natural cut-off of the SM at the Planck-scale can be lowered by introducing additional space-time dimensions. Models of extra-dimensions have in common that SM particles mainly propagate in the so-far observed dimensions whereas gravitation also acts in the additional dimensions. Two important theories are Arkani-Dimopoulos-Dvali (ADD) [42] and Randall-Sundrum (RS) [43] models of extra dimensions. The main difference is that ADD models predict at least two additional dimensions at the millimeter scale whereas RS models postulate one strongly-warped extra dimension. RS models also predict the existence of $m_{t\bar{t}}$ resonances and will be discussed in Sec. 2.3.2.

2.3.1 Z' Boson

The mass of the top quark at the EW scale makes it a natural candidate for playing a role in EWSB. This is achieved in so-called *topcolor* models [44–46]. In these models EWSB is mediated by a $t\bar{t}$ condensate state. The symmetry group of the full model is:

$$\mathrm{SU}(3)_1 \times \mathrm{SU}(3)_2 \times \mathrm{U}(1)_1 \times \mathrm{U}(1)_2 \times \mathrm{SU}(2)_L \to \mathrm{SU}(3)_C \times \mathrm{U}(1)_Y.$$

The breaking of $\mathrm{SU}(3)_1 \times \mathrm{SU}(3)_2 \to \mathrm{SU}(3)_C$, where $\mathrm{SU}(3)_1$ couples to first- and second-generation particles and $\mathrm{SU}(3)_2$ to the third generation, gives rise to a new octet of massive bosons. These are the so-called top-gluons and couple mainly to $t\bar{t}$ and $b\bar{b}$ states.

This scheme has two problems [47]: the top- and b-quark masses are degenerate and the model predicts a top-quark mass of ≈ 600 GeV which is too large. Different strategies exist that can be used to derive a physical top-quark mass: topcolor can be combined with a SUSY theory or technicolor models (technicolor assisted topcolor). It is also possible to utilize a seesaw mechanism [48, 49]: the 600 GeV state couples to another EW singlet which reduces the physical mass to the observed value.

All these models however require one additional ingredient: an enhancement of $\langle t\bar{t}\rangle$ states with simultaenous suppression of $\langle b\bar{b}\rangle$ states is necessary. To this end a new force is introduced that acts attractively on $t\bar{t}$ but repulsively on $b\bar{b}$. This can achieved by introducing another U(1) symmetry into the model. Analogous to the extended symmetry giving rise to $\mathrm{SU}(3)_C$ described above, the weak hypercharge operator $\mathrm{U}(1)_Y$ is created by the symmetry breaking: $\mathrm{U}(1)_1 \times \mathrm{U}(1)_2 \rightarrow \mathrm{U}(1)_Y$. This leads to a new heavy gauge boson: the Z'. That such an approach can statisfy current experimental constraints on flavor changing processes is shown in Ref. [50].

Four different models exist, distinguished by which families of quarks and leptons couple to the gauge groups $\mathrm{U}(1)_1$ and $\mathrm{U}(1)_2$ respectively. In the standard Z' model (Model I) $\mathrm{U}(1)_1$ couples to the first and second generation and $\mathrm{U}(1)_2$ to the third, leading to a relatively low production cross-section for the Z' in proton-proton collisions. The cross-section can be increased by also allowing a coupling of $\mathrm{U}(1)_2$ to the first generation (Model II) or the first and second generation (Model III).

Most interesting for resonance searches in the $t\bar{t}$ invariant mass spectrum is Model IV: only the quarks from generation one and three couple to $\mathrm{U}(1)_2$. This circumvents more stringent limits obtained in searches utilizing the ee and $\mu\mu$ final states while providing a large-enough cross-section for detection at the LHC. The Lagrangian for this model is given by:

$$\begin{array}{rcl}\mathscr{L}_{Z'} & = & (\frac{1}{2}g_1 \cot\theta_H) Z_t'^{\mu} (\bar{t}_L\gamma_\mu t_L + \bar{b}_L\gamma_\mu b_L + f_1\bar{t}_R\gamma_\mu t_R + f_2\bar{b}_R\gamma_\mu b_R \\ & & -\bar{u}_L\gamma_\mu u_L - \bar{d}_L\gamma_\mu d_L - f_1\bar{u}_R\gamma_\mu u_R - f_2\bar{d}_R\gamma_\mu d_R)\end{array} .$$

To ensure the desired attraction and repulstion for $t\bar{t}$ and $b\bar{b}$ respectively, the coefficients need to be set to: $f_1 > 0$, $f_2 < 0$ and $\cot\theta_H \gg 1$. Here θ_H denotes the mixing-angle. The width varies as a function of the parameters, but it can be as low as $\Gamma = 0.012m$ which justifies treating the Z' as a narrow resonance. The Feynman diagram for Z' production and decay at the LHC is shown in Fig. 2.14.

2.3.2 Kaluza-Klein Gluon

Current observations strongly imply that our universe has a four-dimensional space-time. However, a small compact or strongly curved extra dimension of space is not excluded. If a SM particle propagates in such a small extra dimension then *Kaluza Klein* (KK) partner states will be visible to a four-dimensional observer [51, 52]. These states have the same quantum numbers but a higher invariant mass $M_{obs.}$, increased by the momentum-component in the extra dimension p_{5d}:

$$M_{obs.}^2 = m^2 + p_{5d}^2.$$

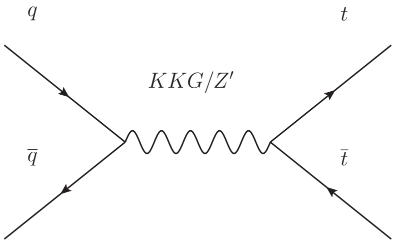

Figure 2.14: Feynman diagram showing the leading contribution to the production of Z' bosons and KK gluons at the LHC. Also shown is the subsequent decay to pairs of top-quarks.

A small and compact extra dimension with periodic boundary conditions leads to quantization of the momentum

$$p_{5d} = n \cdot \frac{h}{\lambda}$$

where n is an integer number, h the Planck-constant and λ the circumference of the extra dimension. A so-called KK tower of new resonances with masses determined by the size of the extra dimension is created.

The main purpose for considering theories of extra dimensions is that these could provide a solution to the hierarchy problem. How this works will be explained for the RS model of extra dimensions [43, 53]. It postulates that our 3+1 dimensional space (three-brane) occupies only a subspace of the full five-dimensional geometry and that the extra dimension of space is strongly curved.

A solution of the Einstein-equation is given by the non-factorizable metric:

$$ds^2 = e^{-2k|y|}\eta_{\mu\nu}dx^\mu dx^\nu - dy^2$$

where the x^μ are the four-dimensional coordinates, y the coordinate of the fifth direction and k is a measure for the curvature of this extra dimension. The geometry of the extra dimension is the orbifold $S_1/\mathbb{Z}_2$ — corresponding to a line with a three-brane on each end. One is labelled the low energy (IR) brane, the other is the high energy (UV) brane. This is illustrated in Fig. 2.15.

The exponential hierarchy between the weak and the Planck scale is then introduced by the background-metric. Masses (m_0) on the three-brane and the underlying theory at the Planck scale (m) are related by:

$$m = e^{-kr_c\pi}m_0.$$

with r_c as the size of the extra dimension. Physical masses in the TeV-range can come from a warp-factor $e^{-kr_c\pi} \approx 10^{15}$ which due to its exponential nature implies a small hierarchy between the underlying parameters.

The initial RS models postulated that the SM fields are strictly localized in the IR brane and that only gravitation would act in the fifth dimension. Assuming that the

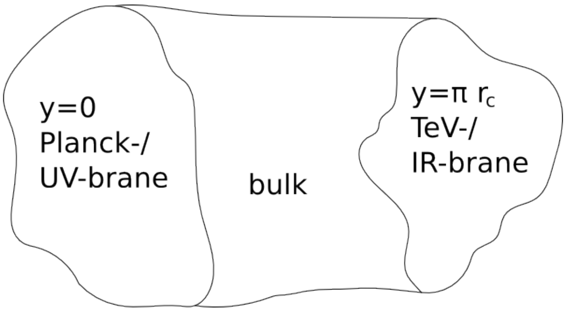

Figure 2.15: Illustration of the Planck- and TeV-brane in the RS model. The coordinate in the extra dimension is denoted by y and its size by r_c.

SM fields also propagate in the fifth dimension increases the agreement with precision measurements of EW parameters and the resulting model does not suffer from unobserved flavor-changing neutral currents [24–26].

According to the mechanism described above, SM particles with degrees-of-freedom in the fifth dimension will have KK partners with higher masses. Due to its strong coupling and high production cross-section at the LHC, the most interesting particle will be the first KK excitation of the gluon: the KK gluon (KKG). The wave function of most SM fermions is localized towards the UV brane, with the exception of the top quark which is closer to the IR brane. As the KK gluon wave function also peaks towards the IR brane, the main decay mode of the KK gluon $g^{(1)}$ is $g^{(1)} \to t\bar{t}$. In Fig. 2.16 the decay channels for KK gluon of different mass are shown and the reaction is illustrated in Fig. 2.14.

The effective four-dimensional couplings to the KK gluon are calculated by integrating over the fifth dimension. This leads to the left-handed (g_L) and right-handed (g_R) couplings to quarks: $g_L = g_R = -0.2g_S$ for light quarks including charm, where $g_S = \sqrt{4\pi\alpha_s}$; $g_L = g_S$; $g_R = -0.2g_S$ for bottom quarks; and $g_L = g_S$; $g_R = 4g_S$ for the top quark. The resulting decay width is $\Gamma/m = 15.3\%$ — KK gluons are broad resonances.

2.4 Jet Clustering

In the previous section it was shown how new theories beyond the SM can lead to resonances decaying into top-quark pairs which have a high probability to further decay into hadrons. Hadronic final states are then analysed using so-called jets [54].

Due to fragmentation, the decays of final-state particles from the hard interaction result in showers of collimated hadrons (jets) which are measured using calorimeters. The individual reconstruction of particles in the shower is not feasible. Therefore jet clustering algorithms are used to capture all decay products of the particle that initiated the shower to access the hard interaction.

Jet algorithms can either operate on detector objects (e.g. calorimeter cells) or partons (in QCD calculations). These objects need to be organized (clustered) to jets that correspond closely to the four-momenta of the initial hard partons.

There are two different types of clustering algorithms: cone-based and sequential

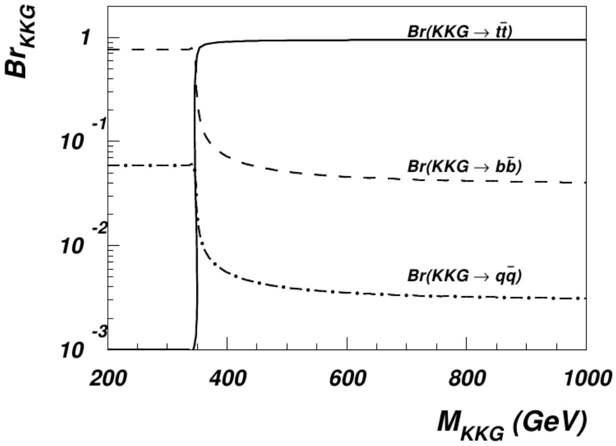

Figure 2.16: Expected branching ratios of a KK gluon as a function of the mass [24].

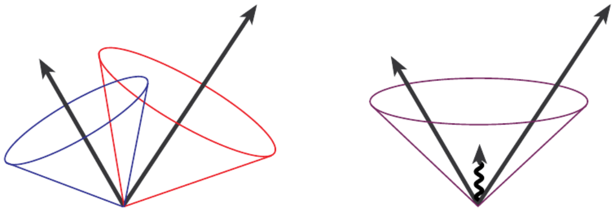

Figure 2.17: Illustrated example of IR sensitivity of cone algorithm jets. The seeds are represented by arrows and the length of an arrow is proportional to its energy. Additional soft radiation between the jets (right figure) can lead to the merging of otherwise separate jets (left figure)[54].

recombination algorithms. In cone-based algorithms the jets are defined as cones around the directions of large energy deposits. Recombination-type algorithms instead use a distance measure between the initial objects and step-wise merge the closest two until the minimal distance exceeds a cut-off value. After evaluating some desirable characteristics for jet algorithms, concrete examples of the different types of algorithms will be discussed.

2.4.1 Jet Properties

An important criterion for jet algorithms is *infrared (IR) safety*. Jets reconstructed using IR safe algorithms are robust against the emission of soft particles. The probability for such emissions diverges for low energies and predictions (for example of cross-sections) obtained using IR-sensitive algorithms can also diverge. Algorithms requiring an initial seed (typically cone-based algorithms) are especially sensitive to IR effects. Jets also should be *collinear safe*, meaning that the close-angle splitting of a parton (for example a gluon) should not affect the final jets. In Fig. 2.17 (Fig. 2.18) an example for IR safety (collinear safety) is presented. The shape of the boundary of a jet should also be robust

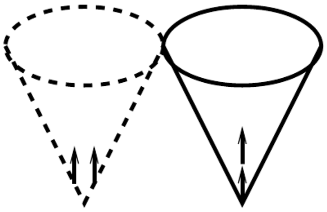

Figure 2.18: Illustrated example of collinear sensitivity of cone algorithm jets. The seeds are represented by arrows and the length of an arrow is proportional to its energy. If the energy (left) is split between calorimeter clusters it can be too low to pass the threshold for creating a seed while the narrow energy distribution (right) passes the threshold [54].

against small changes in the final state.

In proton-proton (or proton-antiproton) collisions the longitudinal boost of the hard interactions is in general not known and jet algorithms that are invariant under the boost are preferred. Robustness against higher-order QCD and hadronization corrections are also desirable.

2.4.2 Cone Algorithms

A simple cone-based jet algorithm (Snowmass [54, 55]) starts by placing cones (circles with a fixed radius R in the η-ϕ-plane[1]) around seeds (energy deposits with energies above a certain threshold). Then the energy-weighted centroid of all objects within the cone is calculated and used as the center of a new trial-cone. This procedure is iterated, using the cone-axis as new seed, until the cone is stable: the centroid and the axis align. For the final direction of the jet, the E_T-weighted ϕ- and η-directions of the particles are used.

This procedure can lead to overlapping cones, where particles are shared between different jets. In this case the particles are either assigned to the closer (in η-ϕ-space) jet or the two jets are merged, depending on how large the fraction of shared p_T is with respect to the p_T of the highest-p_T jet.

A modern jet finder is the Seedless Infrared-Safe Cone jet algorithm (SISCone [56]). It starts by finding all distinct (containing different particles) possible cones for a given cone-size, where cones are defined by the radius and two particles on the boundary. This is illustrated in Fig. 2.19. In a next step the cones are checked for stability: A cone is called stable if the centroid lies inside the cone. Finally a split-merge procedure is employed to arrive at final-jets.

The main advantage of SISCone over other cone-based jet algorithms is that, due to not-using explicit seeds, the algorithms is IR-safe. However the boundary of SISCone jets is still susceptible to soft radiation [57].

---

[1] The coordinate system is defined in Sec. 4.1.

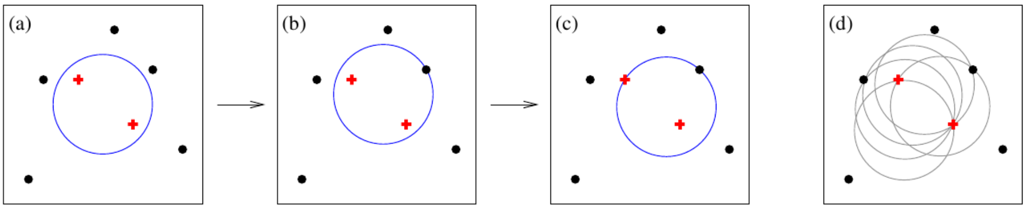

Figure 2.19: All circular enclosures can be moved so that two particles lie on the boundary without changing the particle content: (a) Starting from an arbitrary enclosure; (b) moving in a random direction until a point (either internally or externally) touches the boundary; (c) rotating around one of the points until another point touches the boundary; (d) given two edge points all possible circles result in the same particle content [56].

2.4.3 Sequential Recombination Algorithms

The three most commonly used recombination type jet algorithms are the k_t [58, 59], Cambridge/Aachen [60], and anti-k_t [57] algorithms. All three algorithms evaluate the pair-wise distances d_{ij} between all input objects (partons or calorimeter cells). In this context partons are defined as the final state particles of the hard interaction before hadronization. If the smallest d_{ij} is smaller then the smallest beam-distance d_{iB}, the two objects (i and j) are combined to form a proto-jet, otherwise the object i is removed from the process and taken as a jet. The distance measures are defined as:

$$d_{ij} = \min(k_{ti}^{2p}, k_{tj}^{2p}) \frac{\Delta_{ij}^2}{R^2},$$

and

$$d_{iB} = k_{ti}^{2p},$$

where k_{ti} denotes the transverse momentum, R is the distance-parameter and

$$\Delta_{ij}^2 = (y_i - y_j)^2 + (\phi_i - \phi_j)^2$$

with y being the rapidity and ϕ the azimuthal angle. The parameter p is set to 1 for the k_t, to 0 for the Cambridge/Aachen and to -1 for the anti-k_t algorithm. Two objects are combined by adding their four-momenta. Due to the pair-wise combination steps an initial object can only be assigned to exactly one jet and no split-merge step is necessary. All three algorithms are IR-safe. The Cambridge/Aachen prescription leads to a strictly geometrical ordering. In the case of k_t softer objects — given equal angular distances — are joined first whereas for anti-k_t the hardest clusterings are performed first. One additional advantage of the anti-k_t algorithm, compared to other recombination algorithms, is that it leads to more circular jets in the η-ϕ-plane — it is resilient against soft radiation on the boundary. The active area of different jet clustering algorithms is shown in Fig. 2.20. The most circular jets are given by the anti-k_t and SISCone algorithms whereas the boundaries of k_t and Cambridge/Aachen jets are sensitive to soft radiation. On the other hand the ordering of k_t and Cambridge/Aachen jets allows an easier interpretation of the substructure of jets in terms of QCD [61].

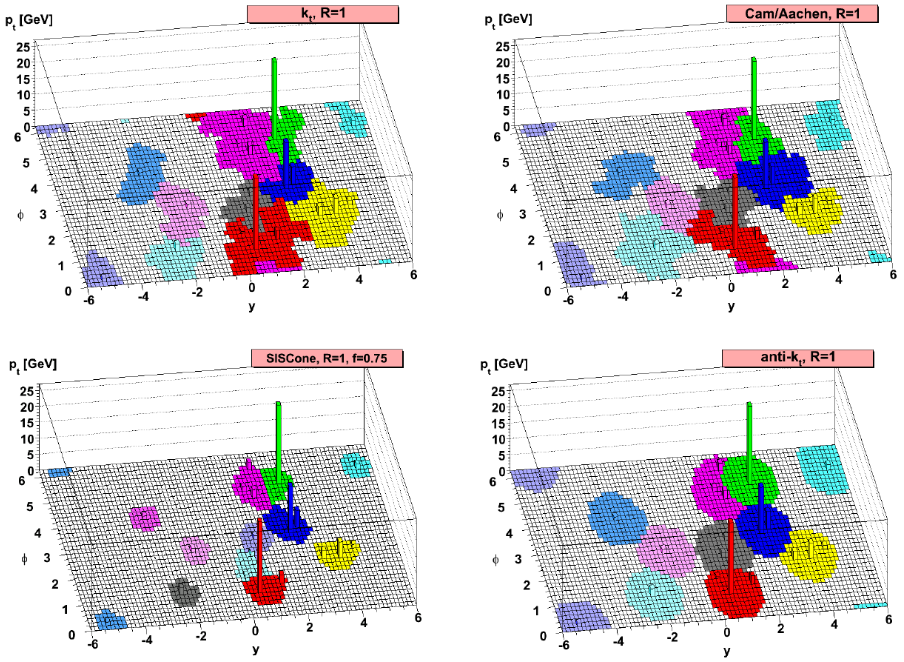

Figure 2.20: Active area of four different jet clustering algorithms. A parton level event is overlayed with soft *ghost* particles to illustrate the effective area of the hard jets [57].

2.5 HEPTopTagger

In Sec. 2.3 new resonances which decay predominantly to top-quark pairs were discussed. Top quarks almost exclusively decay into a b-quark and a W boson. The W boson then either decays to hadrons with 68 % probability or to a neutrino plus charged-lepton in the other cases. In the leptonic decay of the W all three lepton flavors are approximately equally likely. Feynman diagrams for the two different decay chains of the top quark are presented in Fig. 2.21.

For $t\bar{t}$ decays this means that 10 % of events have two charged leptons in the final state (di-leptonic channel), 44 % have one charged lepton (lepton+jets channel) and 46 % have only jets (fully hadronic). Searches for $t\bar{t}$ resonances traditionally focus on the lepton+jets and the di-leptonic channel because charged leptons can efficiently be used to reject non-top-quark backgrounds. To access the large fraction of events in the fully hadronic final state, methods to identify hadronically decaying top quarks are necessary.

For low top-quark p_T the three quarks from the hadronic decay will lead to three distinct jets that can be reconstructed in the detector. As the top-quark momentum increases these jets move closer in the η-ϕ-plane and, with sufficiently high p_T (*boosted*), merge into one jet. The HEPTopTagger [20, 21] algorithm is designed to identify such boosted top-quark decays using the sub-structure of jets reconstructed with a large distance parameter R (fat jets). The relation between the size of fat jets and the top-quark p_T is shown in Fig. 2.22.

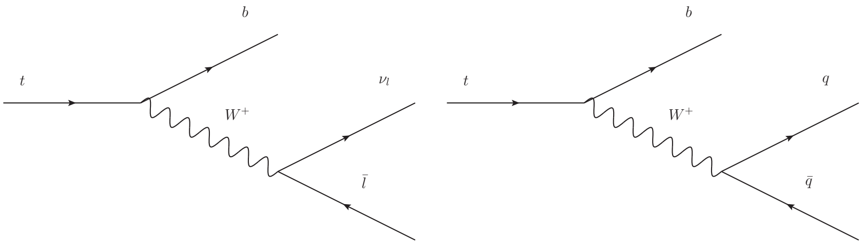

(a) (b)

Figure 2.21: Feynman diagram for the top-quark decays with (a) a charged lepton in the final state and (b) hadrons in the final state. Here l stands for e, μ or τ.

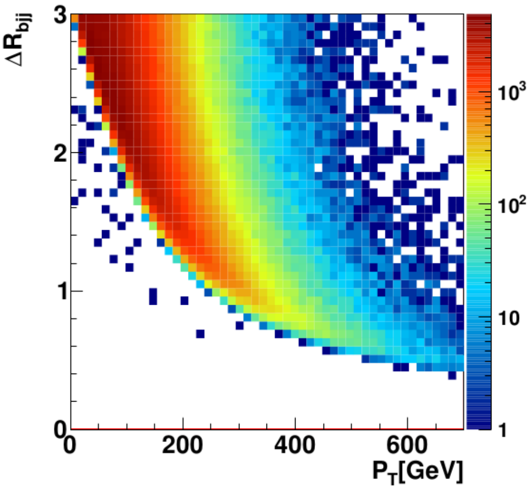

(a)

Figure 2.22: Minimal jet radius necessary to contain the three quarks from an hadronic top-quark decay as a function of the top-quark p_T. The color indicates the number of top quarks from SM $t\bar{t}$ MC simulation [21].

As described in Sec. 3, high data rates for the LHC experiments come at the cost of pile-up: a combination of the effects of multiple proton-proton interactions per bunch-crossing and the relative length of the integration time of the calorimeters compared to the bunch spacing. Pile-up typically leads to overestimating the energy in the calorimeters. The underlying event — the interactions of the remains of the protons that undergo the hard interaction [62] — further contributes to this mis-measurement. Analysis of the substructure can be used to identify and subtract contributions from pile-up and underlying event leading to a more precise and stable measurement of the masses and momenta of top-quarks. In the HEPTopTagger this is achieved in a so-called filtering step.

In the following, the steps of the HEPTopTagger algorithm, as introduced in Ref. [21], are described. The algorithm is illustrated in Fig. 2.23. First the input objects (either clusters of calorimeter cells or partons) are clustered into a fat jet with $R = 1.5$ (Fig. 2.23a). Throughout the HEPTopTagger procedure the C/A jet algorithm, described in Sec 2.4, is used. Fat jets with $p_{\mathrm{T}} > 200$ GeV are analyzed further. This selection is motivated by Fig. 2.22: at $R = 1.5$ only the reconstruction of top quarks with $p_{\mathrm{T}} > 200$ GeV is possible.

To arrive at the hard substructure, the last C/A clustering steps are undone: the jet j is split into subjets j_1 and j_2 ($m_{j_1} > m_{j_2}$). If $m_{j_1} < 0.8 m_j$ then both jets are kept, otherwise j_2 is discarded. In Fig. 2.23b the two subjets resulting from the first unclustering step are shown. This splitting is repeated until the masses of all subjets are below 50 GeV. All triplets of such subjets are further analyzed. If less than three subjets are found, the fat jet is discarded. The sketch in Fig. 2.23c illustrates a situation where 4 subjets with masses below 50 GeV are found. All triplets are further analyzed by the HEPTopTagger algorithm. For illustration only the analysis of the first triplet (consisting of the jets labelled A-C) is shown in more detail here.

To reduce the influence of the underlying event and pile-up, a filtering step is performed. The constituents of the subjet-triplet are re-clustered with half the minimal distance of jets within the triplet as a distance parameter (at most $R = 0.3$). The result of this re-clustering is shown in Fig. 2.23d. If this results in more than five subjets, the ones with the lowest p_{T} are discarded. Five subjets are kept to allow for additional QCD radiation during the decay (Fig. 2.23e).

One final re-clustering step is necessary to identify the subjets with the three jets from the $t \to Wb \to q\overline{q'}b$ decay. The constituents of the up-to-five subjets are clustered into exactly three jets j_1, j_2, and j_3 (ordered in p_{T}) using the exclusive C/A [60, 63] algorithm. The final three subjets are presented in Fig. 2.23f. In order to check for compatiblity with a hadronic top-quark decat the ratios of subjet masses have to fulfill one of three pairs of inequalities:

$$0.2 \arctan \frac{m_{13}}{m_{12}} < 1.3 \text{ and } R_{min} < \frac{m_{23}}{m_{123}} < R_{max}$$

$$R_{min}^2 \left(1 + \left(\frac{m_{13}}{m_{12}}\right)^2\right) < 1 - \left(\frac{m_{23}}{m_{123}}\right)^2 < R_{max}^2 \left(1 + \left(\frac{m_{13}}{m_{12}}\right)^2\right) \text{ and } \frac{m_{23}}{m_{123}} > 0.35$$

$$R_{min}^2 \left(1 + \left(\frac{m_{12}}{m_{13}}\right)^2\right) < 1 - \left(\frac{m_{23}}{m_{123}}\right)^2 < R_{max}^2 \left(1 + \left(\frac{m_{12}}{m_{13}}\right)^2\right) \text{ and } \frac{m_{23}}{m_{123}} > 0.35.$$

Here m_{ij} is the mass of the vector-sum of the subjets i and j and m_{123} the mass of the vector sum of all three subjets. The mass ratio boundaries are $R_{min} = 0.85 \frac{m_W}{m_t}$ and $R_{max} = 1.15 \frac{m_W}{m_t}$. For m_t and m_W the measured values of respectively 172.3 GeV [64] and 80.4 [15] are used. The distribution of events in the plane formed by $\arctan \frac{m_{13}}{m_{12}}$ and $\frac{m_{23}}{m_{123}}$ is presented in Fig. 2.24. Comparing the distribution for $t\bar{t}$ with the potential backgrounds motivates the selected region.

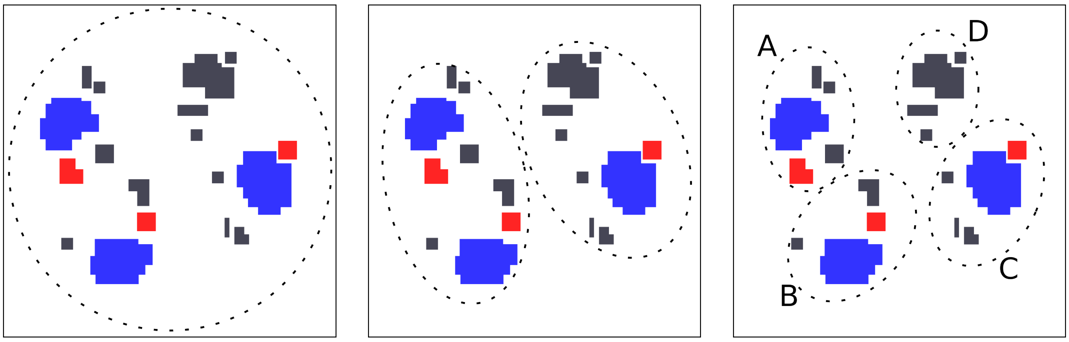

(a) initial fat jet

(b) fat jet after first unclustering step

(c) fat jet after the last unclustering step

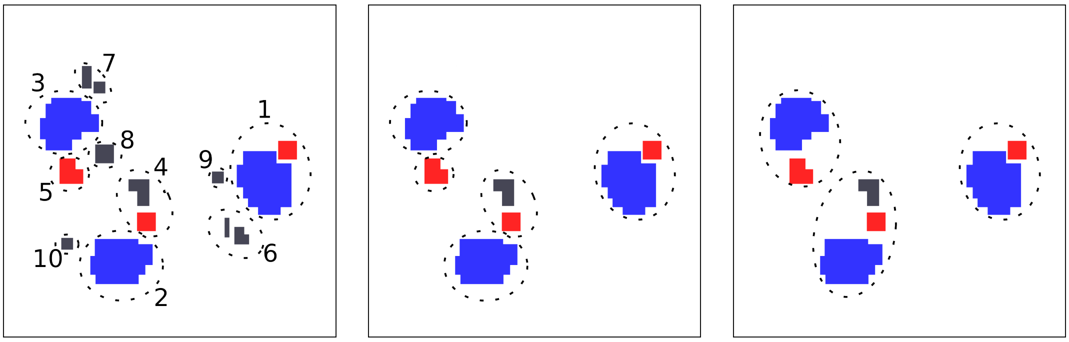

(d) re-clustered constituents of the triplet of jets A, B and C from the previous step using a smaller distance parameter

(e) the five leading subjets found in the previous step

(f) constituents of the five jets from the previous step re-clustered into exactly three jets for testing mass ratios

Figure 2.23: A pictorial representation of the HEPTopTagger algorithm. The shapes composed of rectangles represent clusters of calorimeter cells in the η-ϕ-plane. The blue shapes indicate the main contributions from decays of the three quarks produced in a hadronic decay of a top quark. The red shapes are additional gluons radiated off by the three initial quarks that were clustered into separate objects in the calorimeter. The grey shapes represent additional energy deposits in the calorimeter due to the underlying event and pile-up. The dashed ellipses represent which objects together form a jet. The steps of the algorithm are discussed in the main text. In (c) the letters A-D are used to label the four subjets found by unclustering the initial fat jet. In (d) the numbers 1-10 label the small subjets found by reclustering the consituents of the jets A-C from the previous step. The numbers indicate the p_{T} of the subjet so that jet labelled with 1 has the highest p_{T}.

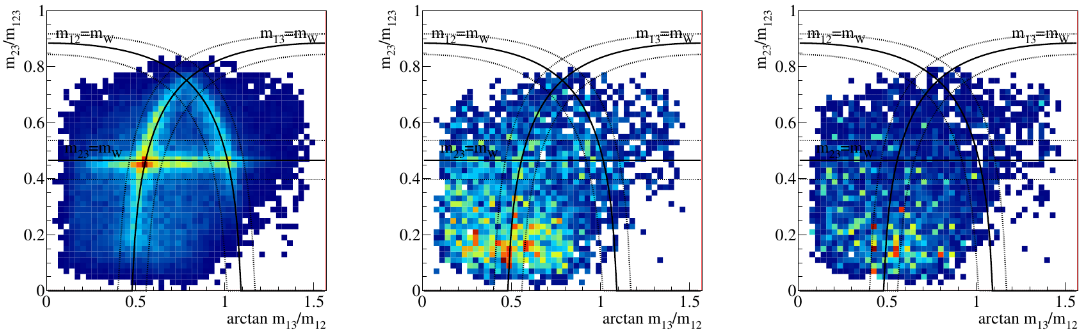

(a)

Figure 2.24: Distribution of MC simulated (left) $t\bar{t}$ (center) W+jet and (right) QCD multijet events in the arctan $\frac{m_{13}}{m_{12}}$ and $\frac{m_{23}}{m_{123}}$ plane. High (low) density areas in the phase space are indicated by red (blue) colors [21].

The choice of variables is motivated by the observation that m_t can — assuming massless final state quarks with $p_i^2 = 0$ — be rewritten as

$$m_t^2 = m_{12}^2 + m_{13}^2 + m_{23}^2,$$

which — for a fixed m_t — describes the surface of a sphere. The two coordinates arctan $\frac{m_{13}}{m_{12}}$ and $\frac{m_{23}}{m_{123}}$ then correspond to the azimuthal and polar angles of a spherical coordinate system. The inequalities involving R_{min} and R_{max} above are equivalent to $m_{ij} = m_W \pm 15\,\%$ for the three possible values of ij: m_{12}, m_{13} and m_{23}.

If a triplet fulfills these selection criteria a top-quark candidate is defined as the vector sum of the subjet four-vectors. If the top-quark candidate mass is outside the interval 140–210 GeV or the $p_{\mathrm{T}} < 200$ GeV the jet is discarded. In the case of multiple triplets meeting all requirements the one with the mass closest to m_t is selected.

When the HEPTopTagger procedure is executed using calorimeter cells (as opposed to truth-level partons) as input objects, calibration of the subjet energy to the energy of the incoming hadron jet is necessary. These calibrations are derived as a function of the p_T, η and the distance parameter of the jet using a simulation of the calorimeter response to particle jets [65, 66].

The original implementation of the HEPTopTagger algorithm uses a cut-off value of 30 GeV instead of 50 GeV[2] in the initial search for the substructure of the fat jet. The original prescription also suggests using the smaller interval of 150–200 GeV for the top-quark candidate mass. The modified parameter values were found by testing different combinations of values for all parameters of the HEPTopTagger for their effect on the expected signal and background yields [67]. The final configuration was chosen because the obtained tagging efficiency is stable for high-p_{T} top quarks and it also results in a slightly increased expected sensitivity for the fully-hadronic resonance search.

---

[2] A value of 30 GeV is used for the cut-off in the performance study presented in Sec. 6.

2.6 Statistics

The results of a search for new resonances in the $t\bar{t}$ invariant mass distribution need to be interpreted statistically. In the absence of an excess, limits on the cross-section times branching ratio ($\sigma \times BR$) can be set. In this thesis a Bayesian approach [15, 68, 69] is used.

The three axioms by Kolmogorov form the foundation of statistics:

- The probability $P(E)$ for an event E is a non-negative number: $P(E) \geq 0$;
- $\sum_i P(E_i) = 1$ when summing over all possible, mutually exclusive, events and
- $P(E_1 \cup E_2) = P(E_1) + P(E_2)$ if E_1 and E_2 are mutually exclusive events.

Conditional probabilities can be expressed in the following way: $P(A|B)$ is the probability for event A under the condition that event B occured. The joint probability can then be written as:

$$P(A \cap B) = P(A|B)P(B) = P(B|A)P(A)$$

from which Bayes' theorem follows:

$$P(A|B) = \frac{P(B|A)P(A)}{P(B)}$$

or, re-labeling the events:

$$P(s|n) = \frac{P(n|s)P(s)}{P(n)}. \tag{2.1}$$

Here $P(s|n)$ is the posterior probability for the true value s given the result of the measurement n, $P(n|s)$ is the Likelihood function for the data given a model, $P(s)$ the prior probability distribution for the theory and $P(n)$ the overall prior probability for observing a certain result.

For a counting experiment (using one bin) the likelihood function is typically chosen to be the Poisson distribution with the expectation value μ as mean:

$$P(n|\mu) = \frac{e^{-\mu}\mu^n}{n!}.$$

If the measurement is done using binned variables a multi-dimensional likelihood is used instead.

For searches for new phenomena it is usual to chose a flat prior over a finite range for the theory cross-section (s):

$$P(s) = \begin{cases} 1/s_{\text{max}} & \text{if } 0 \leq s \leq s_{\text{max}} \\ 0 & \text{otherwise} \end{cases}$$

with a large s_{max}.

Using (2.1) and $P(n) = \int_{s=0}^{\infty} P(n|s)P(s)ds$ gives:

$$P(s|n) = \frac{P(n|s)P(s)}{\int_{s=0}^{\infty} P(n|s)P(s)ds}$$

Due to experimental uncertainties a parameter can only be measured with limited precision. Following the Bayesian approach it is possible to construct an interval $[\theta_{\text{low}}, \theta_{\text{high}}]$ which has a given probability to contain the true value of a parameter θ by taking a $1-\alpha$ fraction of the posterior probability:

$$1-\alpha = \int_{\theta_{\text{low}}}^{\theta_{\text{high}}} P(\theta|n)d\theta.$$

When the parameter θ stands for the $\sigma \times BR$ of a new physics model and data and background estimates agree the lower end of the interval can be set to zero: $\theta_{\text{low}} = 0$. Inserting the posterior distribution yields:

$$1-\alpha = \frac{\int_{s=0}^{s_{\text{high}}} P(n|s)P(s)ds}{\int_{s=0}^{\infty} P(n|s)P(s)ds}.$$

Systematic uncertainties are represented by nuisance parameters (ν). In the presence of nuisance parameters all probabilities and likelihood functions not only depend on the signal strength s but also on ν: $P(n|s,\nu)$. For the final posterior the distributions are integrated over all nuisance parameters:

$$1-\alpha = \frac{\int_{s=0}^{s_{\text{high}}} \int P(n|s,\nu)P(s)P(\nu)dsd\nu}{\int_{s=0}^{\infty} \int P(n|s,\nu)P(s)P(\nu)dsd\nu},$$

where the prior distributions for the nuisance parameter $P(\nu)$ are usually assumed to be Gaussian. The above integrals in general cannot be solved analytically — instead numerical integration techniques are employed.

Chapter 3

Large Hadron Collider

The Large Hadron Collider (LHC) is a proton-proton, Pb-Pb and proton-Pb collider at CERN. It has a circumference of 26.7 km and is built in the tunnel of the former Large Electron–Positron Collider (LEP). The LHC is designed to achieve a center-of-mass energy for proton-proton beams of $\sqrt{s} = 14$ TeV. In 2010 and 2011 the LHC was operated at $\sqrt{s} = 7$ TeV and in 2012 this energy was increased to $\sqrt{s} = 8$ TeV.

There are four major experiments at the LHC: ATLAS (A Toroidal LHC Apparatus), CMS (Compact Muon Solenoid), LHCb (Large Hadron Collider beauty) and ALICE (A Large Ion Collider Experiment) which are shown in Fig. 3.1. We will shortly review the physics goals at the LHC (Sec. 3.1) followed by the parameters of the accelerator and the performance so far (Sec. 3.2).

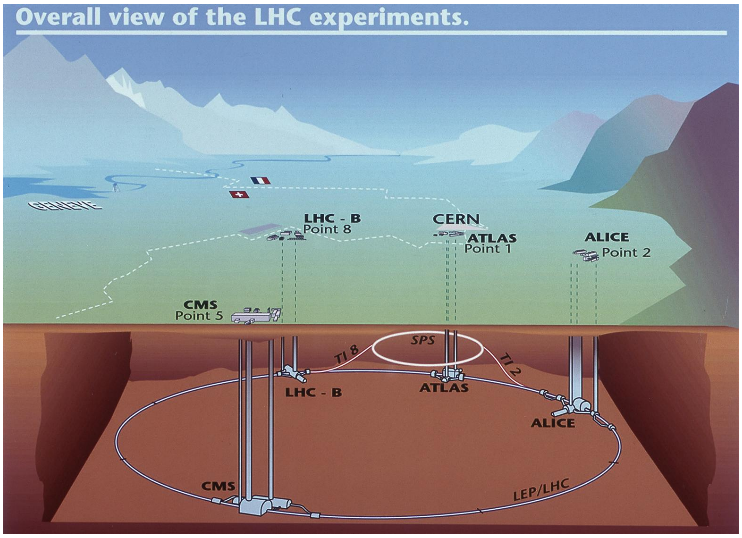

Figure 3.1: Overview of the four main experiments at the LHC [70].

3.1 Physics Goals

The two general purpose experiments at the LHC [16, 71] are ATLAS [17] and CMS [18]. They are designed to deepen our understanding of electroweak symmetry breaking, perform precision measurements of the SM and conduct searches for new physics beyond the SM.

The Higgs boson is the last missing piece of the SM, providing masses to all other particles. Previous experiments at the LEP [72–74] and Tevatron [75] facilities were able to exclude large ranges of possible masses. The LHC was designed to provide sufficient energy and number of collision events to find or exclude a SM Higgs boson in the mass range predicted by precision fits to previous measurements [13, 14, 76]. In 2012 a new resonance, so far compatible with expectations for the Higgs boson, has been found by both the ATLAS and CMS experiments [8, 9]. Measuring its properties such as mass and branching ratios and thus determining if this particle is indeed the SM Higgs boson will be an important part of the LHC physics program for the next years. ATLAS and CMS also utilize the unprecedented energy and amount of data to search for new phenomena beyond the SM.

The LHC can also be used to perform precision measurements of the SM and increase our understanding of QCD. Top quarks will be produced in large quantities, allowing a more precise measurement of their mass and couplings. Precision measurements of the electroweak gauge bosons benefit from larger amounts of data and can be used to deepen our understanding of PDFs.

LHCb [77] is a dedicated b-physics experiment aiming to measure the properties of B hadrons and to investigate CP violation. An important goal is the measurement of the $B_S \to \mu\mu$ branching fraction. The B_S meson consists of a b and an anti-strange quark (or vice versa) and the decay to $\mu\mu$ is sensitive to the effects of new particles. In 2012 LHCb observed first signs of this process [78].

The LHC can also collide lead nuclei at a center-of-mass energy per nucleon-pair of 2.76 TeV. The ALICE [79] detector is optimized for the study of such heavy-ion collisions. At these energies and densities a new state of matter is expected to form: the quark-gluon plasma [80]. ALICE was designed to probe the existence of such a phase and study its properties. This will allow insights into the confinement of QCD and deepen our understanding of chiral symmetry.

3.2 LHC Machine

Before being injected into the LHC protons undergo a series of pre-acceleration steps. An overview of the CERN accelerator complex is presented in Fig. 3.2.

Protons are obtained by stripping electrons from pure hydrogen gas. The initial acceleration is done using the Linear Accelerator 2 (Linac2) which can accelerate protons up to energies of 50 MeV. Protons are then injected into the Proton Synchrotron Booster (PSB). The PSB [82] is a circular accelerator with a radius of 25 m consisting of four rings stacked on-top of each other which accelerates protons up to 1.4 GeV. The PSB started operation in 1972 and was, like all other parts of the LHC injection chain, upgraded to meet the specifications of the new accelerator.

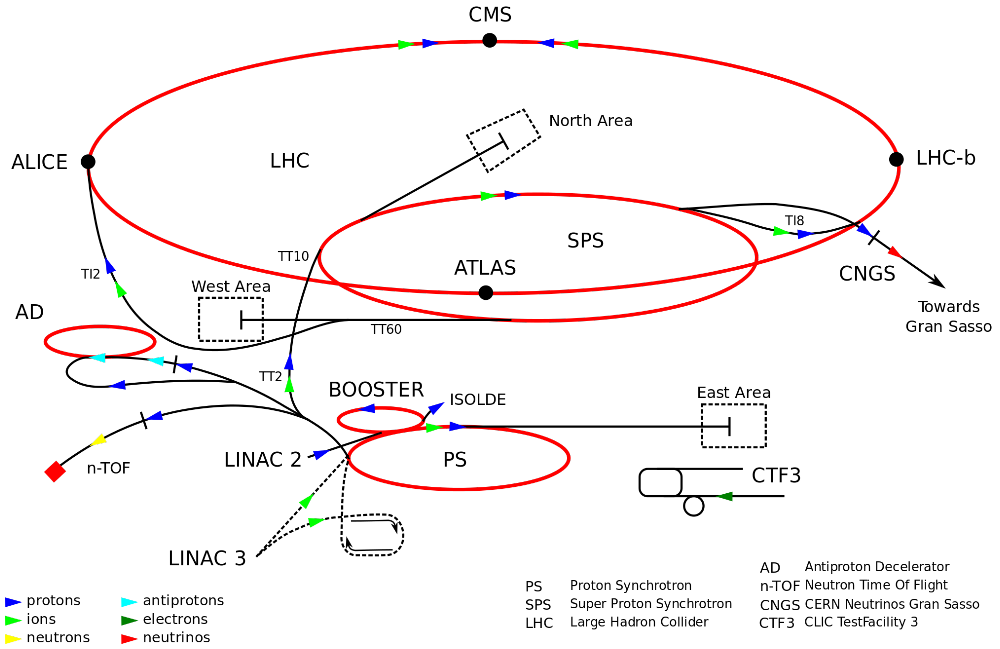

Figure 3.2: Overview of the CERN accelerator complex [81].

From the PSB [83] protons are injected into the Proton Synchrotron (PS) for acceleration to up to 25 GeV followed by the Super Proton Synchrotron (SPS) which provides protons at 450 GeV for injection to the LHC. The PS and SPS are circular accelerators with radii of 100 m and 1.08 km respectively. Both systems have been used to accelerate protons, anti-protons, electrons, positrons and heavy ions. In addition to the preparation of protons beams for injection into the LHC, beams from these accelerators are also used for fixed target experiments and to produce neutrinos for a neutrino beam to Gran Sasso (CNGS) [84].

The LHC is designed for accelerating protons up to 7 TeV. The beams are not continuous but split in up to 2808 bunches per beam, where each bunch contains up to $1.15 \cdot 10^{11}$ protons. Collisions at the four main interaction points can occur up to every 25 ns. Beams are accelerated using radio-frequency (RF) niobium-copper cavities operating at 400 MHz. Separate RF systems are used for each beam and each RF system consists of eight independent cells providing up to 2 MV for a total of 16 MV accelerating voltage. The proton energy can be increased by up to 485 keV per turn. The RF system is situated between the ALICE and CMS interaction points.

A total of 1232 superconducting Niobium-Titanium dipole magnets is used for bending the proton beams. The maximum energy of the beams is limited by the relation of momentum p, magnetic field B and bending radius ρ: $p = B\rho$. The bending radius is fixed by the geometry of the tunnel to $\rho = 2804$ m. These magnets are operated at a temperature of 1.9 K using liquid helium and are designed to provide magnetic fields up to $B = 8.33$ T. The cross section of such a 15 m long magnet is shown in Fig. 3.3.

Besides center-of-mass energy, another parameter characterizing the performance of a particle collider is the instantaneous luminosity $\mathcal{L}$ which determines the number of

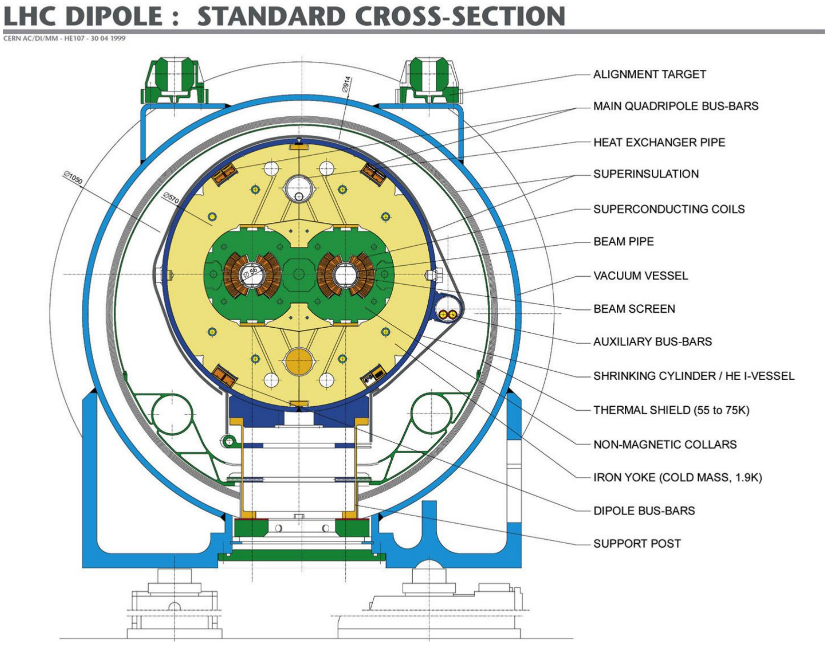

Figure 3.3: Cross section of a LHC cryo-dipole magnet [85].

interactions per second for different processes. The probability for events of a certain process to occur is measured using the cross-section σ. The total number of expected events N is then given by

$$N = \int \mathcal{L}\,\sigma dt.$$

The luminosity can be calculated as

$$\mathcal{L} = \frac{N_b^2 k_b f}{A} H_D,$$

where N_b is the number of particles per bunch, k_b the number of bunches, f the bunch crossing frequency and H_D the change in beam size due to the electromagnetic fields of the bunches which needs to be kept ≈ 1 for high-luminosity. The effective beam-overlap at the interaction points A can be calculated assuming a Gaussian beam profile with an RMS of σ_x (σ_y) in horizontal (vertical) direction and head-on colliding beams as:

$$A = 4\pi\sigma_x\sigma_y.$$

The beam sizes depend on the emittence ϵ and the β function which describes the focusing properties of the accelerator at the interaction point:

$$\sigma_{x(y)} = \sqrt{\beta_{x(y)}\epsilon_{x(y)}}.$$

The β function at the interaction (β^*) point is minimized using strong final-focus quadrupole magnets. The LHC is designed for a luminosity of $\mathcal{L} = 10^{34}\mathrm{cm}^{-2}\mathrm{s}^{-1}$.

The first proton beams were circulated in the LHC on September 10, 2008. On September 19, a magnetic quench in approximately 100 bending magnets occured due to a faulty electric connection [86]. This incident damaged 53 magnets which had to be replaced or repaired, delaying the planned LHC operational schedule.

On November 20, 2009, beams were circulated in the LHC again the first time after the incident and collisions at a center-of-mass energy of 450 GeV were achieved on November 23. The energy was then gradually increased and first collision at 3.5 TeV per bunch were recorded on March 30, 2010. Initially operating at 3.5 TeV instead of 7 TeV lead to lower electrical currents in the dipole magnets and helped avoiding further quench incidents. The 2010 proton-proton run ended on November 4 with a total integrated luminosity of 45.0 pb^{-1} recorded by the ATLAS detector.

In 2011 protons were also collided at an energy of 3.5 TeV per beam. The run lasted from March 13 to October 31 and a total integrated luminosity of $5.25\,\mathrm{fb}^{-1}$ was recorded by ATLAS. The 2012 run, with a higher energy of 4 TeV per beam, has started on April 5, 2012 and ended on December 17. In 2012 a total integrated luminosity of $21.7\,\mathrm{fb}^{-1}$ has been recorded by ATLAS. The integrated luminosity for the different proton-proton data taking periods is shown in Fig. 3.4, the number of colliding bunches in Fig. 3.5a and the peak luminosity per day in Fig. 3.5b.

High luminosities cause another, less desirable, effect: pile-up. Two types of pile-up exist: in-time and out-of-time pile-up. In-time pile-up is another name for multiple pp interactions taking place in the same bunch crossing. Out-of-time pile-up occurs when the measurement time of sub-detectors is larger than the time between bunches. This effect is typically observed for calorimeters where the integration time of O(100) ns is large compared to the design bunch spacing of 25 ns. Pile-up is characterized by the mean number of interactions per bunch crossing $\langle\mu\rangle$, measured at the beginning of a pp store:

$$\langle\mu\rangle = \frac{\mathcal{L}\,\sigma_{inel}}{n_{Bunch} f_r}$$

with the inelastic pp cross-section $\sigma_{inel} = 71.5\,\mathrm{mb}$ (73 mb for collisions at 8 TeV), the number of colliding bunches n_{Bunch} and the LHC revolution frequency f_r [87]. The distribution of $\langle\mu\rangle$ for 2011 and 2012 ATLAS data taking is shown in Fig. 3.6.

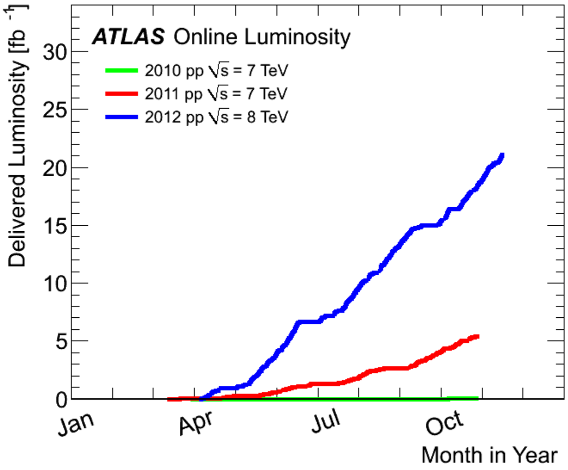

Figure 3.4: Integrated luminosity for proton-proton collisions delivered to ATLAS in 2010, 2011 and 2012 [88].

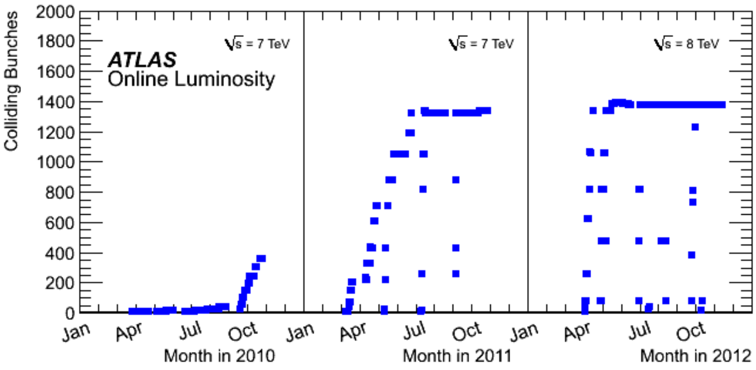

(a)

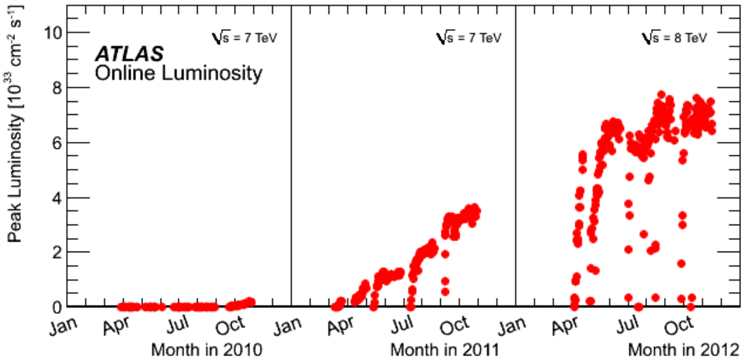

(b)

Figure 3.5: Number of (a) colliding bunches in ATLAS and (b) peak luminosity per day delivered to ATLAS during proton-proton collisions in 2010, 2011 and 2012 data taking runs [88].

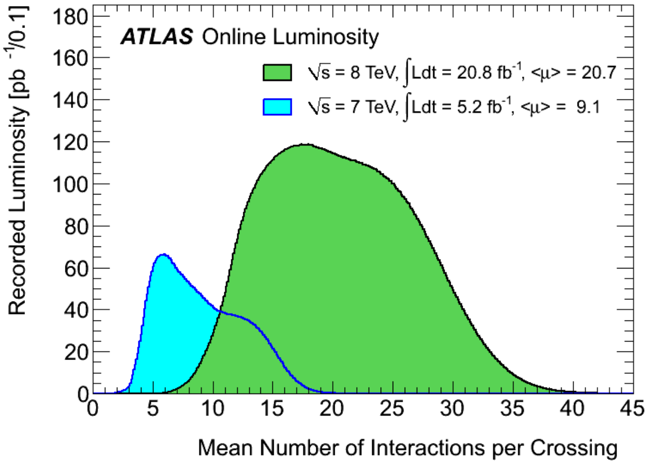

Figure 3.6: Mean number of interactions weighted to the integrated luminosity for LHC data taking in 2011 (7 TeV) and 2012 (8 TeV) as recorded by the ATLAS detector [88].

Chapter 4

The ATLAS Experiment

The ATLAS detector [17] at the LHC [16] is a multi-purpose particle physics experiment. ATLAS has a length of 45 m, a diameter of 25 m and a weight of $\approx$ 7000 t. It covers almost the full solid angle around the interaction point (IP) and is comprised of different layers.

The inner detector (ID), responsible for the reconstruction of charged tracks and vertices, consists of a silicon pixel, a silicon microstrip (SCT) and a transition-radiation tracker (TRT). Tracking capabilities extend up to $|\eta| < 2.5$[1] and are described in Sec. 4.2. The ID is contained in a 2 T solenoidal magnetic field. Outside of this superconducting magnet are a liquid-argon (LAr) sampling electromagnetic calorimeter and a hadronic calorimeter, using iron as absorber and scintillating tiles as active material. The hadronic tile calorimeter covers the central region up to $|\eta| < 1.7$. In the forward and end-cap regions ($1.37 < |\eta| < 4.9$) LAr calorimeters are used for both electromagnetic and hadronic energy measurements. More details on the calorimetry are given in Sec. 4.3. The calorimeters are surrounded by detectors designed to reconstruct muons. These are immersed in a strong toroidal magnetic field, provided by superconducting, air-core magnets. More details on the muon system and magnets are given in Sec. 4.4. An overview of the ATLAS detector is shown in Fig. 4.1.

At nominal conditions bunch-crossings will occur in ATLAS with a frequency of 40 MHz at around 25 proton-proton-collision events per bunch-crossing. Only a small fraction of these events will be interesting for offline analyses and events can only be stored at a rate of 200 Hz. Therefore a fast decision has to be made which events to keep: this is done by the trigger. The ATLAS trigger operates in three stages and will be discussed in Sec. 4.6.

For further analysis the raw detector hits need to be converted into *physics objects* (e.g. electrons). The reconstruction methods for various objects is described in Sec. 4.7. Finally, the data as well as the Monte Carlo generated samples used for performance studies of the HEPTopTagger algorithm and the resonance search are discussed in Sec. 4.8.

Some general requirements on the performance of the ATLAS sub-detectors are:

- Fast and radiation-hard sensors and electronics in combination with high granu-

---

[1] The coordinate system is defined in Sec. 4.1.

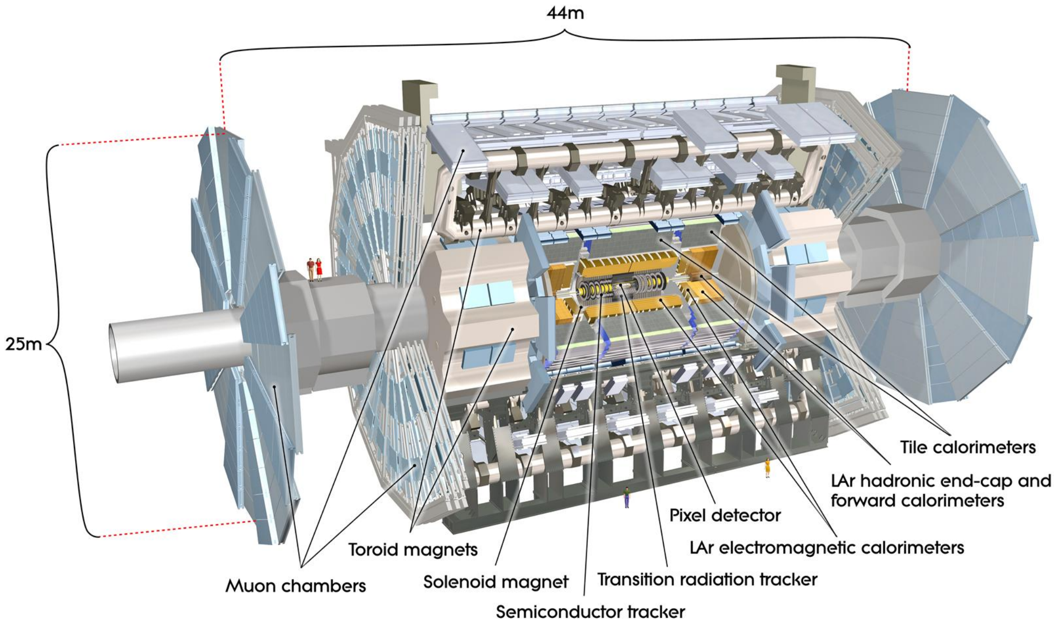

Figure 4.1: Computer generated image of the whole ATLAS detector [89].

larity to withstand the expected large particle fluxes;

- Large coverage in η;
- High reconstruction efficiency and good resolution for charged particle tracks in combination with good vertex resolution for b quark and τ lepton identification;
- High granularity and precision electromagnetic calorimeters for the measurement of electrons and photons as well as large coverage in η by hadronic calorimeters for the reconstruction of jets and missing energy;
- Precise measurement of muon momenta and charge as well as high reconstruction efficiency and
- Efficient and fast trigger decision with good background suppression.

4.1 Coordinate System

In this thesis a right-handed coordinate system with its origin at the nominal interaction point (IP) in the center of the detector will be used. The x-axis points into the LHC ring, the y-axis points upwards and the z-axis points along the beam pipe. Cylindrical coordinates (r, ϕ, θ) — utilizing the symmetry of the detector — will often be used. Here ϕ denotes the azimuthal angle around the beam pipe and θ the polar angle. The pseudorapidity is defined as $\eta = -\ln\tan(\theta/2)$. For massive objects the rapidity $y = \frac{1}{2}\ln\left(\frac{E+p_Z}{E-p_Z}\right)$ is sometimes used instead of the pseudorapidity.

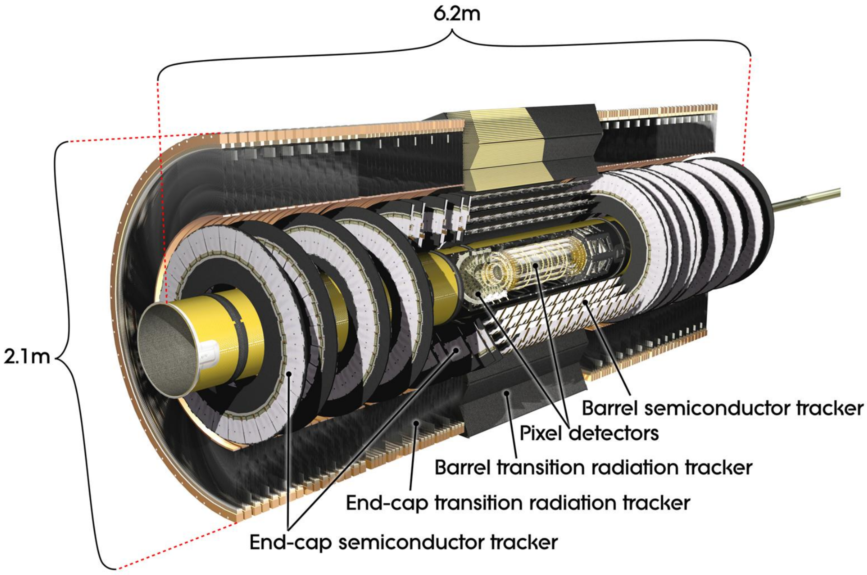

Figure 4.2: Computer generated image of the ATLAS inner detector [90].

Projections of quantities into the x-y-plane (transverse plane) are denoted by a subscript T as in $p_T \equiv \sqrt{p_x^2 + p_y^2}$ for the transverse component of the momentum.

Natural units are used for the measurement of the energy, mass and momentum of particles.

4.2 Inner Detector

The ID is required for the reconstruction of charged tracks as well as for primary and secondary vertices. The reconstruction is performed in the busy environment of ≈ 1000 tracks produced in each bunch-crossing. The ID consists of three independent sub-detectors: the innermost pixel system, the SCT and the outermost TRT. In addition to providing a large lever arm for the reconstruction of tracks, the TRT is also essential for the identification of electron candidates. The sub-detectors will be described in more detail in the following. An overview of the ID is shown in Fig. 4.2. The design resolution for charged tracks is $\sigma_{p_T}/p_T = 0.05\%\, p_T \oplus 1\,\%$ where the unit of p_T is GeV.

4.2.1 Pixel

There are three layers of high-precision pixel sensors around the IP. In the barrel region these layers follow a cylindrical geometry around the beam-pipe. In the forward region the cylinders are closed-off with additional circular end-caps, orthogonal to the z-axis. The three cylinders are situated at radii of $r = 50.5$ mm, 88.5 mm and 122.5 mm and each have a length of 400.5 mm in z. The end-cap disks extend between $88.8 < r < 149.6$ mm and are placed at $|z| = 495$ mm, $|z| = 580$ mm and $|z| = 650$ mm. This geometry leads

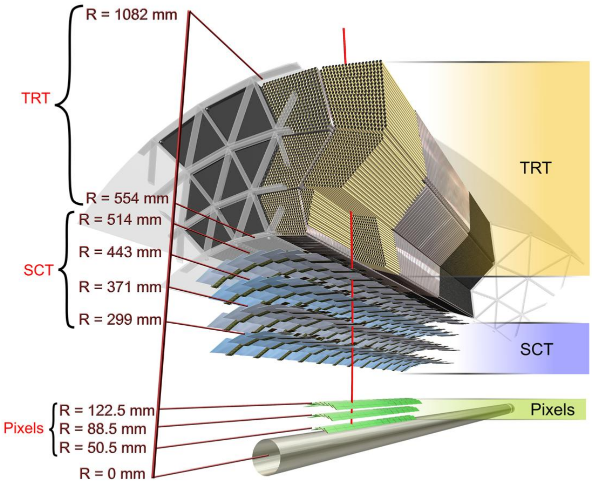

Figure 4.3: Computer generated image of the ATLAS ID showing the structures passed by a simulated charged track with $p_T = 10$ GeV [90].

to an overall coverage of the pixel system of $|\eta| < 2.5$ and is illustrated in Fig. 4.3. A charged track on average passes three pixel layers.

Altogether 1744 identical pixel sensors with 47232 pixels per sensor are used. The total number of read-out channels is 80.4 millions as due to reasons of space some pixels per sensor are combined. The sensors have a thickness of $250\,\mu$m while the nominal pixel size is $R - \phi \times z = 50 \times 400\,\mu\text{m}^2$ (10 % of the pixels are larger with a size of $50 \times 600\,\mu\text{m}^2$). The high resolution of the pixel detectors is important for precise track and vertex reconstruction close to the IP. The innermost pixel layer is especially important for the measurement of secondary vertices.

The pixel detectors are situated closely to the IP and will therefore receive a high radiation dose. To provide constant performance during the planned duration of operation several measures have been taken. Pixel detectors are made out of oxygenized n-type wafers leading to good radiation tolerance. The initial operation voltage is 150 V but this can be increased up to 600 V to retain high charge-collection after long operation. To further reduce noise effects the pixel sensors are operated at a temperature of $-5\,^\circ$C to $-10\,^\circ$C.

For read-out purposes the pixels are connected via In or PbSn bump-bonding to 16 front-end ASIC chips per sensor. To guarantee radiation hardness, chips are prepared using thin gate oxide technology and special layout techniques. Fiber-link cables are used to transfer the signal to the counting room where it is received by optical/electro converters.

4.2.2 Silicon Microstrip

Further away from the IP microstrips are used instead of pixel sensors. The geometry of the SCT is similar to the pixel detector with four cylindrical layers at radii of $r = 299$ mm, $r = 371$ mm, $r = 443$ mm and $r = 514$ mm at a (half) length of $|z| = 749$ mm. The different barrel layers of the SCT can be seen in Fig. 4.3. On each side of the IP nine circular end-caps are mounted at z values between 853.8 mm and 2720.2 mm. The angular coverage extends to $|\eta| < 2.5$. All parts of the SCT are constructed as double-layers with a stereo-angle of 40 mrad. A track will traverse four double-layers, leading to a maximum of eight measurements. Due to its larger radius and number of measurements per track the SCT is a critical complement to the pixel detector.

There are 768 active strips per SCT sensor with a length of $\approx 12\,\mathrm{cm}$, an average pitch of $80\,\mu\mathrm{m}$ and a thickness of $285\,\mu\mathrm{m}$. A SCT module is formed by four sensors (two on each side) and the SCT consists of 4088 modules. The total active surface of the SCT modules is $63\,\mathrm{m}^2$. A p-in-n technology has been used for the SCT sensors which are operated at voltages between 150 V and 350 V depending on the amount of irradiation. The SCT is operated at the same temperature as the pixel detector. As for the pixel system, radiation tolerant ASIC chips and fiberoptic cables are used for read-out.

4.2.3 Transition Radiation Tracker

The drift (straw) tubes — forming the TRT — have a diameter of 4 mm at a wall thickness of $70\,\mu\mathrm{m}$ and a length of 144 cm in the barrel (divided in half at $\approx \eta = 0$). In the additional end-cap the tubes are arranged radially with a length of 37 cm.

Electrically, the straw tube acts as cathode while a wire crossing the tube acts as anode. The wire material is 99.95 % pure tungsten, plated with a thin gold layer. The potential difference between cathodes and anodes is $\approx 1500\,\mathrm{V}$ leading to a gain of $\approx 3 \cdot 10^4$ in the xenon, CO_2 and oxygen gas mixture used.

Extending up to $|z| < 712\,\mathrm{mm}$ and covering the range $563 < r < 1066\,\mathrm{mm}$ in the barrel region, the TRT is the outermost active region of the ID. End-caps are placed on each side of the IP at $848 < |z| < 2710\,\mathrm{mm}$ with a radial coverage of $644 < r < 1004\,\mathrm{mm}$ — leading to an η coverage of $|\eta| < 2$. The geometry of the TRT is shown in Fig. 4.3. It has a total of 351 000 read-out channels and is operated at room temperature.

The TRT contains up to 73 layers in the barrel and 160 planes in the end-cap providing on average 36 — two dimensional — measurements per charged track. This larger number of measurements, in combination with a longer measured track length than in the pixel and SCT detectors, contributes to the overall track resolution. By measuring the radiation coming from the transition between straws and gas in the xenon-gas mixture the TRT is also critical for electron identification.

In the barrel the TRT is comprised of three rings, each holding 32 modules. In the end-caps two independent sets of wheels per side are used: one set of twelve wheels and one of eight. The analogue signal processing of the TRT — distinguishing hits from minimum ionizing particles and transition radiation — is done using ASIC chips directly on the detector. The data are then serialized, the electrical signals are converted to optical signals and sent out using fiber-link cables.

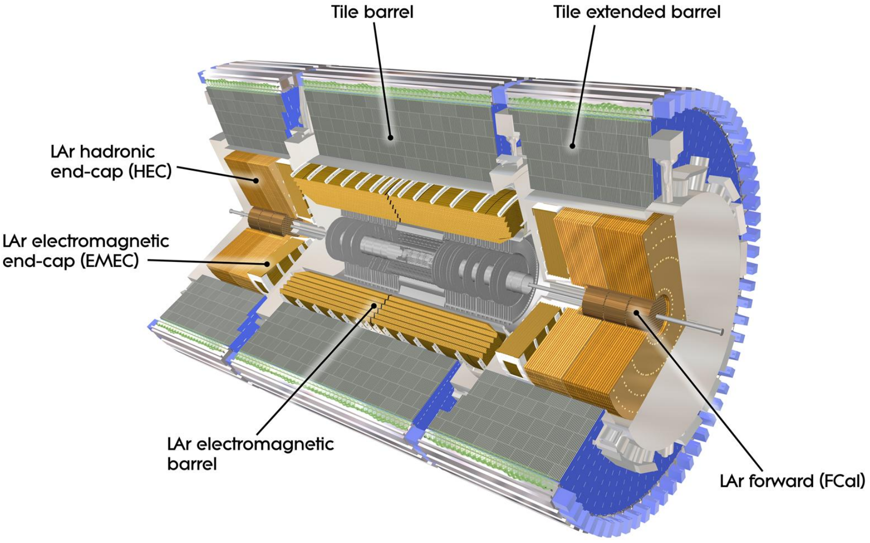

Figure 4.4: Computer generated image of the ATLAS calorimeters [91].

4.2.4 Solenoid Magnet

A strong magnetic field in the ID is essential for the reconstruction of track momenta. For this purpose, a 2 T superconducting solenoid is installed parallel to the beam axis, between the TRT and the calorimetry system, at $2.46 < r < 2.56\,\mathrm{m}$ with a length of 5.8 m.

Altogether ≈ 1200 windings of NbTi-strands are used. To reach superconductivity the magnet is operated at a temperature of 4.5 K. A low radiation length before the calorimeters is critical for precise measurements of the energy. Therefore the magnet shares the cooling vessel with the LAr calorimeter. The total mass of the magnet coil is 5.4 t and the total stored energy is 40 MJ.

4.3 Calorimeters

ATLAS utilizes two different technologies for the energy measurement of hadronic and electromagnetic (EM) showers: liquid argon (LAr) and tile calorimeters. Both are built out of layers that initiate particle showers alternating with layers in which the energy deposit is measured (*sampling calorimeter*). In the central region, over the η range also covered by the ID, a high granularity LAr EM calorimeter provides a precise measurement of electron and photon energies. In other regions LAr and tile calorimeters with coarser granularity are used for the reconstruction of jets. The overall geometry of calorimeters is shown in Fig. 4.4 and the various sub-detectors are described in more detail in the following.

4.3.1 Electromagnetic Calorimeters

The LAr EM calorimeter consists of a barrel part, covering up to $|\eta| < 1.475$ and two end-caps with a range of $1.375 < |\eta| < 3.2$ designed for an energy resolution of $\sigma_E/E = 10\,\%/\sqrt{E} \oplus 0.7\,\%$. The unit of E is GeV.

The barrel is built out of two halves with a small gap at $z = 0$. The length of a half-barrel is 3.2 m, the inner (outer) radius is 2.8 m (4 m) and its weight is 57 t. The end-caps wheels are 63 cm thick and extend from $r = 330\,\text{mm}$ to $r = 2098\,\text{mm}$

The barrel consists of 1024 lead absorber plates with a thickness between 1.13 mm and 2.5 mm to initiate particle showers. The absorber is built in an accordion geometry to provide symmetry in ϕ and to avoid projective azimuthal cracks. Between the lead absorbers are gaps with a thickness of $\approx$ 4mm that are filled with LAr. The LAr is ionized by the passing of particles from the shower and the electron current is measured. LAr is chosen as active material because of its linear response and intrinsic radiation hardness. In the middle of the gaps the electrodes are placed. The EM calorimeter is operated at a nominal voltage of 2000 V.

Up to $|\eta| < 2.5$ the EM calorimeter consists of three active layers that can be read out separately. This allows the measurement of longitudinal shower development and can be used for particle identification. The first layer has a very fine granularity in $\eta \times \phi$. The second layer is built to collect most the energy of the EM shower and has a granularity of $\eta \times \phi = 0.025 \times 0.025$ in the central region. The third layer is designed to measure the tail of EM showers and is less finely segmented. The geometry of a barrel module is shown in Fig. 4.5. In the precision physics region ($|\eta| < 1.8$) an additional pre-sampler — a layer of active material without additional absorber material — is installed to measure showers initiated in the non-instrumented parts of the ID (*dead material*). At $|\eta| > 2.5$ there are only two layers and the overall granularity is more coarse.

The total thickness as multiples of the radiation length X_0 is shown in Fig. 4.6. It varies as a function of η and is between $22\,X_0$ and $30\,X_0$ up to $|\eta| < 0.8$ and $24\,X_0$ and $30\,X_0$ up to $|\eta| < 1.3$ in the barrel. The total thickness of the end-caps is $24\,X_0$ to $36\,X_0$.

4.3.2 Hadronic Calorimeters

Outwards from the EM barrel calorimeter, the hadronic tile calorimeter it situated. It consists of a cylindrical barrel part covering up to $|\eta| < 1$ with a length of 5.8 m and a radial extension of $2.28 < r < 4.25\,\text{m}$. The barrel is augmented by an extended barrel, providing coverage between $0.8 < |\eta| < 1.7$. Additional steel-scintillator tubes help to estimate the energy loss in the uninstrumented region. The tile calorimeter is designed for a jet resolution of $\sigma_E/E = 50\,\%/\sqrt{E} \oplus 3\,\%$.

The tile calorimeter is segmented in three layers with a thickness of $1.5\,\lambda$, $4.1\,\lambda$ and $1.8\,\lambda$ in the barrel and $1.5\,\lambda$, $2.6\,\lambda$ and $3.8\,\lambda$ in the extended barrel. Here λ denotes the hadronic interaction length.

Steel plates with a width between 4 mm and 5 mm are used as absorbers while 3 mm thick scintillating tiles are the active material. Ionizing particles will produce UV scintillation light in the polystyrene base material. The material is doped with fluorine to convert this UV scintillation light to the optical spectrum. At the edge of the tiles

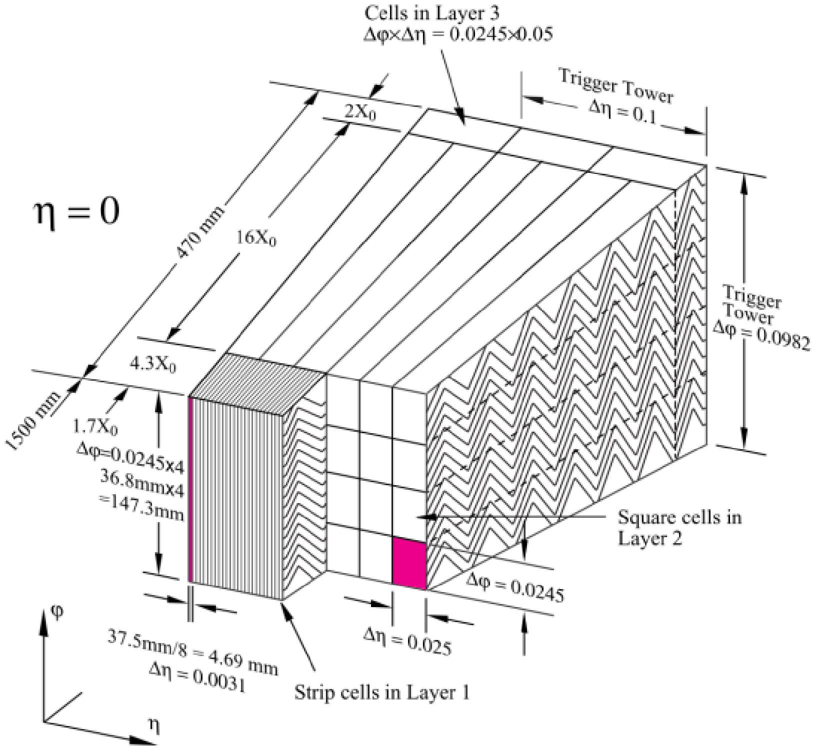

Figure 4.5: Diagram of the three layers of a barrel module in the EM calorimeter [17] showing the cell-size in different layers. The size of a *trigger tower*, the collection of cells used in the trigger system, is also shown.

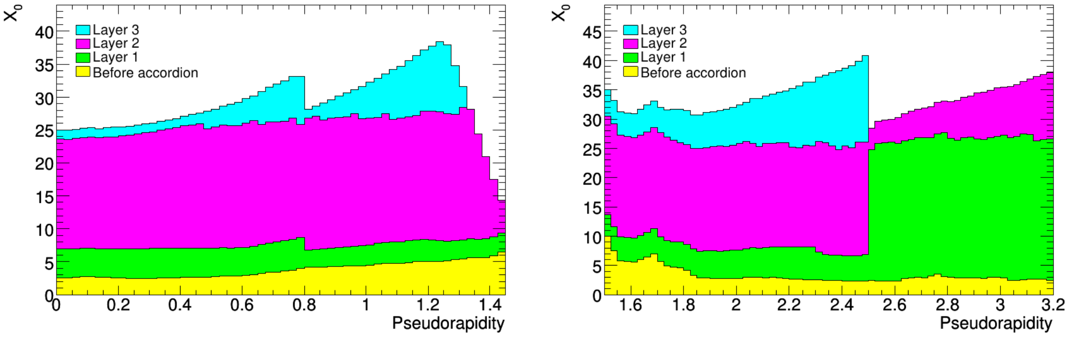

Figure 4.6: Total amount of material before and in the electromagnetic calorimeter as a function of $|\eta|$ for the (left) central and (right) forward regions. The material is measured in multiples of the radiation length X_0 [17].

the light is picked up by fiber-link cables which further shift the signal to longer wave lengths. It is then read-out by photo-multiplier tubes.

Two additional wheels on each side form the hadronic end-cap calorimeter (HEC) covering $1.5 < |\eta| < 3.2$. It is placed behind the EM end-cap and uses similar technology. Copper plates with a thickness between 20 mm and 50 mm act as absorber plates with

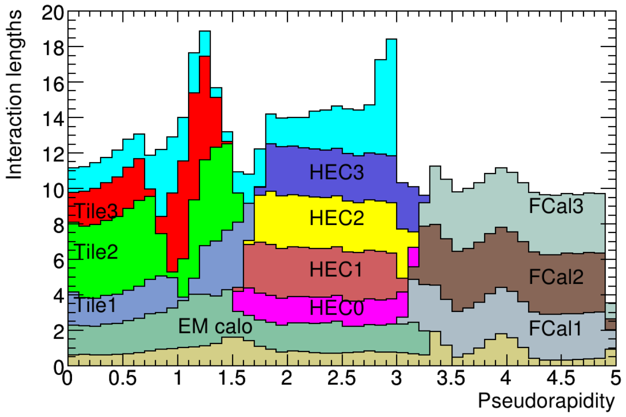

Figure 4.7: Total amount of material before and in the hadronic calorimeter as a function of $|\eta|$. The material is measured in multiples of the interaction length [17].

LAr as active material. In each of the 8.5 mm gaps between the absorber plates three electrodes are placed. The HEC is operated at a nominal voltage of 1800 V.

The most forward part of the hadronic calorimeter, the forward LAr calorimeter (FCal) extends the η range covered by calorimetry up to $3.1 < |\eta| < 4.9$. The FCal is designed for a resolution of $\sigma_E/E = 100\,\%/\sqrt{E} \oplus 10\,\%$. As the particle flux at this pseudo-rapidity is very large, the FCal is positioned at $z = 4.7$ m to reduce the amount of radiation initiated by neutrons (*neutron albedo*) that reaches the ID. To further mitigate radiation effects it is designed very densely. Three modules are used. One copper layer is used mostly for the measurement of EM showers while two tungsten layers provide containment of hadronic showers. The active material LAr is contained in gaps in the metal matrix. To avoid ion buildup these gaps are smaller than in the EM calorimeter. The total thickness of the FCal is $10\,\lambda$. This is illustrated in Fig. 4.7.

4.4 Muons

The outermost ATLAS sub-detector is the muon spectrometer. Muons are deflected in a strong magnetic field provided by superconducting air-core magnets arranged in a toroidal geometry. Monitored drift tubes (MDT) are built to precisely measure the track parameters for $|\eta| < 2.7$ ($|\eta| < 2.0$ for the innermost layer) supported by cathode strip-chambers (CSC) for $2.0 < |\eta| < 2.7$. For triggering, resistive plate chambers (RPC) are used up to $|\eta| < 1.05$ and thin gap chambers (TGC) extend the muon trigger capabilities to up to $|\eta| < 2.4$.

For muons with a p_{T} of 1 TeV the total sagitta along the z-axis is around 500 μm. A targeted momentum resolution of $\approx$ 10% translates to a maximal positional uncertainty on z (or r in the forward detectors) of $\approx 50\,\mu$m.

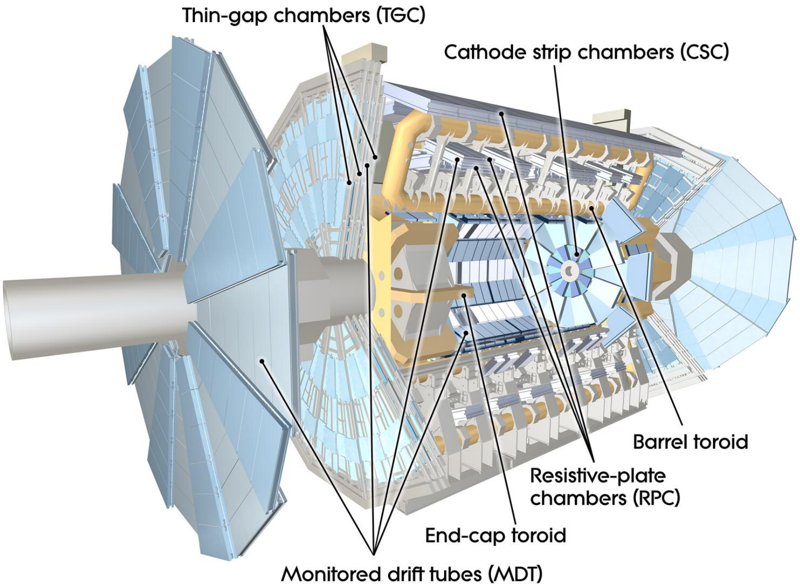

Figure 4.8: Computer generated image of the ATLAS muon spectrometer [92].

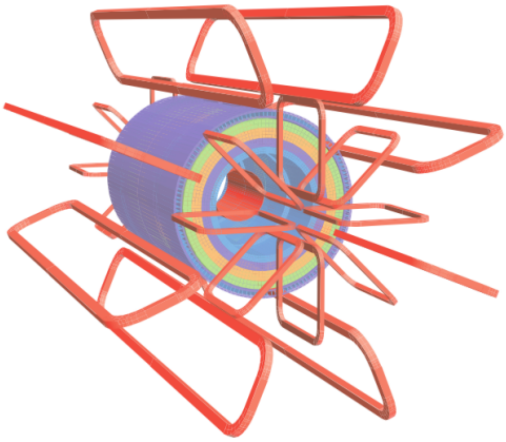

Figure 4.9: Image of the geometry of the ATLAS magnets [17].

4.4.1 Toroid Magnets

The strong magnetic fields necessary for the bending of high-p_T muon tracks are achieved using three toroidal magnets: one in the barrel and 2 in the end-caps. Each toroid consists of eight magnets and is symmetric around the beam axis. The geometry of the magnets can be seen in Fig. 4.9.

The barrel magnet has an outer diameter of 20 m and a length of 25 m. The average magnetic field in the barrel (for $|\eta| < 1.4$) is $\approx 0.5\,\mathrm{T}$. The toroid endcap magnets provide a field of $\approx 1\,\mathrm{T}$ for $1.6 < |\eta| < 2.7$ and have a length of 5 m and a diameter of 10 m. The total mass is 830 t for the toroid barrel magnet and 240 t for each of the end-caps.

As for the inner solenoid a Nb-Ti-Cu superconductor, stabilized with Al, is used. The superconducting fibers are wrapped around pancake-shaped coils. At nominal conditions a total energy of 1.6 GJ is stored in the magnets.

4.4.2 Monitored Drift Tubes

The main muon precision-tracking detector is the MDT. The geometry of the MDT follows the symmetry of the magnets. The MDT consists of three layers of chambers at $r = 5$ m, $r = 7.5$ m, $r = 10$ m in the barrel and four wheels at $r = 7.4$ m, $r = 10.8$ m, $r = 14$ m and $r = 21.5$ m in the end-cap region. One chamber consists of three to eight layers of drift tubes. There is a total number of 1150 chambers in the MDT leading to 354 000 read-out channels. The spatial resolution in z per chamber is $\approx 35\,\mu$m while for the other coordinate the position of the drift tube is used.

Drift tubes have a diameter of 29.97 mm and a length between 0.9 m and 2.1 m depending on the position. Tungsten/rhenium wires for collection of ionized particles are positioned concentric with the tube. The drift tubes are filled with an Argon and $C0_2$ gas mixture with a small fraction of H_2O at a pressure of 3 bar. The operating voltage is 3080 V which leads to a maximum drift time of 700 ns.

4.4.3 Cathode Strip Chambers

In the innermost layer of the forward region, the high density of charged particle tracks makes it necessary to use an alternative detector concept. The MDT is replaced with CSC, allowing a higher rate and better time resolution. The CSC are comprised of two disks with eight chambers per disk at $z = 7$ m from the IP and an inner (outer) diameter of 888 mm (2081 mm).

The CSC are multiwire proportional chambers. Copper clad laminate walls are used as cathode planes and Tungsten/rhenium wires as anodes. The potential difference is 1900 V. The central wire of each chambers points radially outwards, the other wires are parallel to it. Both cathode planes are segmented in strips. One is oriented parallel to the wires, the other one orthogonal. The induced charge distribution in the cathodes is measured, providing a spatial precision of $40\,\mu$m in R and 5 mm in ϕ.

4.4.4 Resistive Plate Chambers

Complimentary to the precision measurements by MDT and CSC, additional fast measurements are necessary for triggering. Important requirements are: good spatial and time resolution, measurement of the multiplicity and approximate energy range of muon tracks, determination of the bunch-crossing ID and robustness against random hits. In the central region, up to $|\eta| < 1.05$, the RPC is used for this. It is comprised of three concentric cylindrical layers at $r = 7.8\,$m, $r = 8.4\,$m, and $r = 10.2\,$m and is fully immersed in the toroidal magnetic field.

The two inner layers together are used for the measurement of low-p_{T} tracks (6-9 GeV) while the inner and outer layer provide measuremtents of high-p_{T} tracks (9-35 GeV). The η and ϕ coordinates are measured independently in each layer.

The RPC is constructed using lattices of parallel electrodes with a read-out pitch of 23-55 mm. This wire-free approach simplifies construction and is mechanically more robust. Phenolic-melaminic plastic laminate is used for the plates which are kept at a distance of 2 mm by spacers. The RPC operating voltage is 9.8 kV and the volume is filled with a $C_2H_2F_4$ / Iso-C_4H_{10} / SF_6 gas mixture.

4.4.5 Thin Gap Chambers

In the end-cap region the MDT is augmented by the additional TGC. It has two functions: to provide an additional measurement of the azimuthal coordinate and a fast trigger decision. Two TGC layers are situated and the inner end-cap MDT and seven layers at the middle MDT.

The TGC is a multi-wire-proportional chamber. The radial coordinate is measured by the wire groups, the azimuthal by radial cathode strips. Wires are separated 1.8 mm from each other while the CO_2 and n-pentane filled gas-gap is 2.8 mm wide. Operating at an electric field of 2900 V it provides a good time resolution for the TGC.

4.5 Luminosity

A precise measurement of the luminosity is essential for searches for new particles as well as for precision measurements of the cross-sections of Standard Model particles. In the following the different subdetectors contributing to the measurement of the luminosity are described [87, 93].

The methods used to determine the luminosity can be divided into two categories: measuring the total luminosity (summed over many bunches) via detector currents that are averaged over a longer time (O(10 ms)) and the direct measurement of the luminosity on a bunch-by-bunch basis. The total luminosity is measured using the tile and forward calorimeters, using that the voltage in the calorimeter cells is proportional to the average rate of particles.

Two detectors are used for bunch-by-bunch measurements of the luminosity: BCM (Beam Conditions Monitor) and LUCID (Luminosity measurement using a Cherenkov Integrating Detector). The BCM consists of four diamond sensors, each with a cross-section of $1\,\mathrm{cm}^2$, arranged in cross-shape around the beampipe at $z = \pm 184\,\mathrm{cm}$. LUCID is positioned more forward, at $z = \pm 17\mathrm{m}$. It is comprised of 16 polished aluminum tubes filled with C_4F_{10}. Cherenkov photons created in the gas are detected by photo-multiplier tubes installed as endcaps of the aluminum tubes. The final luminosity used for physics analyses is a combination of measurements from the different subsystems.

The luminosity detectors are calibrated using so-called van-der-Meer scans. In these scans the known luminosity delivered by specially prepared proton beams is compared with the measured luminosity in the detector. The position of both beams is varied in the x-y-plane.

4.6 Trigger and Data Acquisition

The Trigger and Data Acquisition (TDAQ) system decides which events are to be stored for offline analysis — decisions at the trigger stage are termed *online*, later analysis steps are called *offline* — and manages the read-out of these events from the detector. It is comprised of three subsequently executed levels: Level 1 (L1), Level 2 (L2) and Event Filter (EF). Each level uses additional information to improve the decision provided by the previous level. L1 is implemented using custom-made electronics while L2 and EF (together referred to as High Level Trigger (HLT)) are executed on standard computer hardware. Information from the various sub-detectors is used for triggering. Triggering on the following objects is possible: high p_{T} muons, electrons, photons, jets, τ leptons decaying into hadrons, missing E_T and total transverse energy.

The trigger menu is the overall configuration of the trigger: it defines the thresholds for different trigger types, which L1 trigger should be used as input to which L2 trigger (and which L2 trigger as input to which EF trigger). At all three levels so-called prescale factors can be defined for each trigger. A prescale factor reduces the output rate of a trigger chain by only accepting 1 in n events (where n is the prescale factor). For the analysis presented in this thesis only unprescaled triggers are used.

4.6.1 Level 1

At L1 the event rate is reduced from the bunch-crossing frequency of 40 MHz to 75 kHz. Because the full detector read-out information is stored in pipeline buffers during processing, the total time available for decision is $2.5\,\mu$s. $1\,\mu$s of this time is allocated for transmitting the information out of the detector. At L1 up to 256 menu items (different combinations of thresholds and object multiplicities) can be implemented. The L1 also assigns the bunch-crossing ID to events. Information for the L2 is passed on in the form of regions-of-interest (RoI). A RoI is a region in $\eta \times \phi$ with interesting features (e.g. a jet above an energy threshold).

Two detector subsystems are used at L1: the calorimeters and the muon detectors. For triggering on muons the RPC and TGC sub-detectors are utilized. Muon tracks are identified by comparing the measured hit-patterns with expected tracks for different energies. The coincidence hits along a *road* (expected particle trajectory) are used for this. The width of this road is determined by the p_{T} threshold. Six independent p_{T} thresholds are possible. Information from all calorimeters (EM and hadronic, barrel, end-cap, and forward) is used for the identification of electrons, photons, jets, τ leptons, missing E_T and total transverse energy, albeit with a reduced granularity of 0.1×0.1 in $\eta \times \phi$ for most of the detector. For each calorimeter trigger type, 4–16 different thresholds are available.

4.6.2 High Level Trigger

When an event is accepted on L1, the full detector is read out to the DAQ system via 1574 connections, each having a bandwith of 160 MB/s. This information is stored in read-out buffers to be accessed by the HLT systems. At L2, the full detector granularity is used, however only in the regions of interest. This amounts to $\approx 2\,\%$ of the total event data. The additional use of inner detector tracking is especially important for the identification of electron and photon candidates. At L2 the event rate is reduced 20-fold to 3.5 kHz with a latency of 40 ms.

At the EF fully-reconstructed events are analyzed using offline methods to arrive at the final trigger decision. This decision is made in 4 s and the average EF output rate is 200 Hz. At an event size of $\approx 1.3\,\mathrm{MB}$, the limiting factor is the speed with which events can be stored for later analysis.

4.7 Object Reconstruction

Before the measurements from the sub-detectors can be used for offline analysis, physics objects such as muons or jets need to be reconstructed from the raw detector hits. In the following an overview of the reconstruction methods used for tracks, vertices, electrons, muons, jets, b-jets and missing transverse energy is given [94].

4.7.1 Tracks

Inner-detector tracks are reconstructed [95] using the high granularity information from the pixel and SCT detectors as well as hits recorded by the TRT. In a pre-processing step the raw hits from the pixel and SCT detectors are converted to clusters and the TRT timing information is converted to calibrated drift circles. Primary charged particles — particles with a mean lifetime larger than $3 \times 10^{-11}\,\mathrm{s}$, produced directly in the pp interaction or resulting from decays of intermediate particles with a mean lifetime shorter than $3 \times 10^{-11}\,\mathrm{s}$ — are reconstructed using an inside-out method. Following this approach, track seeds are calculated from clusters in the pixel detector as well as the inner SCT layer. These seeds are then extended outwards through the SCT — using a combinatorial Kalman filter — to arrive at track candidates. Outlying clusters, ambiguities and fake tracks are removed before the track is extended into the TRT. In a final step the tracks are refit using the information from all three detectors.

For the reconstruction of tracks from secondary charged particles — secondary particles are the products of interactions of primary particles — a back-tracking approach is used. In the back-tracking method the tracking starts at the TRT and extends inwards by adding hits from the SCT and pixel systems.

4.7.2 Vertices

The position of the primary pp interaction (primary vertex) is determined using an adaptive iterative vertex finder [95]. The input to the vertex reconstruction are the z-positions of tracks along the beam pipe. These seeds are used — together with nearby tracks — in an iterative χ^2 fit. Tracks are given a weight — depending on the compatibility with the vertex — in the fit which depends on χ^2 and which is changed iteratively. Tracks with a distance of at least 7σ to the vertex are used as new seeds. This procedure is repeated until no new seeds are found. The position of the beam-spot is used as an additional constraint in finding the vertex. After the iterative vertex finding, the vertex and tracks are refit so that the tracks originate from the vertex. If multiple primary vertex candidates are found, the one with the highest $\sum p_{\mathrm{T}}^2$ of the tracks associated with it is used.

4.7.3 Electrons

Electrons are reconstructed using the combined information from the ID and calorimeter sub-detectors. To exploit the full physics potential of the LHC, efficient electron identification over three orders of magnitude in momentum — from a few GeV to a few TeV — is necessary. Standard electron reconstruction is seeded from clusters of cells in the EM calorimeter which are then matched to tracks.

For finding seeds, the barrel and end-cap EM calorimeter is segmented into cells of 0.025×0.025 in $\Delta\eta \times \Delta\phi$. The energy measured in different longitudinal layers is separately summed up for all cells. A sliding-window algorithm with a size of 3×5 cells in $\Delta\eta \times \Delta\phi$ is then used to search for clusters. If the energy in such a window exceeds 3 GeV it is called a pre-cluster. The final energy and position is then calculated using a 3×3 sub-window to reduce noise. If two clusters are too close, only the more energetic one is used.

The electron reconstruction then proceeds by searching for a matching ID track within a cone of 0.05×0.10 in $\Delta\eta \times \Delta\phi$ around the position of the cluster after extrapolation to the EM calorimeter. Tracks flagged as originating from photon conversion in the ID are ignored and electrons need to have a transverse impact parameter $d_0 < 1\,\mathrm{mm}$ and a longitudinal impact parameter $z_0 < 2\,\mathrm{mm}$ with respect to the primary vertex with the highest $\sum p_{\mathrm{T}}^2$ of the tracks associated with it.

Central electrons are reconstructed up to $|\eta| < 2.47$ excluding the crack between barrel and end-cap calorimeters by requiring $|\eta|$ outside of the range $1.37 - 1.52$. For these requirements, the η-coordinate of the cluster with respect to the primary vertex position is used. Electron identification requirements on the shape of the shower in the calorimeters and the hits in different parts of the tracking system are placed. Clusters are also removed if so called object quality requirements — aimed at rejection of non-functional cells, or cells with very high levels of noise — are not met.

4.7.4 Muons

Isolated muons are an important signature for various analyses and the ATLAS detector has been designed for the measurement of muons with a p_{T} up to 1 TeV. For muon momenta between 30 and 200 GeV both the ID and muon spectrometer measurements contribute approximately equally to the reconstruction of muon tracks. For lower (higher) muon p_{T} the ID (muon spectrometer) becomes more important. The muon reconstruction can be supported by calorimeter information by utilizing the minimum ionizing signature of muons.

Two different families of algorithms for the reconstruction of muons exist in ATLAS: *Staco* and *MuID*. Each of these provides four different types of muon reconstruction:

Standalone: Muons are reconstructed from track segments in each of the three muon stations;

Inner Detector: Only the ID is used;

Tagged Muons: The muon track is reconstructed using the ID and matched with a muon track segment from the first muon station and

Combined: Full information from ID and the muon stations is used for reconstruction.

In this thesis combined muons reconstructed using the MuID method are used. The reconstruction starts with an inner detector track and a covariance matrix. These are extended by measurements from the three muon stations. In the process the possibility of multiple scattering and energy loss in material and the magnetic field is taken into account. A χ^2 is calculated to assess the agreement and muons candidates are accepted if the value is below a threshold.

For further analysis central muons with $|\eta| < 2.5$ and a longitudinal impact parameter $z_0 < 2\,\mathrm{mm}$ with respect to the primary vertex are considered. Additional requirements on the number of hits in the pixel, SCT, TRT and muon sub-detectors are set.

4.7.5 Jets

For the reconstruction of hadronic jets, information from EM and hadronic calorimeters is used. In a first step, the individual measurements in the calorimeter (cells) are grouped using a topological clustering algorithms [65, 96]. These *topoclusters* are then combined into jets using the FastJet software [97, 98].

The topological clustering algorithm takes the cells from all calorimeters as input. If the energy of a cell is at least four times the noise threshold, it is used as a seed. The noise threshold is calculated individually for all cells and is the sum of electronic-noise and pile-up induced noise. A seed is iteratively extended in all three dimensions by all cells with an energy of at least two times the noise threshold. In a last step all connected cells are added to the cluster.

These topological clusters are then processed using jet clustering algorithms as described in Sec. 2.4. The default algorithm in ATLAS is anti-k_t with a distance parameter of either $R = 0.4$ or $R = 0.6$. Only topoclusters with positive energies are used.

The uncalibrated energy recorded by the calorimeter cells is at the so-called *electromagnetic scale* (*EM scale*). As a first step *local calibration* (*LCW scale*) is performed: according to the density of energy depositions, clusters are classified as electromagnetic or hadronic and then corrected accordingly [99]. These corrections are derived using single pion MC simulated samples. In a second step the jet energy is corrected to the *true* energy of simulated hadron jets. This is done using a numerical inversion technique derived on simulated dijet events. Two calibration schemes are used: the numerical inversion is either done after the local calibration (*LC+JES*) or the intermediate LCW scale is omitted (*EM+JES*).

The default anti-k_t jets are reconstructed using the EM+JES technique, jets used in the HEPTopTagger algorithm are calibrated with the LC+JES technique. Additionally the cluster-directions are corrected so that their four vectors point towards the primary vertex.

4.7.6 *b*-Jets

A combination of calorimeter and tracking information can be used to separate jets originating from the decay of a b quark from those that are from lighter quark and gluon jets.

Jets from b quarks have several distinguishing properties. Most importantly, the long lifetime of B hadrons of $\approx 1.5\,\mathrm{ps}$ can lead to a displaced decay vertex with a distance of a few mm with respect to the primary vertex. Due to hard fragmentation, the B hadron typically carries a large fraction of the b-quark momentum. The high mass of B hadrons of at least 5 GeV leads to a larger momentum of decay products transverse to the jet axis and a wider opening angle.

Different b-tagging algorithms are available in ATLAS [100]. The SV1 method uses three variables pertaining to the secondary vertex, such as the mass of all tracks associated to the vertex, to tag b quarks. The IP3D algorithm uses the longitudinal and transversal impact parameters of tracks with respect to the primary vertex for b-quark identification. Discrimination in the JetFitter algorithm is based on the topology of b- and c-quark decays and uses similar variables to the SV1 method together with additional variables such as decay lengths.

The b-tagging algorithm used for the analysis in this thesis is MV1 [101]: a neuronal network based on the output of SV1, IP3D and JetFitter algorithms. The output of the neuronal network is one value, the so-called b-tagging weight. If the b-tagging weight exceeds a threshold (*working point*) the jet is accepted as originating from a b quark (*tagged*). The relation between efficiency and mis-tag rates is presented in Fig. 4.10 for different algorithms. The efficiency with which b-jets are found is inversely correlated with the purity of the selection. The rejection power of the MV1 algorithm against light-jets is superior. Using a JetFitter algorithm optimized for c-jet rejection (JetFitterCombNNc) can reduce the c-jet fraction at low values for the signal efficiency by up to a factor of three with respect to the MV1 algorithm.

For the fully hadronic resonance search (Sec. 7) the MV1 algorithm at a b-tagging working point with a nominal efficiency of 70 % is used. At this working point the light-jet (c-jet) rate is reduced by approximately a factor of 100 (8).

4.7.7 Missing Energy

An important quantity in the transverse plane is the missing E_T (or $E_{\mathrm{T}}^{\mathrm{miss}}$). It is defined as [102]:

$$E_{x,(y)}^{\mathrm{miss}} = E_{x,(y)}^{\mathrm{miss,\ calo}} + E_{x,(y)}^{\mathrm{miss,}\ \mu}$$

where $E_{x,(y)}^{\mathrm{miss,\ calo}}$ ($E_{x,(y)}^{\mathrm{miss,}\ \mu}$) is the contribution of clusters associated to objects reconstructed by the calorimeters (of muon tracks reconstructed in the muon spectrometer) to the $E_{\mathrm{T}}^{\mathrm{miss}}$. The contributions to $E_{x,(y)}^{\mathrm{miss,\ calo}}$ are:

$$E_{x,(y)}^{\mathrm{miss,\ calo}} = E_{x,(y)}^{\mathrm{miss.}\ e} + E_{x,(y)}^{\mathrm{miss.}\ \gamma} + E_{x,(y)}^{\mathrm{miss.}\ \tau} + E_{x,(y)}^{\mathrm{miss.\ jets}} + E_{x,(y)}^{\mathrm{miss.\ calo\text{-}}\mu} + E_{x,(y)}^{\mathrm{miss.\ cell\text{-}out}}.$$

The individual terms in the sum are calculated by adding the four-momenta of calorimeter cells associated to:

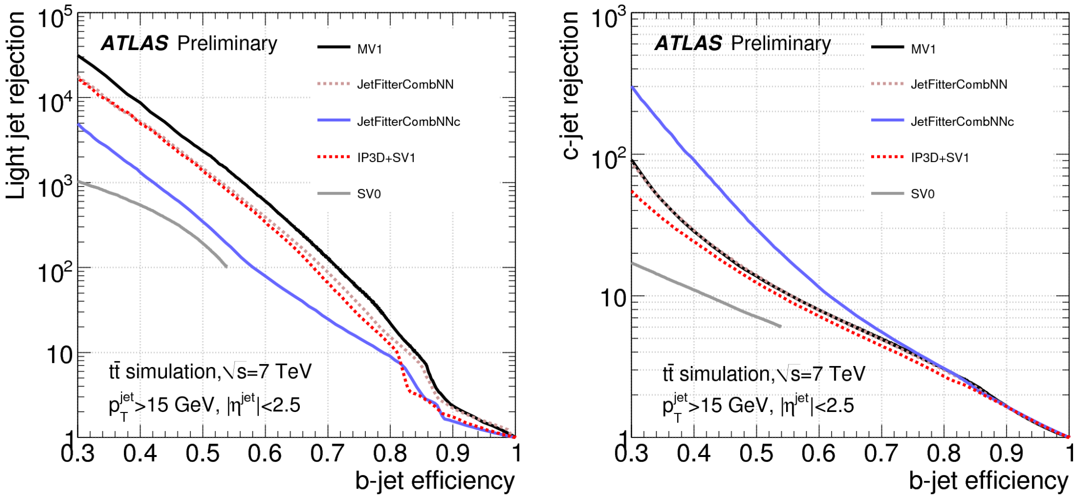

Figure 4.10: The (a) light-jet rejection and (b) c-jet rejection as a function of the b-tagging efficiency for different b-tagging algorithms. The efficiencies and mis-tag rates are estimated using simulated $t\bar{t}$ event [101].

- electrons ($E_{x,(y)}^{\text{miss. } e}$);
- photons ($E_{x,(y)}^{\text{miss. } \gamma}$);
- τ leptons ($E_{x,(y)}^{\text{miss. } \tau}$);
- jets ($E_{x,(y)}^{\text{miss. jets}}$);
- muons ($E_{x,(y)}^{\text{miss. calo-}\mu}$) and
- topoclusters which are not associated to other objects ($E_{x,(y)}^{\text{miss. cell-out}}$).

The $E_{\text{T}}^{\text{miss}}$ contribution from the muon spectrometer ($E_{x,(y)}^{\text{miss, } \mu}$) is calculated as -1 times the sum of the four-momenta of muon tracks.

4.8 Data and Monte Carlo Samples

For the HEPTopTagger performance studies (Sec. 6) and the fully hadronic resonance search (Sec. 7) data corresponding to an integrated luminosity of $4.7 \pm 0.2\,\text{fb}^{-1}$ [87, 93], recorded during the 2011 LHC data taking are used. During this period, the mean number of interactions per bunch-crossing, $\langle\mu\rangle$, varied between 6 and 17. This distribution of $\langle\mu\rangle$ is shown in Fig. 3.6.

Events need to fulfill baseline quality criteria to reduce contamination from detector noise and read-out problems. These data quality criteria are defined individually for all sub-systems and data-taking periods. In addition to requiring a fully operational ATLAS detector and stable LHC beams, measures are taken to reject non-collision backgrounds: the primary vertex — reconstructed from at least two tracks with $p_T > 400\,\mathrm{MeV}$ — has to be consistent with the LHC beam spot.

For the simulation of the various physics processes occuring in LHC collisions different Monte Carlo (MC) programs are used. Many processes with two incoming and two outgoing particles ($2 \rightarrow 2$) as well as $2 \rightarrow 1$ and $2 \rightarrow 3$ processes are implemented in the PYTHIA MC generator [103]. The matrix elements for these processes are calculated at *tree-level* (leading order, LO) and no corrections due to loops or additional vertices are included. Processes with higher particle multiplicities at tree-level can be simulated using the ALPGEN [104] and MADGRAPH [105] generators.

The MC@NLO MC generator allows the calculation of processes including one additional vertex or QCD loop in addition to the tree level process (next-to-leading order, NLO). The NLO calculation of the hard process is matched to simulated parton showers to avoid double-counting of contributions.

SM $t\bar{t}$ events are simulated using the MC@NLO v4.01 generator [106, 107] with CT10 parton density functions (PDFs) [108]. Some Feynman diagrams for the $t\bar{t}$ production at the LHC are presented in Fig. 4.11. In the simulation a top-quark mass of 172.5 GeV is assumed. For the simulation of final-state parton showers, the HERWIG v6.5 [109] program together with the JIMMY v4.31 underlying event model [110] are utilized. The underlying event is the contribution from the interactions of the proton constituents with the exception of the hard interaction [62]. The $t\bar{t}$ production cross section is calculated at approximate next-to-next-to-leading order (NNLO) — including up to two more vertices than the diagram at leading order — in QCD employing the HATHOR v1.2 Monte Carlo program [111] and found to be 167 pb. For the calculation of this cross-section the MSTW2008 90% NNLO PDF sets [36] are used.

The production of leptonically decaying gauge bosons $W \rightarrow \mu\nu$ and $Z \rightarrow \mu\mu$ in association with jets (Fig. 4.12) is simulated with the ALPGEN v2.13 [104] generator interfaced to HERWIG. For the production of hadronically decaying W bosons $W \rightarrow qq'$ the HERWIG program in combination with JIMMY is used. Single top production in the s-channel (Fig. 4.13a), the t-channel (Fig. 4.13b) and the Wt-channel (Fig. 4.13c) is simulated using the MC@NLO generator interfaced to the JIMMY program. QCD multijet events are simulated using the PYTHIA v6.421 MC generator [103]. In Fig. 4.14 two examples for Feynman diagrams contributing to the QCD jet production at the LHC are shown.

For the simulation of the $Z' \rightarrow t\bar{t}$ signal process, the PYTHIA program is used together with the MSTW2008 PDFs [36]. The NLO corrections to the production cross-section of Z' bosons decaying into top quark pairs have been calculated [112]. The ratio of the NLO cross-section to the LO cross-section (called *k-factor*) is estimated to be 1.3 for the Z' mode under consideration. This factor is used to correct the LO prediction obtained using the PYTHIA MC generator by re-weighting events.

The production and decay of KK gluon resonances is simulated using the MADGRAPH v4.4.51 [105] MC generator with the CTEQ6L1 PDFs [37]. For KK gluon events PYTHIA is used to model the parton shower. Depending on the relative phase between the SM $t\bar{t}$ continuum and new resonances, constructive or destructive interference can occur. Such effects are not taken into account in the simulation.

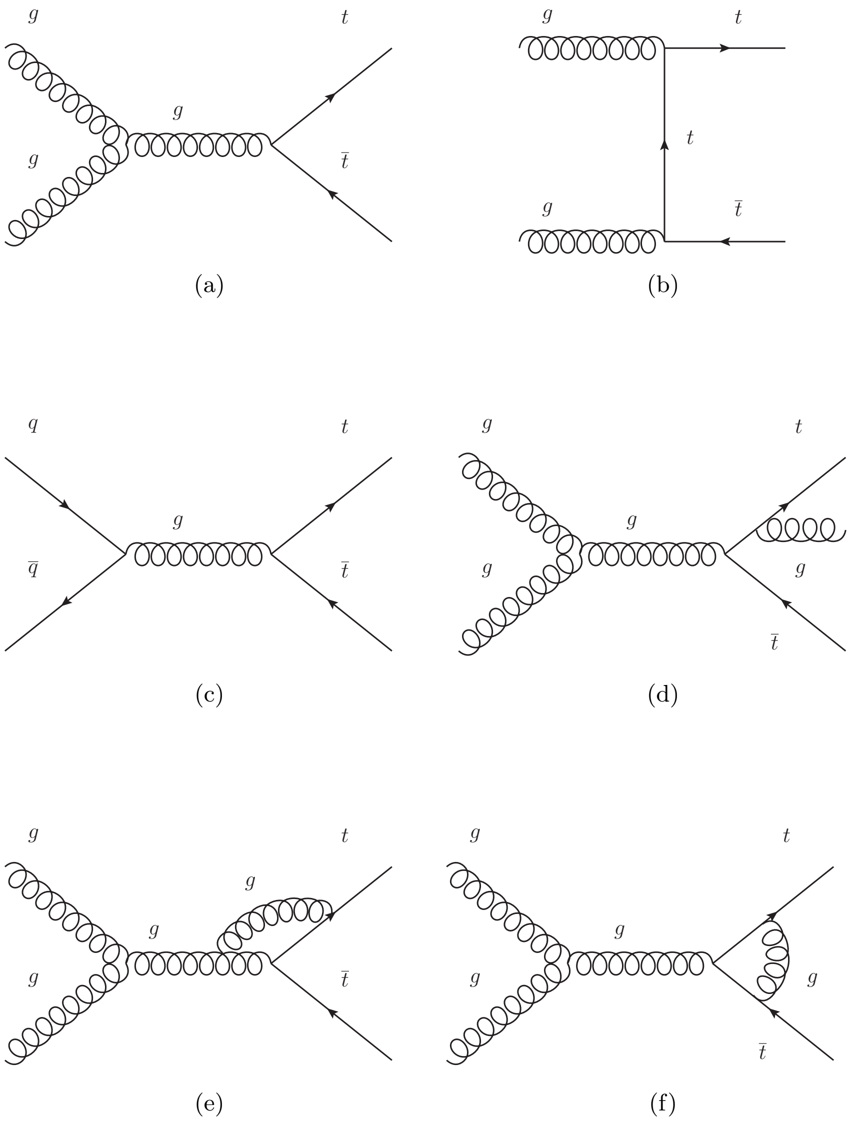

Figure 4.11: Feynman diagrams of (a-c) leading order contributions to the $t\bar{t}$ production at the LHC and of (d-f) examples for diagrams at next-to-leading order in QCD.

Following parton showering and hadronization, the MC events are processed using a full GEANT4 [113] simulation of the ATLAS detector [114]. The same trigger, event, quality and other selection criteria are applied to MC simulation and data. To simulate pile-up, soft *pp* collisions (minimum bias events) are generated with PYTHIA 6.425 [103] using the ATLAS MC11 AUET2B tune [115] and added to the hard scattering events. The number, energy and event weight of minimum bias events is set such that the average

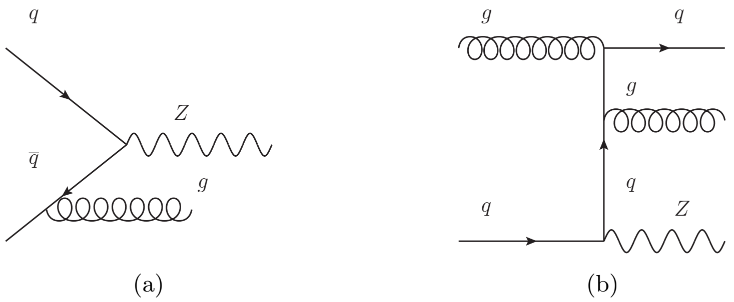

(a) (b)

Figure 4.12: Tree-level feynman diagrams contributing to the production of Z bosons in association with (a) one jet and (b) two jets.

number of interactions per bunch crossing agrees with the measured distributions.

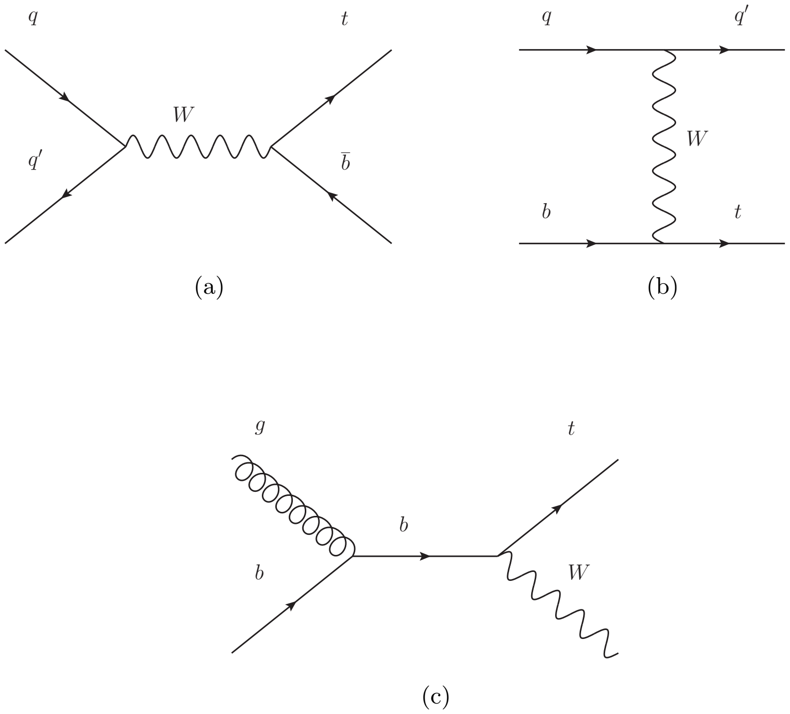

Figure 4.13: Feynman diagrams for the single top quark production at leading order. Shown are (a) the s-channel, (b) the t-channel and (c) the Wt-channel.

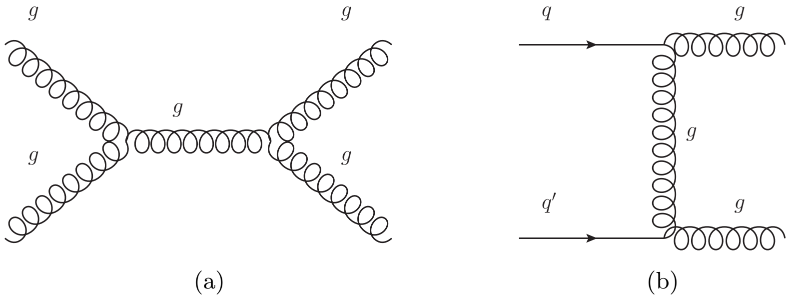

Figure 4.14: Examples of Feynman diagrams contributing at leading order to jet production at the LHC.

Chapter 5

Jet Trigger Performance Studies

The ATLAS [17] Event Filter [116] (EF, outlined in Sec. 4.6) jet trigger [94] is critical for the selection of events containing jets with a high transverse momentum. The EF is executed on events passing the selection at Level 2 and allows a more detailed reconstruction of jets. Therefore a more strict selection can be performed so less-interesting events containing low E_{T} jets, that occur at a high rate, can be surpressed. In the following the performance of the inclusive single jet triggers is studied. Such triggers accept the event if at least one jet with a E_{T} higher than a certain threshold value is found.

During the 2010 data taking period the EF jet trigger was operated in *pass-through* mode — the trigger decisions were recorded but no events were rejected. This was possible because the data rate was low enough so that the L2 trigger could provide sufficient rejection. The initial configuration of the Event Filter (EF) jet trigger utilized the ATLAS Cone [55] jet algorithm ($R = 0.7$) to reconstruct jets from calorimeter trigger towers. EF jets were reconstructed in Regions-of-Interest (RoI) around jets found at Level 2.

Before the beginning of 2010 data taking the ATLAS cone algorithm had already been replaced by the recombinatorial anti-k_t [57] algorithm for offline analyses. As described in Sec. 2.4 this algorithm is infrared and collinear safe and the resulting jet boundaries are robust against soft radiation. To achieve ideal performance in the jet trigger — including better agreement between jet measurements at the trigger stage and offline analysis — it is necessary to also use the anti-k_t algorithm in the EF.

The time between 2010 and 2011 data-taking was used to upgrade the EF jet trigger to correspond more closely to the updated algorithms used for the offline analyses. This means utilizing the anti-k_t (R=0.4) jet algorithm in a full-scan approach on topological clusters of calorimeter cells. Before using the updated configuration for rejecting events, the impact was evaluated by simulating the updated trigger decision (reprocessing) on events recorded in the pass-through mode with an efficiency at the EF stage of 100 %

The reasons for the various changes are explained in more detail in Sec. 5.1 and the used data and object definitions are listed in Sec. 5.2. After describing the performance metrics used to compare the different trigger configurations in Sec. 5.3 the results of the individual comparisons are presented in Sec. 5.4. The results are reviewed in Sec. 5.5. These studies are also summarized in Ref. [117].

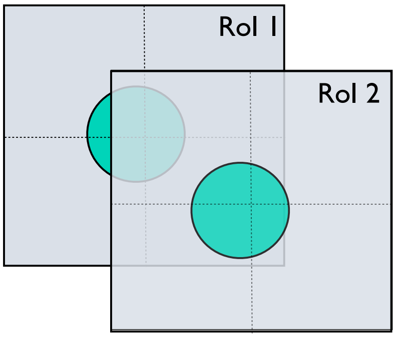

Figure 5.1: Illustration of two overlapping RoIs (grey squares) centered around two jets (green circles) in the η-ϕ-plane. The depicted situation would lead to the upper-left jet being reconstructed twice: once in each RoI [117].

5.1 Motivation

Three changes to the jet reconstruction at the EF are studied in the following:

- replacing the ATLAS Cone jet algorithm by the recombinatorial anti-k_t algorithm;
- switching from RoI based reconstruction to reconstructing all jets in the calorimeter simultaneously (*fullscan*) and
- exchanging trigger towers (Sec. 4.3) with topoclusters (Sec. 4.7.5) as input objects.

The switch to the anti-k_t algorithm is motivated by two factors. Firstly it is collinear and infrared safe. Secondly it is the recommended algorithm for offline jet reconstruction in ATLAS. In the following it will be shown that using the same reconstruction algorithm increases the resolution of the trigger with respect to offline measurements. Therefore tighter selection criteria can be placed on the jets at trigger level, leading to a higher rejection for unwanted events.

For most objects the reconstruction in the EF is only performed in a RoI in η and ϕ[1] centered around directions seeded by the Level 2 trigger (Sec. 4.6). To allow the reconstruction of jets with a typical size of $R = 0.6$ and an axis within a cone with a radius of 0.3 around the RoI direction, the side-length of the RoI has to be at least 1.8. The actual size used for RoI based jet finding is $\Delta\eta = 1.6$ and $\Delta\phi = \pi/2$. Jets far from the RoI axis might not be fully reconstructed as a consequence.

If two jets at Level 2 are close enough, so that their respective RoIs overlap, this region of the detector will be processed multiple times and can result in duplicate jets. This situation is sketched in Fig. 5.1. The duplication of jets can lead to the erroneous statisfaction of multijet signatures. This can happen when a single high-E_T jet passes the threshold and is counted multiple times — once in each RoI.

In events with a high jet multiplicity the total area covered by different RoIs can easily exceed the total area of the calorimeter, leading to an increase in processing time.

---

[1] The coordinate system is defined in Sec. 4.1.

The issues of not fully-reconstructed jets, overlapping RoIs, and increased processing time in high density events can be circumvented by reconstructing the jets in a fullscan approach. This means that if one L2 chain initiates the running of the EF jet finder, the jet algorithms are executed on the complete calorimeter at once. This has the additional advantage of corresponding more closely to the theory perspective on jet finding where the full event is considered at once [57]. The fullscan based jet approach also allows to recover jets that were *lost* due to mismeasurement at Level 2 with the EF trigger.

Using topoclusters not only for offline jet reconstruction but also for jet finding in the EF further increases similarity between these two stages. Only small differences in calibrations, noise thresholds, detector conditions and dead cell definitions remain.

5.2 Data and Object Selection

Collision events at a center-of-mass energy of 7 TeV recorded with the ATLAS detector during 2010 and early in 2011 are used for this study. The response of anti-k_t trigger algorithms not present during the original run is calculated in an additional reprocessing step. This does not bias the results because due to the low event rate during 2010 and early-2011 data taking the EF jet trigger was not used for rejecting events.

Baseline quality criteria that veto events affected by detector noise and read-out problems are used to pre-select events. This leads to a total number of 7.5 million events as input to this study. At least one primary vertex with four or more associated tracks with $p_T > 400\,\text{MeV}$ is required to reject events from non-collision backgrounds.

Events reconstructed at different trigger stages have to pass increasingly tight thresholds in transverse energy. The thresholds at Level 1, Level 2 and EF for several single jet triggers are summarized in Table 5.1. This means that only events with e.g. at least one Level 1 jet with E_T larger than 30 GeV are passed to the Level 2 trigger requiring 45 GeV and only events passing that threshold are passed on to the EF trigger with a requirement of 50 GeV.

Table 5.1: Inclusive single jet trigger transverse energy thresholds (in GeV) at different trigger stages. Trigger chains are built so that an event needs to pass the Level 1, Level 2 and EF thresholds succesively.

Level 1	Level 2	Event Filter
5	15	20
10	25	30
15	30	35
30	45	50
55	70	75
75	90	95

The performance — resolution and efficiency — of EF jets is measured with respect to offline jets reconstructed using the same distance parameter. Offline jets (Sec. 4.7.5) are calibrated to the EM scale and reconstructed from topoclusters with the anti-k_t algorithm . Events with jets marked as *bad* — corresponding to rare noise bursts —

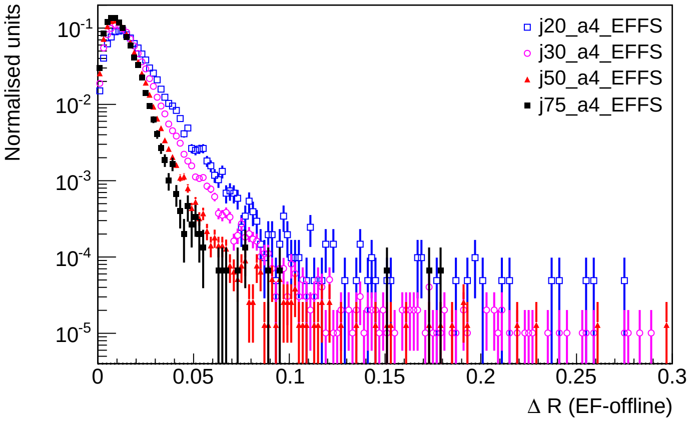

Figure 5.2: Distribution of ΔR between offline and trigger jets from anti-k_t (R=0.4) fullscan signatures with different E_{T} tresholds.

according to the quality requirements listed in Ref. [118] are rejected. To define a reference sample the following additional selection criteria are applied to offline jets:

- Not passing the *out-of-time* criteria defined in Ref. [118];
- $E_{\mathrm{T}} > 0$ and also greater than the corresponding threshold at Level 2 (see Tab. 5.1) for the EF trigger chain being analysed;
- $|\eta| < 2.8$;
- For the measurement of inclusive single jet triggers only the leading (in E_{T}) offline jet in the event is considered.

As a large number of different configurations of jet trigger chains are studied in the following, an efficient labelling system is used. A label starts with the letter “j” followed by an integer number, denoting the EF E_{T} threshold in GeV. Seperated by an underscore is the algorithm type: “a4” for anti-k_t (R=0.4), “a6” for anti-k_t (R=0.6) and “c7” for ATLAS Cone (R=0.7). An additional “tc” after the algorithm denotes that the jet is built from topoclusters, otherwise trigger towers are used. The suffix EFFS (also seperated by an underscore) denotes that the fullscan-based reconstruction is used instead of an RoI-based approach, e.g. j20_a4_EFFS corresponds to jets reconstructed using the anti-k_t (R=0.4) algorithms in the full-scan approach from trigger towers.

5.3 Metric

For defining the efficiency a matching criterion between offline jets and jets at the trigger level needs to be defined. For this study EF jets are matched to offline jets by choosing — for each offline jet — the trigger jet that matches:

$$\Delta R \equiv \sqrt{(\eta_{\mathrm{EF}} - \eta_{\mathrm{Offline}})^2 + (\phi_{\mathrm{EF}} - \phi_{\mathrm{Offline}})^2} < 0.3,$$

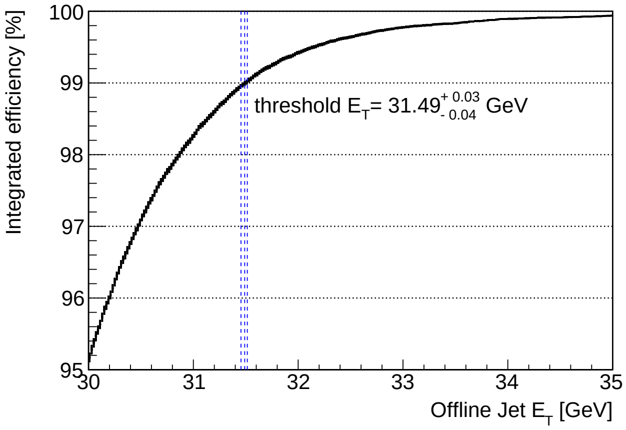

Figure 5.3: Distribution of the integrated efficiency ε_{int} for the anti-k_t (R=0.4) fullscan signature with a threshold of 30 GeV. The statistical uncertainty on the threshold value is also shown.

while minimizing

$$|E_{T,\text{Offline}} - E_{T,\text{EF}}|.$$

The second criterion reduces the events in which close by, low-energy, trigger jets are accidentally associated to offline jets. In Fig. 5.2 the distribution of ΔR for fullscan anti-k_t (R=0.4) inclusive single jet signatures with different thresholds is shown[2] . The ΔR matching improves with rising E_{T}. The distribution does not have its maximum at zero because ΔR is the quadratic sum of two radial quantities — $\Delta\eta$ and $\Delta\phi$ — with non-zero resolutions.

The efficiency ε with which offline reconstructed jets are also found at the EF stage is then defined as:

$$\varepsilon = \frac{N(\text{Offline jets matched to EF jets})}{N(\text{Offline jets})}.$$

where $N(X)$ denotes the number of jets fulfilling the indicated condition X.

A standard measure for the performance of a trigger is the offline threshold above which the overall, integrated efficiency is at least 99%. The E_{T} integrated efficiency ε_{int} is defined as:

$$\varepsilon_{\text{int}}(E_{\text{T}}) = \frac{N(\text{Offline jets with } E_{\text{T,Offline}} > E_{\text{T}} \text{ matched to EF jets})}{N(\text{Offline jets with } E_{\text{T,Offline}} > E_{\text{T}})}.$$

The integrated efficiency for the anti-k_t (R=0.4) fullscan signature with a threshold of 30 GeV is presented in Fig. 5.3. Neighbouring points on the horizontal axis are highly correlated as each point represents ε_{int} for the same reference sample with slightly different E_{T} thresholds.

The mean difference (bias, offset) and resolution in E_{T}, η and ϕ of EF jets with respect to matched offline jets are measured as functions of E_{T} and η.

---

[2] The vertical bars on all figures in Sec. 5 are used to indicate statistical uncertainties.

The root-mean-square (RMS) of the 95 % core of the distributions — RMS_{95} — is chosen as a measure of resolution because it is more robust against outliers than the pure RMS and does not require a specific shape — such as a gaussian — for the residual distributions. The 95 % core is determined iteratively until symmetric limits around the mean are found so that 95 % of the events lie within the limits.

The relative E_{T} mean shift and resolution are measured from the residual distribution of matched offline-trigger pairs of jets:

$$\Delta E_{\mathrm{T}}/E_{\mathrm{T,Offline}} \equiv \frac{E_{\mathrm{T,EF}} - E_{\mathrm{T,Offline}}}{E_{\mathrm{T,Offline}}}.$$

For the η and ϕ the residuals

$$\Delta\eta \equiv \eta_{\mathrm{EF}} - \eta_{\mathrm{Offline}}$$

and

$$\Delta\phi \equiv \phi_{\mathrm{EF}} - \phi_{\mathrm{Offline}}$$

are used respectively. In Fig. 5.4 examples of the residual distributions $\Delta E_{\mathrm{T}}/E_{\mathrm{T,Offline}}$, $\Delta\eta$, and $\Delta\phi$ are are shown. The E_{T} threshold in the offline jet selection contributes to the asymmetry in the relative E_{T} residual distribution.

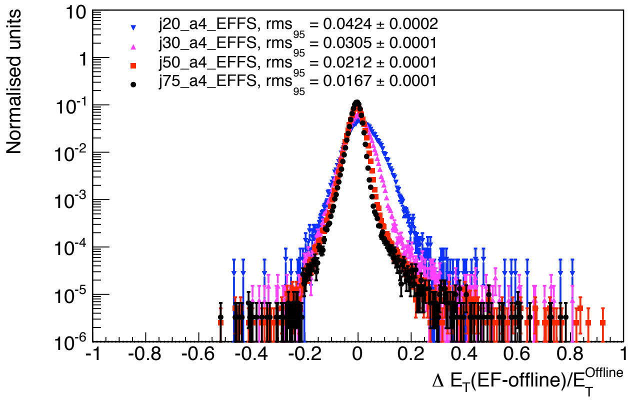

(a)

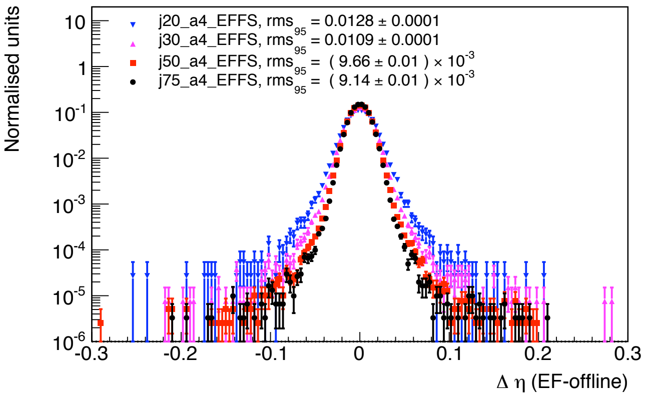

(b)

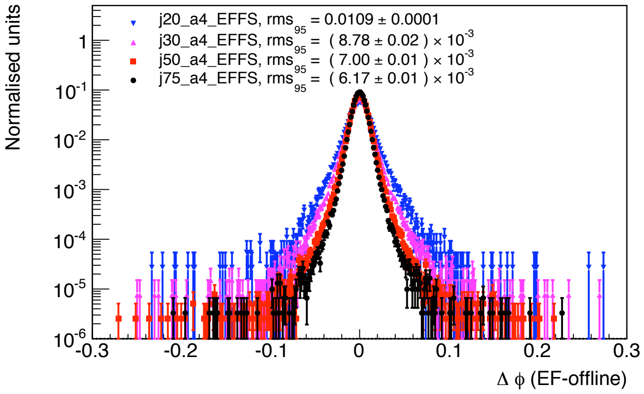

(c)

Figure 5.4: The residual distributions (a) $\Delta E_\mathrm{T}/E_{\mathrm{T,Offline}}$, (b) $\Delta\eta$, and (c) $\Delta\phi$ for four inclusive single jet chains with different thresholds using the anti-k_t (R=0.4) algorithm and the fullscan reconstruction technique.

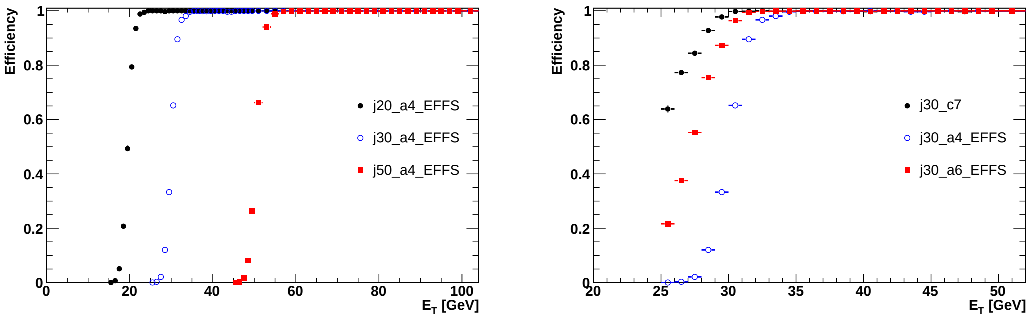

(a) (b)

Figure 5.5: Per-jet efficiency for (a) three different E_{T} thresholds using anti-k_t (R=0.4) fullscan jet reconstruction and (b) a comparison of the anti-k_t (R=0.4) fullscan, anti-k_t (R=0.6) fullscan and ATLAS Cone (R=0.7) reconstruction for a 30 GeV threshold.

5.4 Performance

5.4.1 Comparison of anti-k_t and Cone Jet Finding

The most important change in the EF jet trigger is the switch from the ATLAS Cone algorithm to the anti-k_t algorithm. In the following, anti-k_t jets reconstructed in the EF with a distance parameter of $R = 0.4$ and $R = 0.6$ are compared with anti-k_t offline jets with the same distance parameters. ATLAS Cone jets with a distance parameter $R = 0.7$ reconstructed in the EF are also compared with anti-k_t (R=0.6) offline jets as 0.6 is the largest distance parameter recommended for most analyses.

The efficiency curves for three different thresholds for the anti-k_t (R=0.4) fullscan jet reconstruction are shown in Fig. 5.5a. The efficiency increases from ≈ 0 % to a plateau at 100 % at transverse energies within a few GeV around the nominal threshold.

Comparing the efficiency between different reconstruction methods for the threshold of 30 GeV (Figure 5.5b) shows that a larger distance parameter allows more energy to be contained in the jet, shifting the turn-on to lower values. As the turn-on is also spread-out over a larger E_{T} range for larger distance parameters — largest for the ATLAS Cone jets — these are less efficient in rejecting events with low E_{T}.

In Figure 5.6 the offline E_{T} above which the integrated trigger efficiency $\varepsilon_{\mathrm{int}}$ exceeds 99 % is shown as a function of η using three different trigger configurations for the 50 GeV threshold. The variation with η is weakest when anti-k_t (R=0.4) jets are used in the trigger and strongest when ATLAS cone jets are used. There are no entries for the ATLAS Cone configuration in the central region as it is already 99 % efficient at the Level 2 threshold. This means that the ATLAS Cone trigger adds no additional rejection power in the central region.

The offset and resolution of E_{T} reconstruction in the trigger with respect to offline reconstruction techniques is presented in Fig. 5.7 as a function of E_{T} and Fig. 5.8 as a

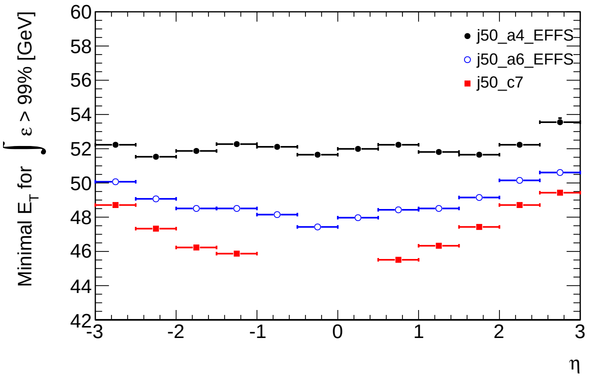

Figure 5.6: Minimal E_T so that $\varepsilon_\mathrm{int} \geq 0.99$ for anti-k_t (R=0.4), anti-k_t (R=0.6) and ATLAS Cone (R=0.7) chains using the 50 GeV threshold for different regions in η.

function of η.

Apart from an asymmetry close to the threshold the E_T reconstruction is unbiased for anti-k_t (R=0.4) jets (Fig. 5.7a). The asymmetry is only a technical artifact: jets with E_T below threshold that are mismeasured so the E_T is increased pass the threshold and are included in the sample whereas jets where the E_T fluctuates downwards fail the threshold and drop out of the sample. The resolution is below 5% at 20 GeV and improves to 2% for E_T above 100 GeV (Fig. 5.7c).

The E_T is also overestimated above the threshold (Fig. 5.7b) when a larger distance parameter is used for reconstructing the jets: the difference for the 20 GeV threshold chains at an offline E_T of 30 GeV is 10 % for anti-k_t (R=0.6) and 20 % for ATLAS Cone (R=0.7). For this E_T value the resolution (Fig. 5.7d) is 5.5 % for anti-k_t (R=0.6) and 8 % for ATLAS Cone. At higher values of E_T the bias and resolution approach zero and 2 % respectively.

In the central region ($-1 < \eta < 1$) the resolution is worsened (Fig. 5.8a and Fig. 5.8b). Jets with the same E_T have a lower total energy for central η values than at higher pseudorapidities. This means that for central jets the reconstructed E_T is subject to larger fluctuations. The observed variation of bias and resolution with η is smallest for anti-k_t (R=0.4) jets and largest for ATLAS Cone jets. The η dependence also decreases with increasing E_T.

In Fig. 5.9 the quality of ϕ reconstruction is shown. This coordinate is reconstructed without bias for all threshold and reconstruction algorithms (Fig. 5.9a and Fig. 5.9b). The ϕ resolution at low E_T is 0.01 for anti-k_t (R=0.4), 0.015 for anti-k_t (R=0.6) and 0.025 for ATLAS Cone (Fig. 5.9c and Fig. 5.9d). At high E_T the resolution approaches 0.005.

The mean shift and resolution for the reconstruction of η are presented in Fig. 5.10. For all algorithms and thresholds η is reconstructed without bias (Fig. 5.10a and Fig. 5.10b). The η resolution is 0.015 at 20 GeV for anti-k_t (R=0.4) 0.02 for anti-k_t (R=0.6) and 0.035 for ATLAS Cone reconstruction (Fig. 5.10c and Fig. 5.10d). All

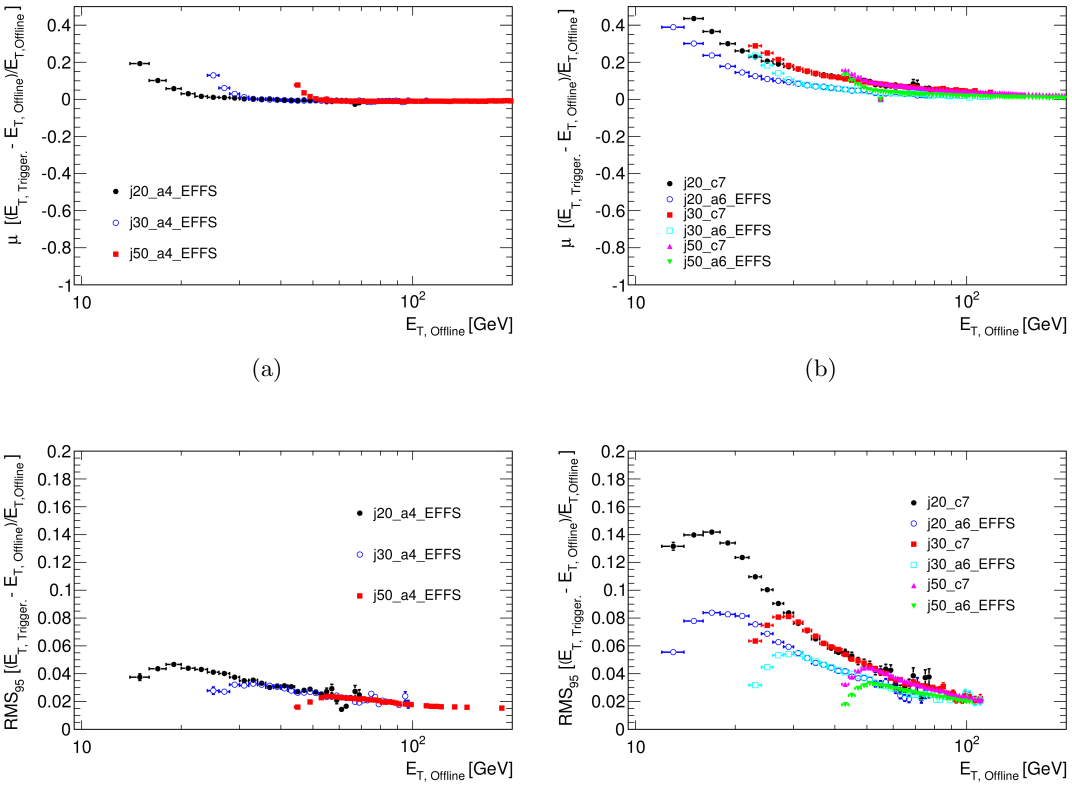

(a) (b)

(c) (d)

Figure 5.7: The relative shift of the mean in E_T between offline and trigger jets as function of E_T for three different thresholds for (a) anti-k_t (R=0.4) and (b) anti-k_t (R=0.6) and ATLAS Cone (R=0.7) jet reconstruction. The relative E_T resolution as function of E_T for (c) anti-k_t (R=0.4) and (d) anti-k_t (R=0.6) and ATLAS Cone (R=0.7) jet reconstruction.

resolutions improve to 0.01 for jets with an E_T of 100 GeV.

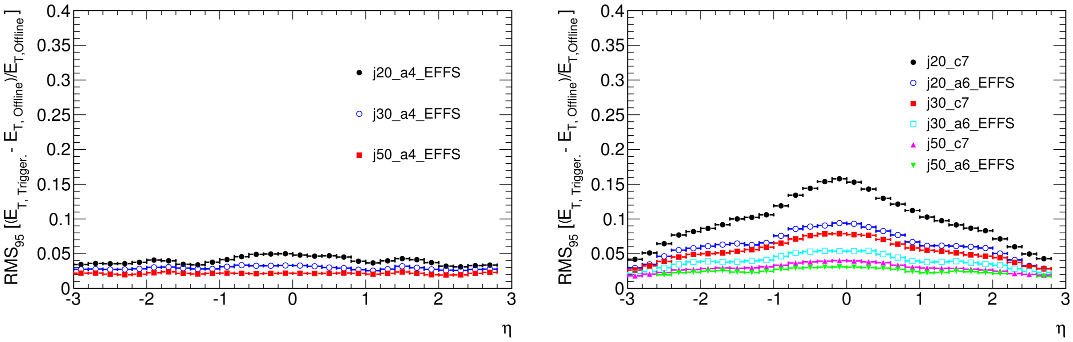

(a) (b)

Figure 5.8: Relative E_T resolution as function of η for (a) anti-k_t (R=0.4) and (b) anti-k_t (R=0.6) and ATLAS Cone (R=0.7) jet reconstruction for three different thresholds.

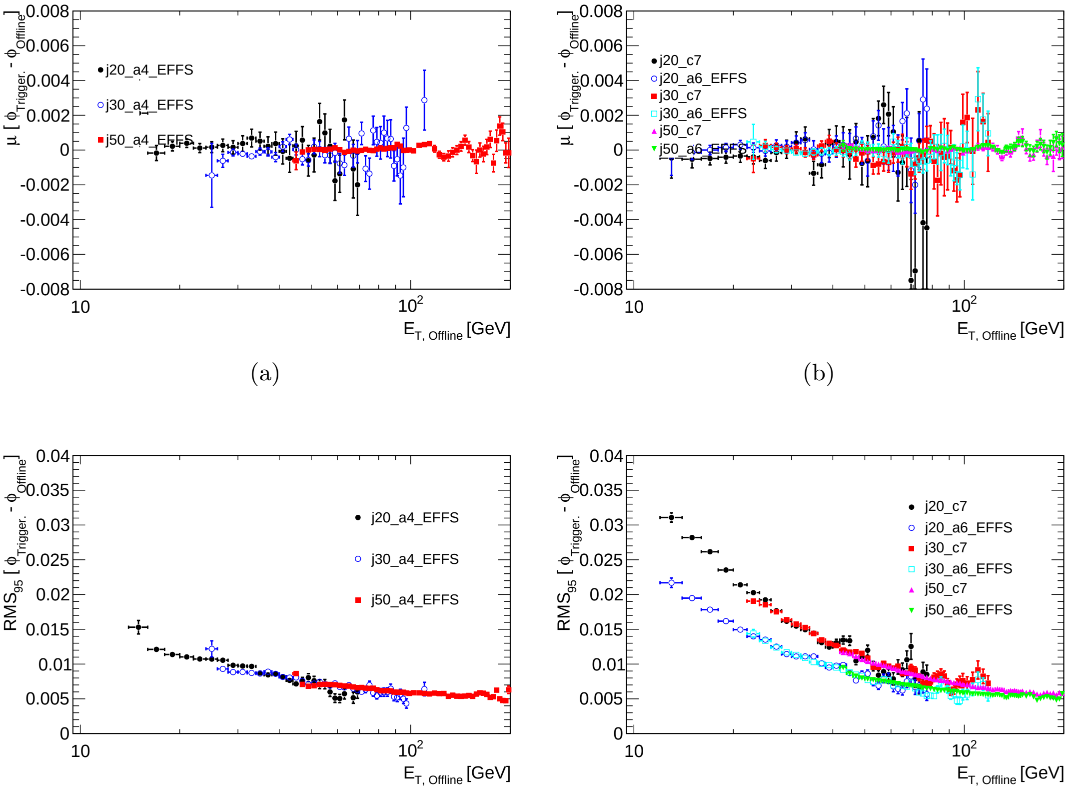

(a) (b)

(c) (d)

Figure 5.9: The shift of the mean in ϕ between offline and trigger jets as function of E_{T} for three different thresholds for (a) anti-k_t (R=0.4) and (b) anti-k_t (R=0.6) and ATLAS Cone (R=0.7) jet reconstruction. The resolution in ϕ as function of E_{T} for (c) anti-k_t (R=0.4) and (d) anti-k_t (R=0.6) and ATLAS Cone (R=0.7) jet reconstruction.

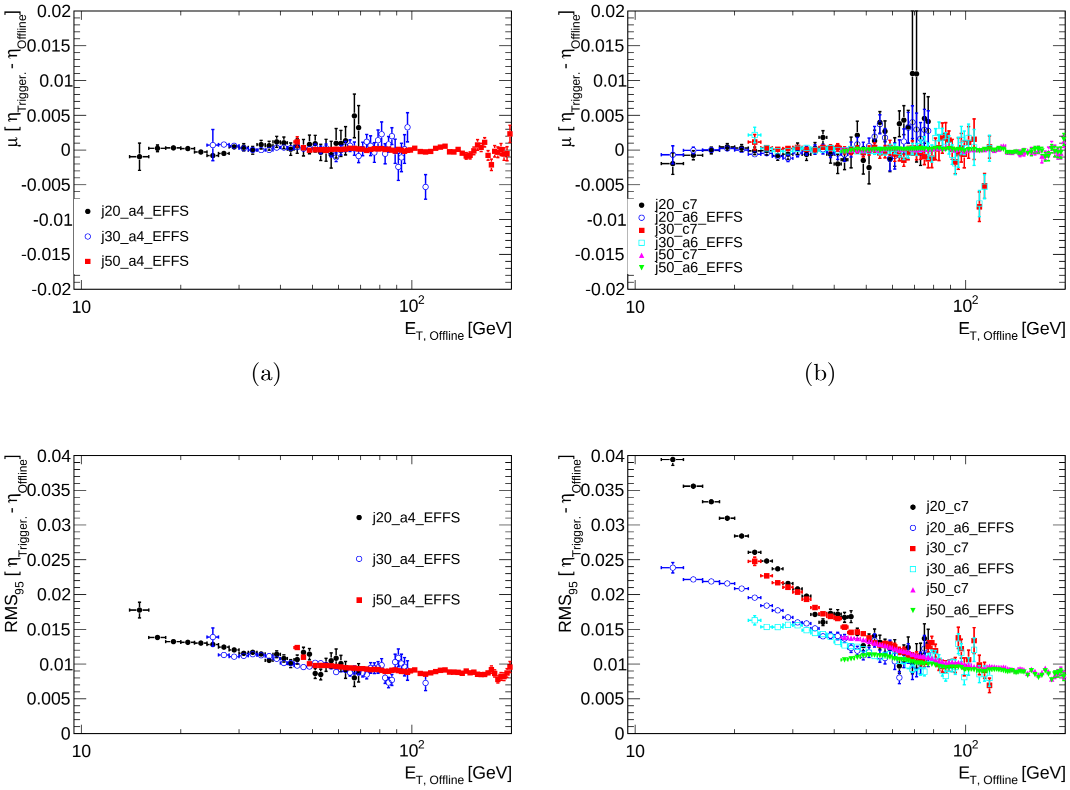

(a) (b)

(c) (d)

Figure 5.10: Shift of the mean in η between offline and trigger jet as function of E_T for three different thresholds for (a) anti-k_t (R=0.4) and (b) anti-k_t (R=0.6) and ATLAS Cone (R=0.7) jet reconstruction. Resolution in η as function of E_T for (c) anti-k_t (R=0.4) and (d) anti-k_t (R=0.6) and ATLAS Cone (R=0.7) jet reconstruction.

5.4.2 Region-of-Interest- and Fullscan-Based Jet Finding

As discussed in Sec. 5.1 the reconstruction of jets can be improved by switching from RoI-based to fullscan-based jet finding. The trigger efficiency for anti-k_t (R=0.4) chains with different thresholds using the RoI-based and fullscan-based jet finding is presented in Fig. 5.11a. For all thresholds the fullscan-based reconstruction is superior. For example the fullscan-chain with a E_T threshold of 50 GeV reaches a plateau of full efficiency at an E_T of 60 GeV whereas the RoI-based trigger is only 100 % efficient at $E_\mathrm{T} \approx 100$ GeV. This difference occurs for events that were accepted by the L2 trigger but the leading offline jet was not found at L2. If the jet in the L2 RoI does not also pass the event filter criteria, such events can be lost at the EF.

In Fig. 5.11b the angular distance ΔR between offline jets and the direction of the closest L2 RoI is shown. This is done for all offline jets, offline jets matched to a trigger jet from a fullscan EF chain and offline jets matched to a trigger jet from an RoI based chain. Most of the offline jets are closer than 0.2 in ΔR to a L2 RoI. Aditionally there are offline jets with a larger distance (around π) that are reconstructed by the fullscan approach but cannot by found by an RoI based trigger.

In Fig. 5.12 the number of EF jets that can be matched to an offline jet is shown for anti-k_t (R=0.4) jet reconstruction and with an E_T threshold of 30 GeV. For this, only isolated offline jets close to at least one L2 RoI are used. As exptected, using the fullscan approach (Fig. 5.12a), offline jets are reconstructed at most once by the trigger. Using the RoI-based approach (Fig. 5.12b) shows that a small fraction of jets is reconstructed two times. This does not affect single-jet trigger chains but can lead to false-positives for multijet-triggers.

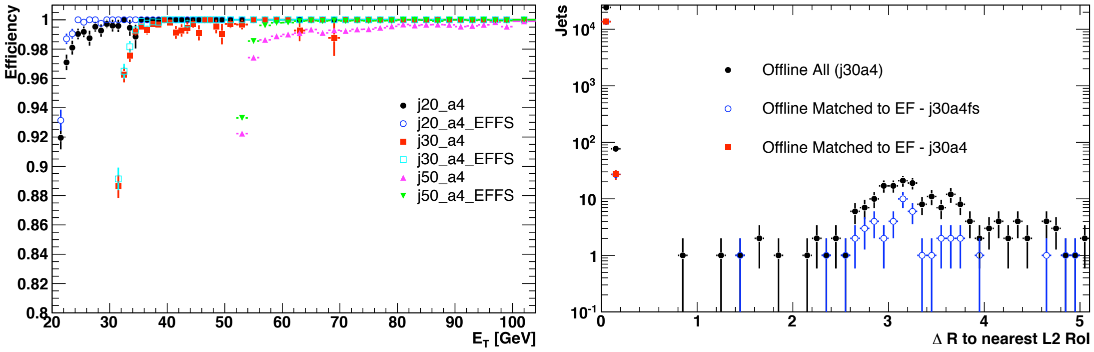

(a) (b)

Figure 5.11: The (a) per-jet efficiency using the anti-k_t (R=0.4) jet reconstruction in the RoI-based and fullscan based approach for different E_T thresholds. Distribution of (b) the distance ΔR between offline jets and the direction of the closest L2 RoI for all offline jets, offline jets matched to a trigger jet from a fullscan EF chain and offline jets matched to a trigger jet from an RoI based chain.

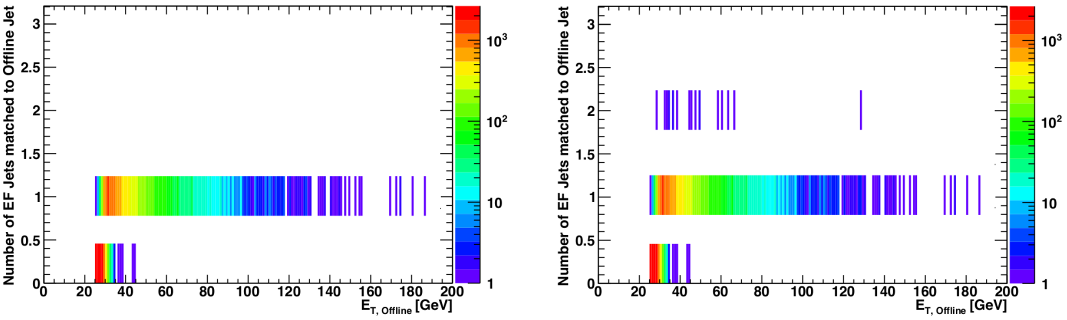

(a) j30_a4_EFFS (b) j30_a4

Figure 5.12: Multipicity of (a) fullscan-based and (b) RoI-based anti-k_t (R=0.4) EF jets reconstructed using a E_T threshold of 30 GeV that can be matched to isolated offline jets as a function of the offline jet E_T.

5.4.3 Data and Simulation

To ensure a good description of the fullscan reconstruction technique using the anti-k_t algorithm by MC simulation the measured bias and resolution are compared with events recorded during the 2010 data-taking period. The comparison is made with respect to a QCD multijet sample, simulated using the Pythia 6 [103] MC generator.

In Figure 5.13 data and MC simulation agree overall, especially for the bias in E_T reconstruction as function of E_T (Fig. 5.13a). At lower E_T the resolution is well modelled with a shift of 0.8 % for E_T larger than 35 GeV (Fig. 5.13b). The variation of the mean E_T shift with η is slighty underestimated by the simulation (Fig. 5.13c). The difference is less visible when the resolution is shown as a function of η. This is caused by the larger fraction of lower-E_T jets in the sample (Fig. 5.13d). There is no bias in the reconstruction of η (Fig. 5.13e) and the resolution is 0.011 for E_T of 30 GeV in data and 0.010 in the simulation (Fig. 5.13f).

5.4.4 Fullscan Based anti-k_t Jet Finding in Data in 2010 and 2011

To verify that results from studies using reprocessed data from 2010 collisions are also valid for 2011 where the new trigger chains are executed online, a comparison of efficiency and resolutions for anti-k_t fullscan jet reconstruction is made. The measured efficiency is shown in Fig. 5.14 and the mean shifts and resolutions are presented in Fig. 5.15.

The efficiency distributions as a function of E_T agree well between data recorded in 2010 and 2011 (Fig. 5.14). The efficiency recorded in 2011 rises slightly less steeply at the threshold and is shifted towards higher E_T values. This can be attributed to additional fluctuations and higher contributions from pile-up.

The mean E_T bias (Figure 5.15a) above the threshold is negligible for jets measured in 2010 and 2011. The E_T resolution for low E_T jets (Figure 5.15b) is $\approx 5\,\%$ and shows a small increase in 2011.

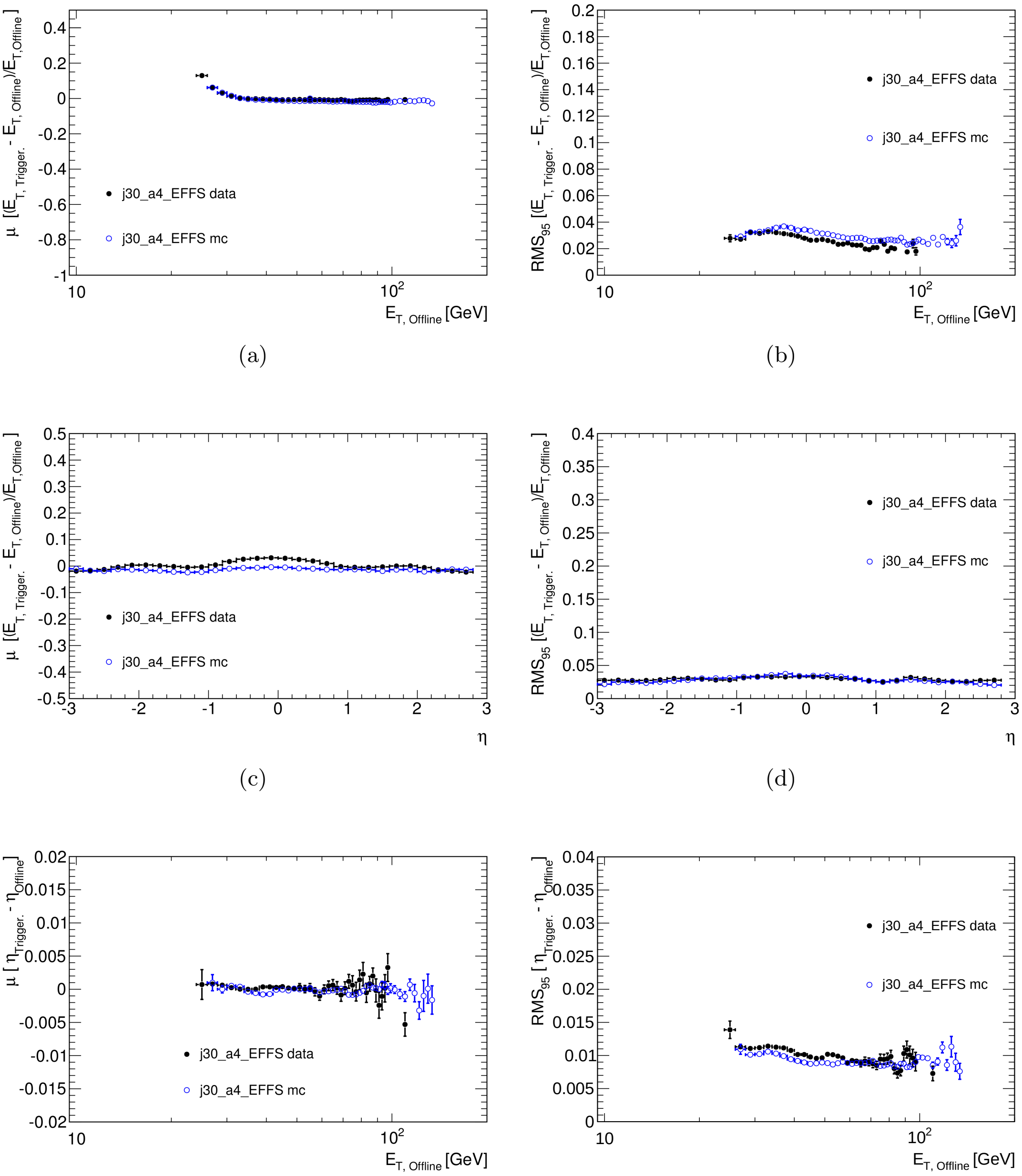

(a) (b)

(c) (d)

(e) (f)

Figure 5.13: A comparison between data recoreded in 2010 with MC simulation for the fullscan reconstructed anti-k_t (R=0.4) jet reconstruction for the 30 GeV threshold. Presented are: (a) the bias in E_T as a function of E_T, (b) the E_T resolution as a function of E_T, (c) the bias in E_T as a function of η, (d) the E_T resolution as a function of η, (e) the bias in η as a function of E_T and (f) the η resolution as a function of E_T.

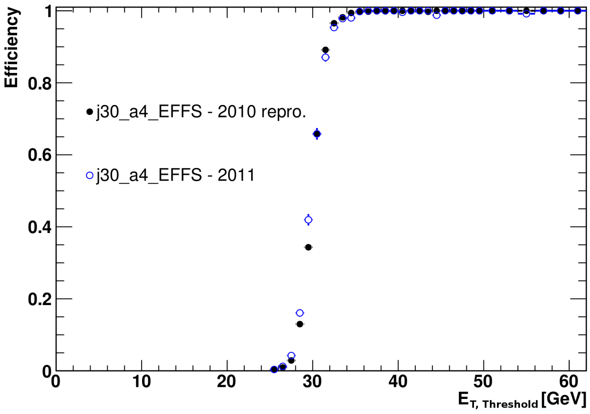

Figure 5.14: Per-jet efficiency using anti-k_t (R=0.4) fullscan jet reconstruction with a 30 GeV threshold. Shown is a comparison of data recorded during 2010 and from a run in early 2011.

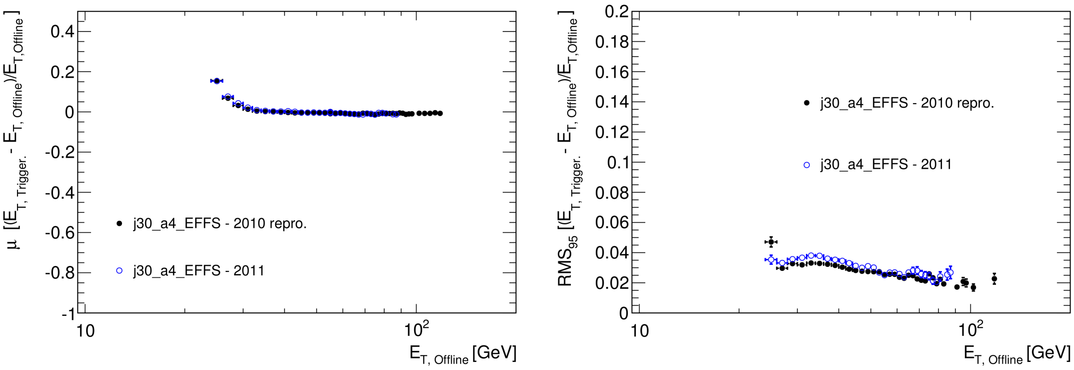

(a) (b)

Figure 5.15: Distribution of (a) the bias and (b) the resolution in E_T between offline and trigger jets as function of E_T for anti-k_t (R=0.4) jet reconstruction. Shown is a comparison of data recorded during 2010 and from a run in early 2011.

5.4.5 Calorimeter Trigger Towers and Topological Clusters

Another step to reduce differences between jet reconstruction in the trigger and the jets used in offline analyses is to use the same input objects. This means replacing the trigger towers with topological clusters of calorimeter cells.

A comparison of the trigger efficiency between these two approaches is presented for two different E_{T} threshold in Fig. 5.16. Using topoclusters leads to a sharper turn-on (corresponding to an improved E_{T} resolution) at slightly higher values of E_{T}.

The E_{T} shift (Fig. 5.17a) below the threshold is slightly smaller for jets built from topoclusters, above the thresholds both distributions approach zero. The E_{T} resolution (Fig. 5.17b) improves from 4 % to 2 % for 30 GeV jets when using topoclusters. The η resolution (Fig. 5.17c) and ϕ resolution (Fig. 5.17d) at a jet E_{T} of 30 GeV are reduced from ≈ 0.015 to ≈ 0.07 by using topoclusters.

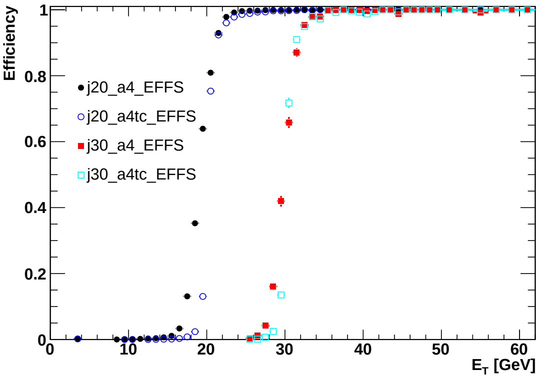

Figure 5.16: Per-jet efficiency using the anti-k_t (R=0.4) fullscan reconstruction for different E_{T} thresholds. Jets constructed from trigger towers and topoclusters are compared.

5.5 Conclusions

The reasons for the three changes to prepare the EF jet trigger for data taking in 2011 and beyond are described in Sec. 5.1. Using the anti-k_t algorithm in a fullscan approach with topoclusters as input for reconstruction reduces the differences with respect to offline techniques. While only the effects on inclusive single jet trigger chains are studied the results also apply to more complex trigger signatures — as for example multijet signatures —as these quantities are calculated as sums of individual jets.

In Sec. 5.4 the effect of these changes on the trigger efficiency and the resulting change in bias and resolution are reviewed. Events simulated using MC techniques are used to make sure that the results obtained on data correspond to the modelling of the ATLAS detector. A comparison of data recorded in 2010 with collision events recorded in 2011 was performed to ensure a smooth start of operations.

In an additional study [117], the time consumption of the jet trigger was evaluated.

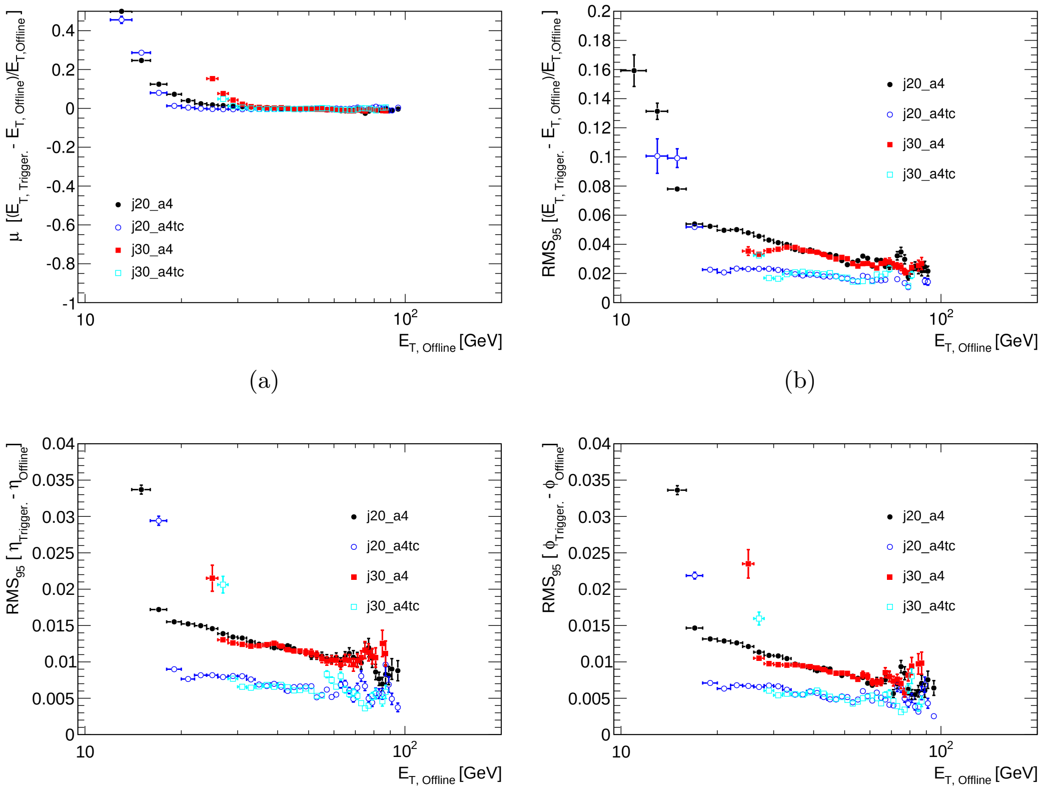

(a) (b)

(c) (d)

Figure 5.17: Distribution of (a) the shift of the mean (b) the resolution in E_T between offline and trigger jets as function of E_T for two different thresholds and two different collections of input objects to the jet finding: trigger towers and topoclusters. The resolution in (c) η and (d) ϕ between offline and trigger jets as function of E_T.

The mean execution time (including the time needed for data-preparation) is ≈ 200 ms for the first reconstruction of all jets in the event. The subsequent tests if the reconstructed jets fulfill the multiplicity and E_T requirements then only take a few ms. As the average total time available per-event at the EF is approximately 4 s, the typical execution times of the jet trigger do not pose a problem.

All results show that the updated EF jet trigger can be safely used to select events for physics analyses from 2011 onwards.

Chapter 6

Performance of the HEPTopTagger

Before the HEPTopTagger algorithm, described in Sec. 2.5, can be used in the search for new phenomena beyond the Standard Model, its performance needs to be validated using samples statistically independent from the samples used for the search. As the fully hadronic final state is used for the resonance search, a sample containing $t\bar{t}$ decays with one muon in the final state is utilized for these validation studies. Requiring the presence of isolated muons reduces the multijet background so that a clean top-quark signal can be observed. Sec. 6.1 lists the applied selection criteria. MC simulation based studies of resolution and efficiency are summarized in Sec. 6.2 and a comparison between data and MC simulation is presented in 6.3. These studies are also documented in Ref. [119].

6.1 Event Selection

The data and Monte Carlo simulated samples used in this analysis are described in Sec. 4.8. All events are required to pass the EF muon trigger, with a p_{T}[1] threshold of 18 GeV. Events are selected if they contain at least four jets, reconstructed with the anti-k_t algorithm and a distance parameter $R = 0.4$. These jets are required to have $p_{\mathrm{T}} > 25$ GeV and a jet-vertex fraction $|JVF| > 0.75$. The JVF is the fraction of the energy of tracks around the jet that can be matched to the primary vertex, divided by the total energy of tracks inside the jet. Finally, jets need to fulfill the quality requirements — i.e. the *loose* criterion — defined in Ref. [120]. Requiring four or more anti-k_t jets is not ideal for analyzing very boosted top quarks, but this selection was kept for consistency with other studies in ATLAS.

In the offline event selection exactly one muon is required. This muon must have tracks in the inner detector and muon system, a $p_{\mathrm{T}} > 20\,\mathrm{GeV}$ and $|\eta| < 2.5$. Muons within a cone of $\Delta R < 0.4$ to a jet are discarded. If there are electrons passing default DQ-requirements in the event, the event is discarded.

As input to the HEPTopTagger, fat jets reconstructed with the Cambridge-Aachen algorithm (R=1.5) with $p_{\mathrm{T}} > 200$ GeV are required. These are built from the same

---

[1] The coordinate system is defined in Sec. 4.1.

input objects (topoclusters, Sec. 4.7.5) as the $R = 0.4$ anti-k_t jets. As the multiplicity of anti-k_t jets is only used for the initial event selection, the inevitable overlap of jets from the two collections is not problematic.

To suppress events without a neutrino or a leptonically decaying W boson, selection criteria on the missing transverse energy $E_{\mathrm{T}}^{\mathrm{miss}}$ and the transverse mass of the W boson (m_T) are applied. m_T is defined as the mass of the vector sum of the transverse components of the $E_{\mathrm{T}}^{\mathrm{miss}}$ and muon four-vectors. The requirements are $E_{\mathrm{T}}^{\mathrm{miss}} > 20$ GeV and $E_{\mathrm{T}}^{\mathrm{miss}} + m_T > 60$ GeV.

The dominant background to $t\bar{t}$ decays with one muon in the final state is formed by events with a W boson and associated jets. If the W boson decays into a muon and a neutrino these events can pass the selection criteria. Single top events can also be selected if the W boson from the top-quark decay subsequently decays into a muon and a neutrino. These events are however surpressed by the lower cross-section with respect to the $t\bar{t}$ process as well as a lower number of jets per event. Events where a Z boson instead of a W boson is produced in association with jets are surpressed by requiring missing energy and exactly one muon. The contributions from diboson (WW, WZ and ZZ) and QCD multijet production are negligible.

6.2 Performance on Simulated Events

The $t\bar{t}$ MC simulated sample is used to study the resolution and signal efficiency of the HEPTopTagger. For this, events are selected if they contain at least one hadronically decaying top quark, with a truth level (reconstructed from simulated, stable particles) $p_{\mathrm{T}} > 150$ GeV.

6.2.1 Bias and Resolutions

In Fig. 6.1 the distribution of mass, p_{T}, η and ϕ for generated, truth-level, top quarks as well as top-quark candidates reconstructed by the HEPTopTagger algorithm are presented for the $t\bar{t}$ MC sample. The reconstructed mass (Fig. 6.1a) is shifted to lower values and peaks less sharply than the generated mass. The minimal p_{T} for top-quark candidates is 200 GeV (Fig. 6.1b) whereas top quarks are produced with a minimal p_{T} of 150 GeV. The distribution of η (Fig. 6.1a) is slightly more central for reconstructed than for generated top quarks while there is no difference in the distributions for the ϕ direction (Fig. 6.1d).

In Fig. 6.2 the difference in mass, p_{T}, η and ϕ between the generated top quark and the reconstructed top-quark candidate is shown. On average the mass is underestimated by 8 GeV to 13 GeV with a resolution (defined as the RMS of the distribution) of ≈ 15 GeV. For low-p_{T} top quarks the HEPTopTagger algorithm overestimates the p_{T} on average by 6 % whereas for high-p_{T} quarks the p_{T} is underestimated by up to 9 %. The p_{T} resolution improves from 20 % at low p_{T} to 10 % at high p_{T}. The angular variables η and ϕ are reconstructed without bias and a resolution between 0.22 and 0.08, depending on the top-quark p_{T}.

To quantify the effect of pile-up on offsets and resolutions of mass, p_{T}, η and ϕ, the mean and RMS of these distributions are drawn as a function of the average number of

Table 6.1: Overview of the HEPTopTagger performance. Offset and slope are the result of a linear fit to $\langle\mu\rangle$. Entries of "< 0.001" indicate that the absolute value of the slope is smaller than 0.001.

	Mean		RMS	
$p_{\mathrm{T,\,Gen.}}$ [GeV]	offset	slope	offset	slope
$\eta_{\mathrm{Gen.}} - \eta_{\mathrm{Cand.}}$				
150 – 240	0.003 ± 0.006	-0.000 ± 0.001	0.223 ± 0.004	< 0.001
240 – 300	0.000 ± 0.003	< 0.001	0.117 ± 0.002	0.001 ± 0.000
300 – 900	0.000 ± 0.002	< 0.001	0.124 ± 0.002	-0.001 ± 0.000
$\phi_{\mathrm{Gen.}} - \phi_{\mathrm{Cand.}}$				
150 – 240	0.004 ± 0.005	< 0.001	0.180 ± 0.003	< 0.001
240 – 300	0.002 ± 0.002	< 0.001	0.093 ± 0.001	0.001 ± 0.000
300 – 900	0.003 ± 0.002	< 0.001	0.082 ± 0.001	< 0.001
$m_{\mathrm{Gen.}} - m_{\mathrm{Cand.}}$ [GeV]				
150 – 240	8.26 ± 0.38	0.00 ± 0.04	14.72 ± 0.27	0.03 ± 0.03
240 – 300	12.49 ± 0.30	-0.08 ± 0.03	13.96 ± 0.21	0.03 ± 0.02
300 – 900	13.14 ± 0.34	-0.08 ± 0.03	16.15 ± 0.24	0.03 ± 0.02
$(p_{T,\mathrm{Gen.}} - p_{T,\mathrm{Cand.}})/p_{T,\mathrm{Gen.}}$				
150 – 240	-0.067 ± 0.006	-0.002 ± 0.001	0.204 ± 0.004	0.001 ± 0.000
240 – 300	0.064 ± 0.002	-0.001 ± 0.000	0.093 ± 0.001	< 0.001
300 – 900	0.094 ± 0.002	< 0.001	0.104 ± 0.002	< 0.001

interactions per bunch crossing $\langle\mu\rangle$ (Sec. 3.2). In Fig. 6.3 the resulting distributions for mass and p_{T} are shown as examples. The points are overlayed with a fit of the form

$$Y = \mathit{offset} + \mathit{slope} \cdot \langle\mu\rangle$$

where *offset* and *slope* are the fitted parameters and Y stands for either the mean or RMS of the mass, p_{T}, η or ϕ distributions.

The results of these fits are summarized in Table 6.1. The mean shift and resolution of η and ϕ are unaffected by the amount of pile-up present. The mean mass is also stable with pile-up: the maximal slope is 0.08 GeV. As shown in Fig. 3.6, the mean number of interactions per bunch crossing ($\langle\mu\rangle$) for the 2011 data taking run for most events is $5 < \langle\mu\rangle < 15$. The total change in mass-bias due to pile-up (10×0.08 GeV) is therefore small in comparison to the offset. The slope of 0.03 GeV for the RMS is similarly negligible. The largest change in the mean p_{T} shift is 0.2 % for low-p_{T} top-quark candidates while the RMS is robust.

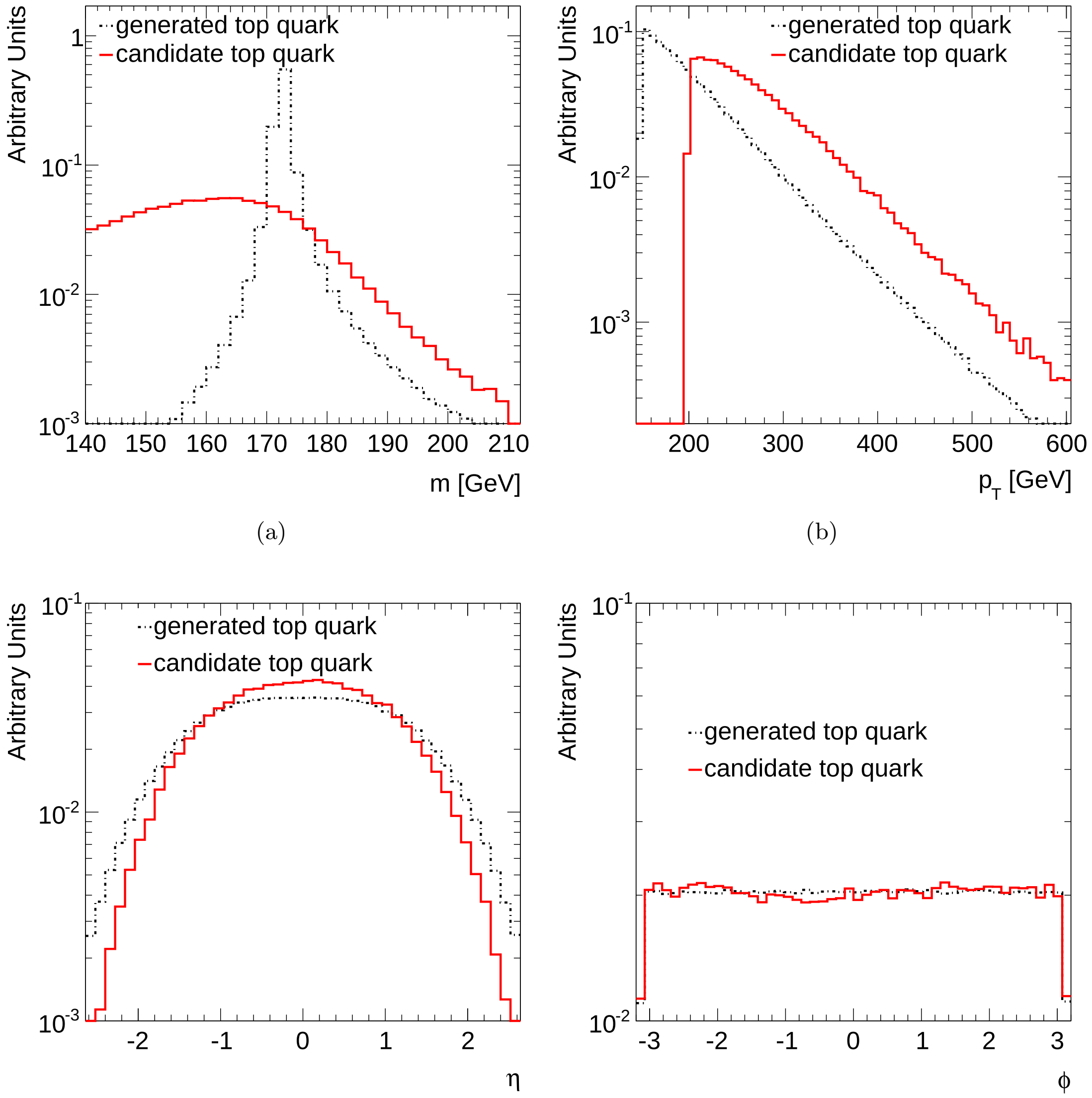

(a) (b)

(c) (d)

Figure 6.1: Distribution of (a) the mass, (b) p_{T}, (c) η and (d) ϕ for generated, hadronically decaying top quarks and top-quark candidates reconstructed using the HEPTopTagger algorithm. The $t\bar{t}$ MC sample is used. All distributions are weighted so that the area under the histograms equals one. No selection is performed on the pile-up distribution $\langle\mu\rangle$.

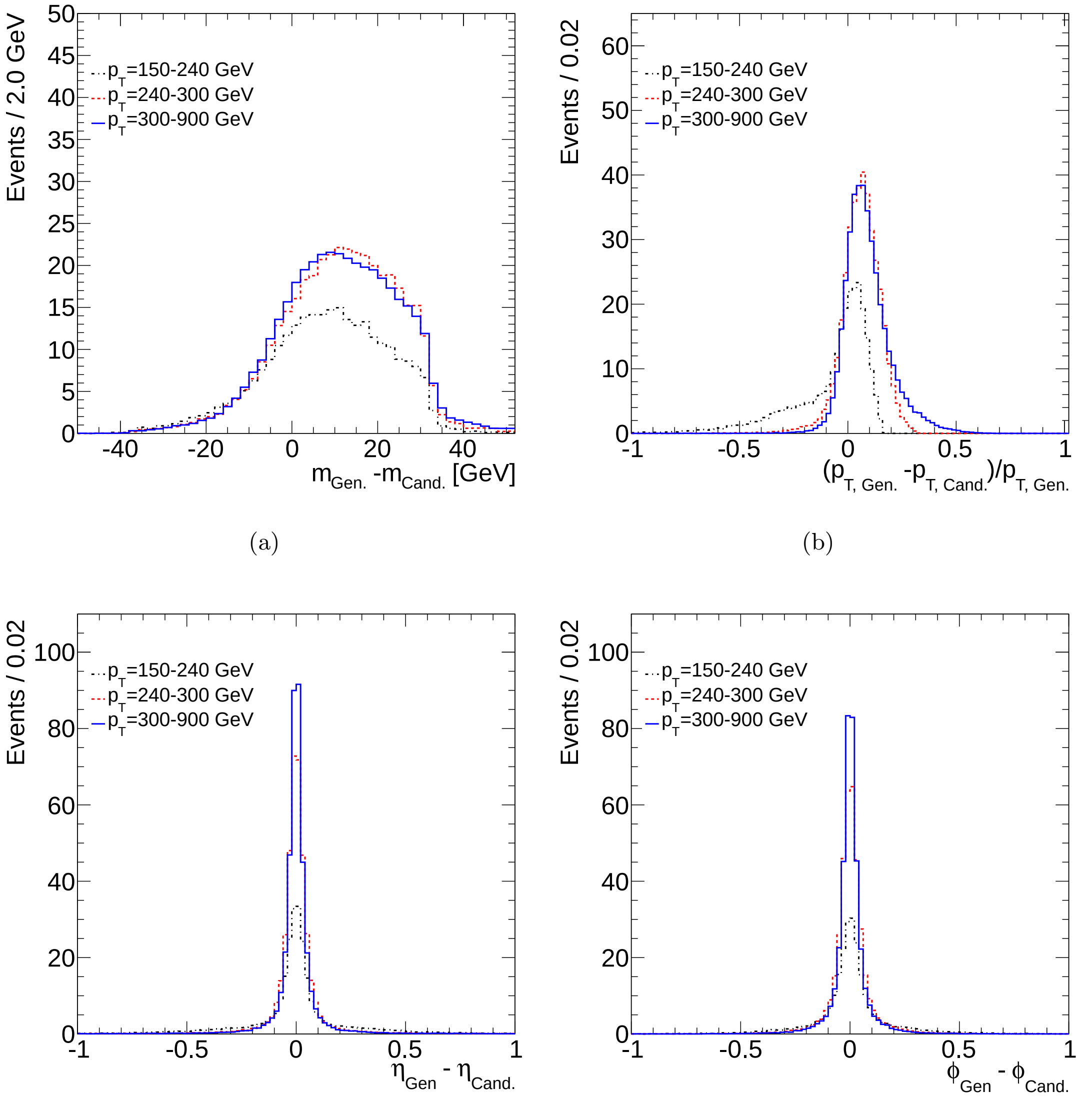

(a) (b)

(c) (d)

Figure 6.2: Residual toq-quark candidate (a) mass, (b) p_{T}, (c) η and (d) ϕ distribution for three different regions of generated top-quark p_{T}. Shown are the difference between the generated (true) value and the reconstructed value after full detector simulation and application of the HEPTopTagger. The $t\bar{t}$ MC sample is used and events are normalized to an integrated luminosity of $1\,\mathrm{fb}^{-1}$. No selection is performed on the pile-up distribution $\langle\mu\rangle$.

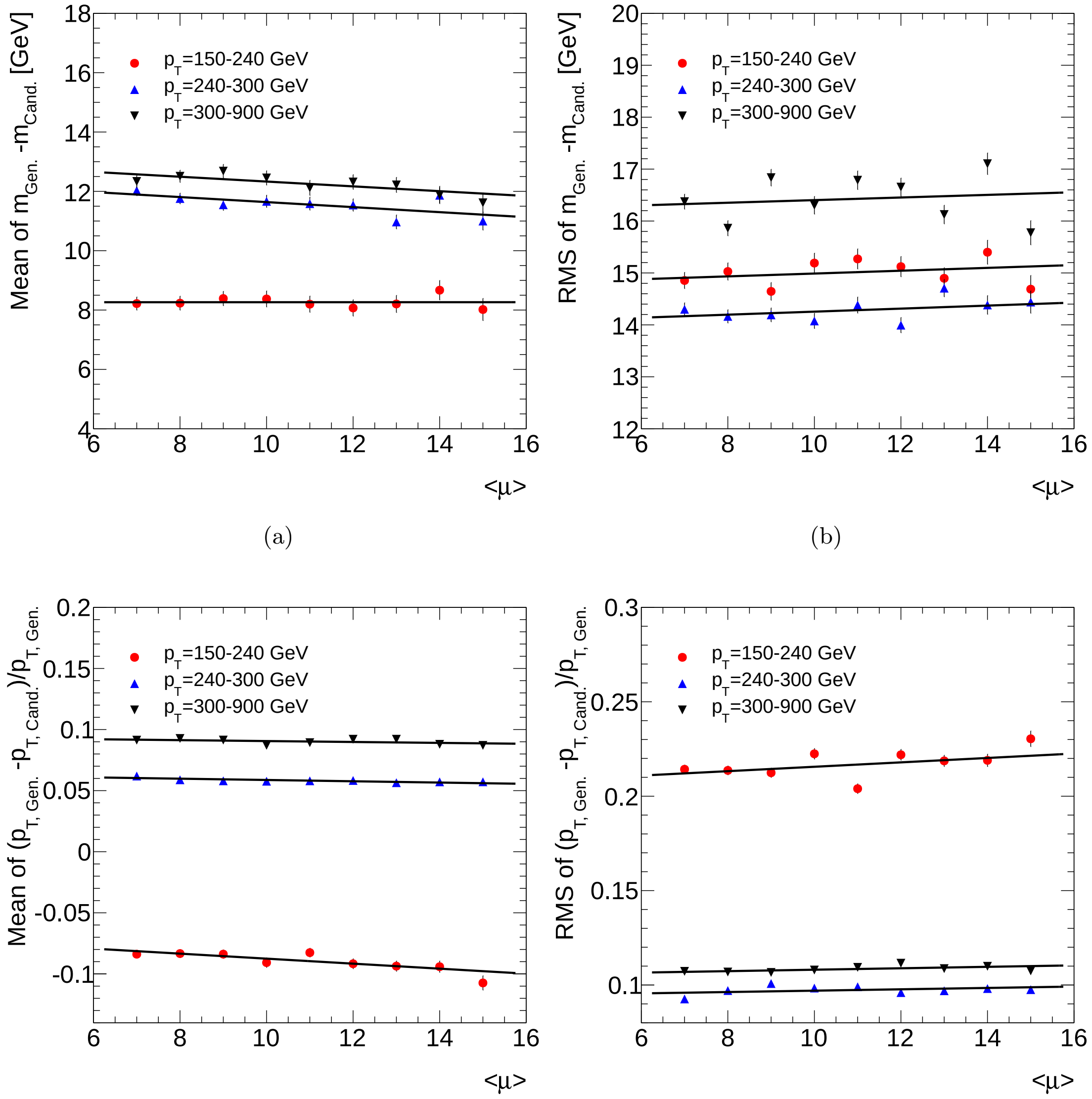

(a) (b)

(c) (d)

Figure 6.3: Distribution of the (left) mean and (right) RMS of the (top) mass and (bottom) p_{T} residual distributions from Fig. 6.2 as a function of the average number of interactions per bunch-crossing $\langle \mu \rangle$ for three different regions of generated top-quark p_{T} using the $t\bar{t}$ MC sample. Linear fits to the distributions are superimposed. The vertical bars represent the statistical uncertainty.

6.2.2 Efficiencies

The efficiency to find a top-quark candidate using the HEPTopTagger algorithm $\varepsilon(\text{total})$ is the product of the efficiency to find a fat jet ($\varepsilon(\text{fat jet})$ and the efficiency to correctly tag that jet ($\varepsilon(\text{tag})$):

$$\varepsilon(\text{total}) = \varepsilon(\text{fat jet}) \cdot \varepsilon(\text{tag}).$$

The efficiencies are defined as:

$$\varepsilon(\text{total}) = \frac{N(\text{matched and tagged})}{N(\text{generated})},$$

$$\varepsilon(\text{fat jet}) = \frac{N(\text{matched})}{N(\text{generated})},$$

and

$$\varepsilon(\text{tag}) = \frac{N(\text{matched and tagged})}{N(\text{matched})},$$

where $N(\text{generated})$ is the number of generated top quarks, $N(\text{matched})$ is the number of generated top quarks matched to a fat jet and $N(\text{matched and tagged})$ is the number of generated top quarks matched to a fat jet which is also tagged by the HEPTopTagger. Generated, hadronically decaying, top quarks are matched to fat jets with $p_{\mathrm{T}} > 200$ GeV within a cone of $\Delta R = 1.0$. If multiple fat jets are found within the cone, the one minimizing ΔR to the generated top is selected.

The efficiencies are presented in Fig. 6.4. The fat jet finding efficiency $\varepsilon(\text{fat jet})$ (Fig. 6.4a) shows a sharp turn-on starting at $p_{\mathrm{T}} \approx 180$ GeV and an efficiency of 100 % is reached at $p_{\mathrm{T}} \approx 300$ GeV. The fat-jet-finding efficiency depends on the pile-up conditions (Fig. 6.4b). Higher pile-up increases $\varepsilon(\text{fat jet})$. In Fig. 6.4c it can be seen that $\varepsilon(\text{total})$ starts to increase at $p_{\mathrm{T}} \approx 200$ GeV and reaches a plateau of 40 % at $p_{\mathrm{T}} \approx 400$ GeV. The efficiency is dominated by top-quark candidates not passing the kinematic selection requirements. The total efficiency is robust against changes in pile-up (Fig. 6.4d).

For background processes not containing real top-quark decays, the fraction of tagged fat jets is presented as function of the fat jet p_{T} in Fig. 6.5. The distribution is similar for hadronic decays of W bosons and QCD multijet events. It is 0.5 % at $p_{\mathrm{T}} \approx 300$ GeV and reaches 2.5 % at $p_{\mathrm{T}} \approx 500$ GeV.

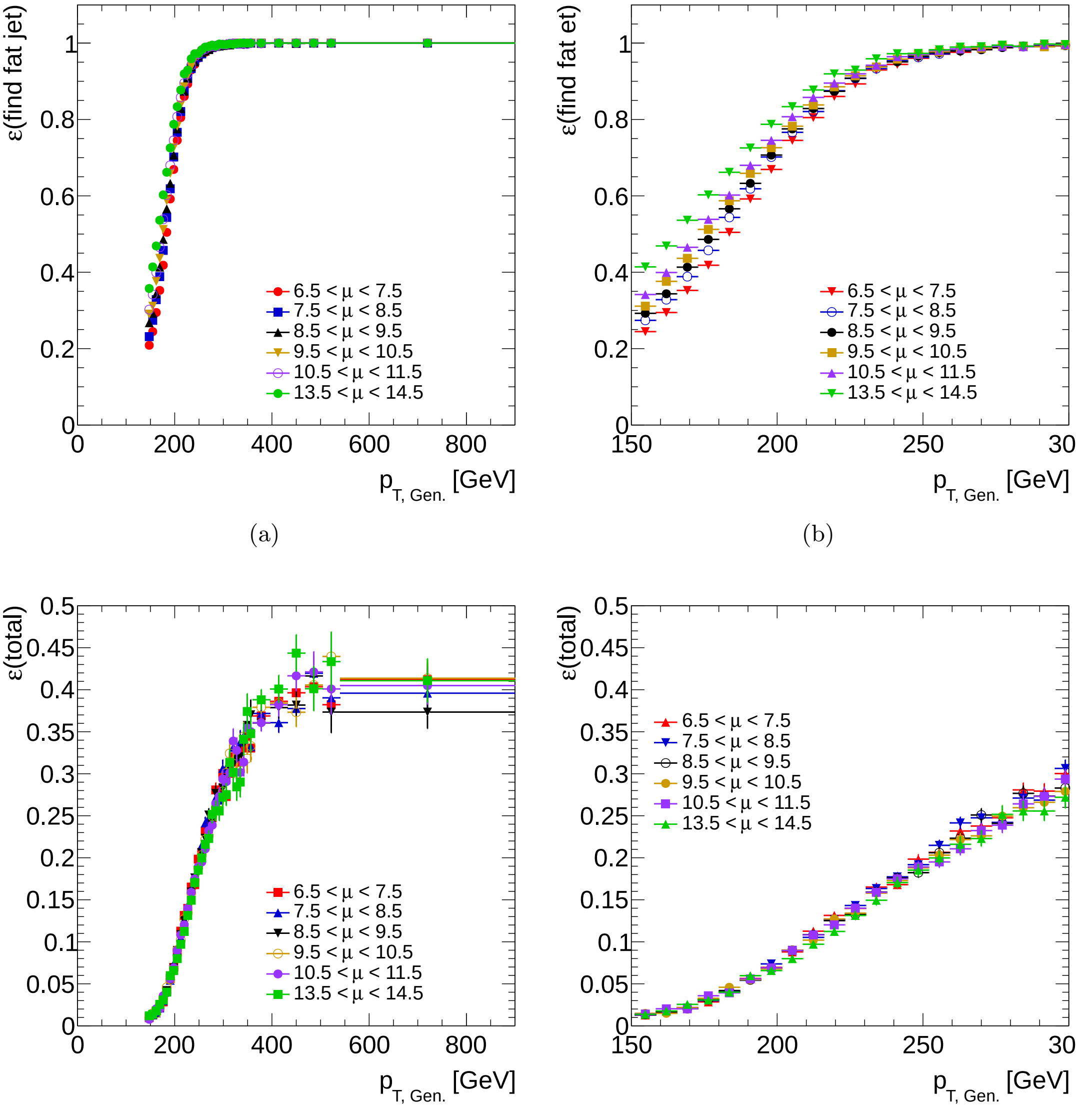

(a) (b) (c) (d)

Figure 6.4: Distribution of the efficiency to find a fat jet with $p_{\mathrm{T}} > 200$ GeV for (a) $0 < p_{T,\mathrm{Gen.}} < 900$ GeV and (b) $150 < p_{T,\mathrm{Gen.}} < 300$ GeV as well as the efficiency to successfully reconstruct the top quark using the HEPTopTagger algorithm for (c) $0 < p_{T,\mathrm{Gen.}} < 900$ GeV and (d) $150 < p_{T,\mathrm{Gen.}} < 300$ GeV. The efficiencies are plotted as a function of the generated top-quark p_{T} and shown for different pile-up ranges. Events from the $t\bar{t}$ MC sample are used for all distributions. The vertical bars represent the statistical uncertainty.

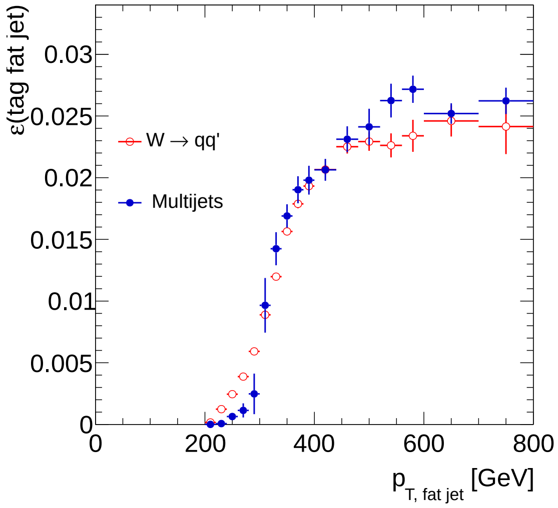

Figure 6.5: Fraction of fat jets that are (wrongly) identified as a top-quark candidate using the HEPTopTagger algorithm as function of the fat jet p_{T}. The distribution is shown for two different background samples: QCD multijet events and events containing a hadronically decaying W boson. The vertical bars represent the statistical uncertainty.

6.3 Comparison of Data and Simulation

For a comparison between data and the MC prediction the full selection described in Sec. 6.1 is applied. In Fig. 6.6 three basic quantities used in the event selection are shown: the p_{T} of the leading (in p_{T}) anti-k_t jet (R=0.4) in Fig. 6.6a, the p_{T} of the leading muon in Fig. 6.6b and the missing transverse energy in Fig. 6.6c. In these (and the following) figures the data recorded in 2011 are overlayed with the stacked contributions to the SM prediction. The largest contributions are due to $t\bar{t}$ and the associated production of W bosons (which subsequently decay into a charged lepton and a neutrino) and jets. The single top-quark production and the production of a Z boson in association with jets are less important processes. All distributions show good agreement between data and MC prediction.

In Fig. 6.7, the distributions for fat jets before application of the HEPTopTagger algorithm are shown. The mass of fat jets (Fig. 6.7a) is between 100 GeV and 400 GeV for a large fraction of events. The p_{T} distribution (Fig. 6.7b) is steeply falling from 2000 events per 8 GeV at 200 GeV to a few events at $\approx$ 800 GeV. Most fat jets are central in η and the distribution extends to approximately $|\eta| < 2.5$, as can be seen in Fig. 6.7c. The distribution is flat in ϕ (Fig. 6.7d). All fat jet kinematic quantities before application of the HEPTopTagger are well modelled in the simulation.

The mass and p_{T} of fat jets and top candidates after applying the HEPTopTagger are presented in Figs. 6.8. The fraction of $t\bar{t}$ events is increased in comparison with Fig. 6.7. Comparing the fat jet mass distribution in Fig. 6.8b with the filtered mass of the top candidate in Fig. 6.8d shows an improved mass reconstruction for top quarks with a sharp peak around the top-quark mass of $\approx 172\,\mathrm{GeV}$ [15]. The second, background-dominated, peak below 50 GeV is due to the large number of possible combinations of low p_{T} subjets and can be removed by increasing the lower mass limit in the initial unclustering step of the HEPTopTagger algorithm from 30 GeV to 50 GeV [67]. The kinematics of top-quark candidates reconstructed using the HEPTopTagger are well described by the simulation.

The shape of two substructure variables used for identifying top quark candidates is shown in Fig. 6.9. The HEPTopTagger algorithm identifies exactly three subjets in the final step. There are three possible combination to match these subjets to the b quark and the two decay products from the W boson. The left peak in Fig. 6.9a corresponds to the leading and sub-sub-leading subjet coming from the W boson, the right peak to the leading and sub-leading subjets. The peak around $\frac{m_W}{m_t}$ (≈ 0.46) in Fig. 6.9c occurs for decays where the sub-leading and sub-sub-leading subjets form the W.

In Fig. 6.10 the distribution of the mean reconstructed top-quark candidate mass is shown as a function of the average number of interactions per bunch-crossing for data and simulated events. The mean reconstructed mass shows no systematic shift with increased $\langle\mu\rangle$.

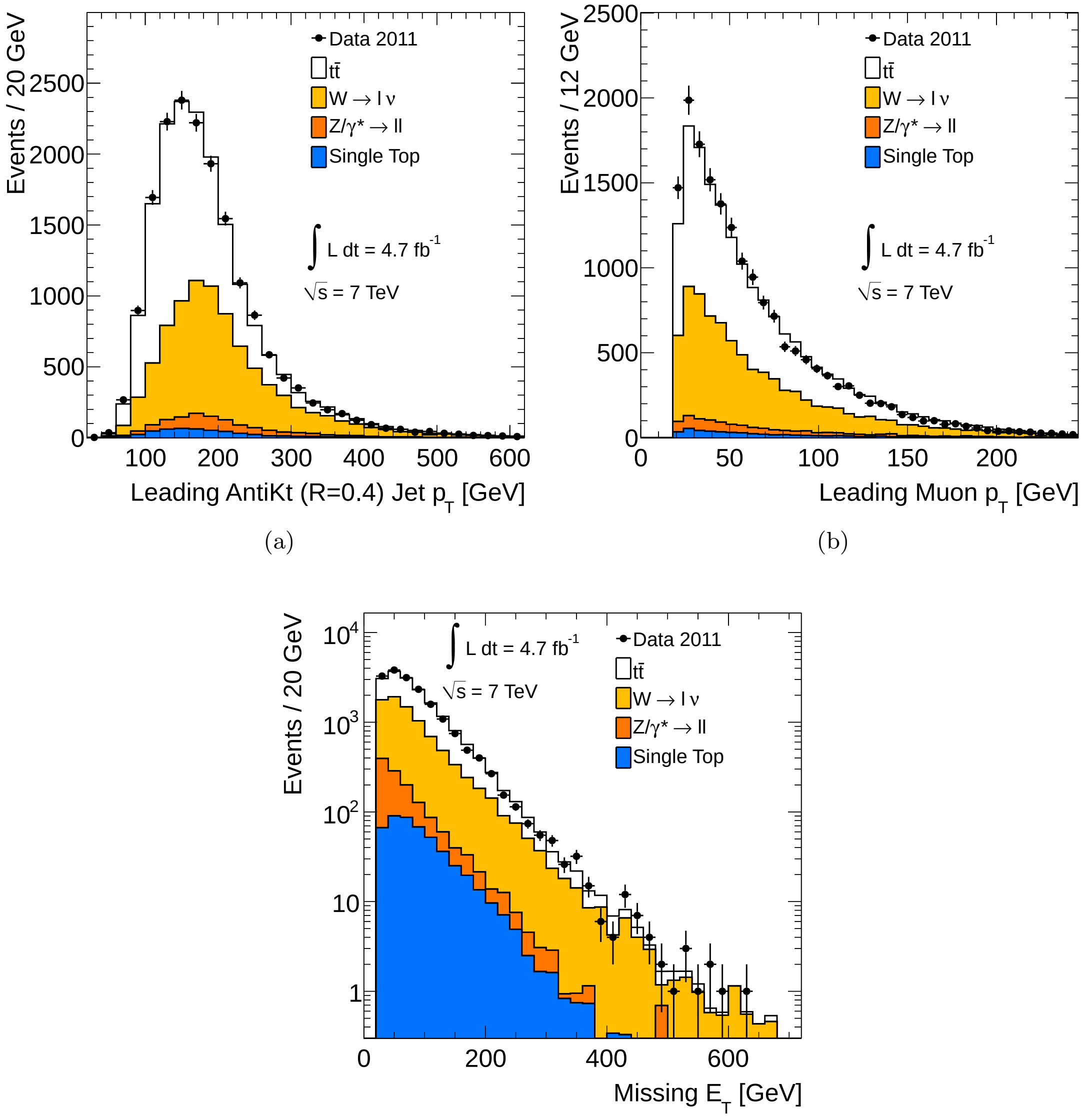

(a)

(b)

(c)

Figure 6.6: Distribution of (a) the leading anti-k_t(R=0.4) jet p_{T}, (b) the leading muon p_{T} and (c) the $E_{\mathrm{T}}^{\mathrm{miss}}$ in data after application of all selection criteria before applying the HEPTopTagger algorithm. Also shown are the predicted SM $t\bar{t}$ production, contributions from W bosons or Z bosons produced in association with jets and single top production. The vertical bars represent the statistical uncertainty of the data events.

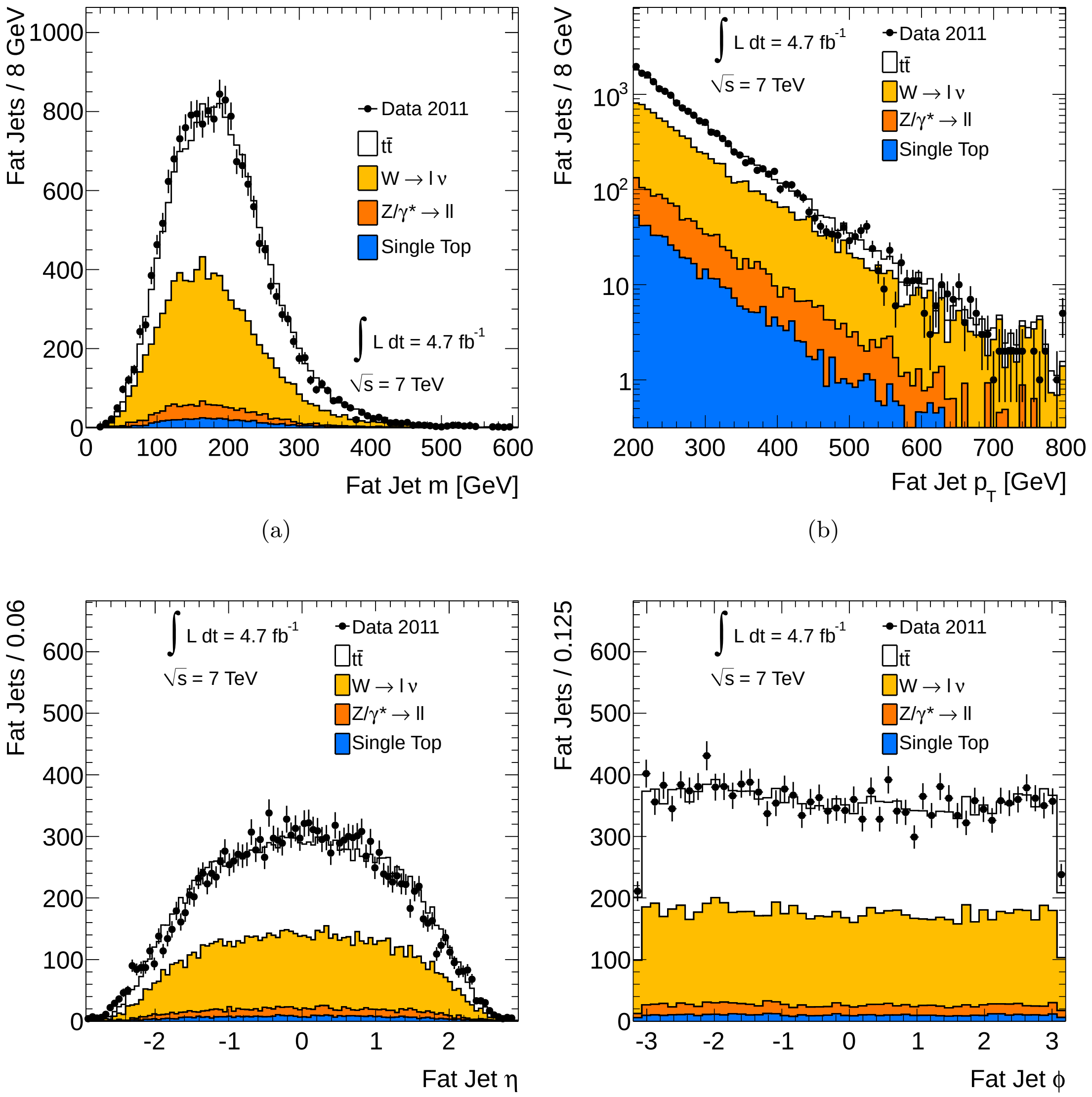

(a)

(b)

(c)

(d)

Figure 6.7: Distribution of (a) fat jet mass, (b) the fat jet p_{T}, (c) the fat jet η and (d) the fat jet ϕ in data after application of all selection criteria before applying the HEPTopTagger algorithm. Also shown are the predicted SM $t\bar{t}$ production, contributions from W bosons or Z bosons produced in association with jets and single top production. The vertical bars represent the statistical uncertainty of the data events.

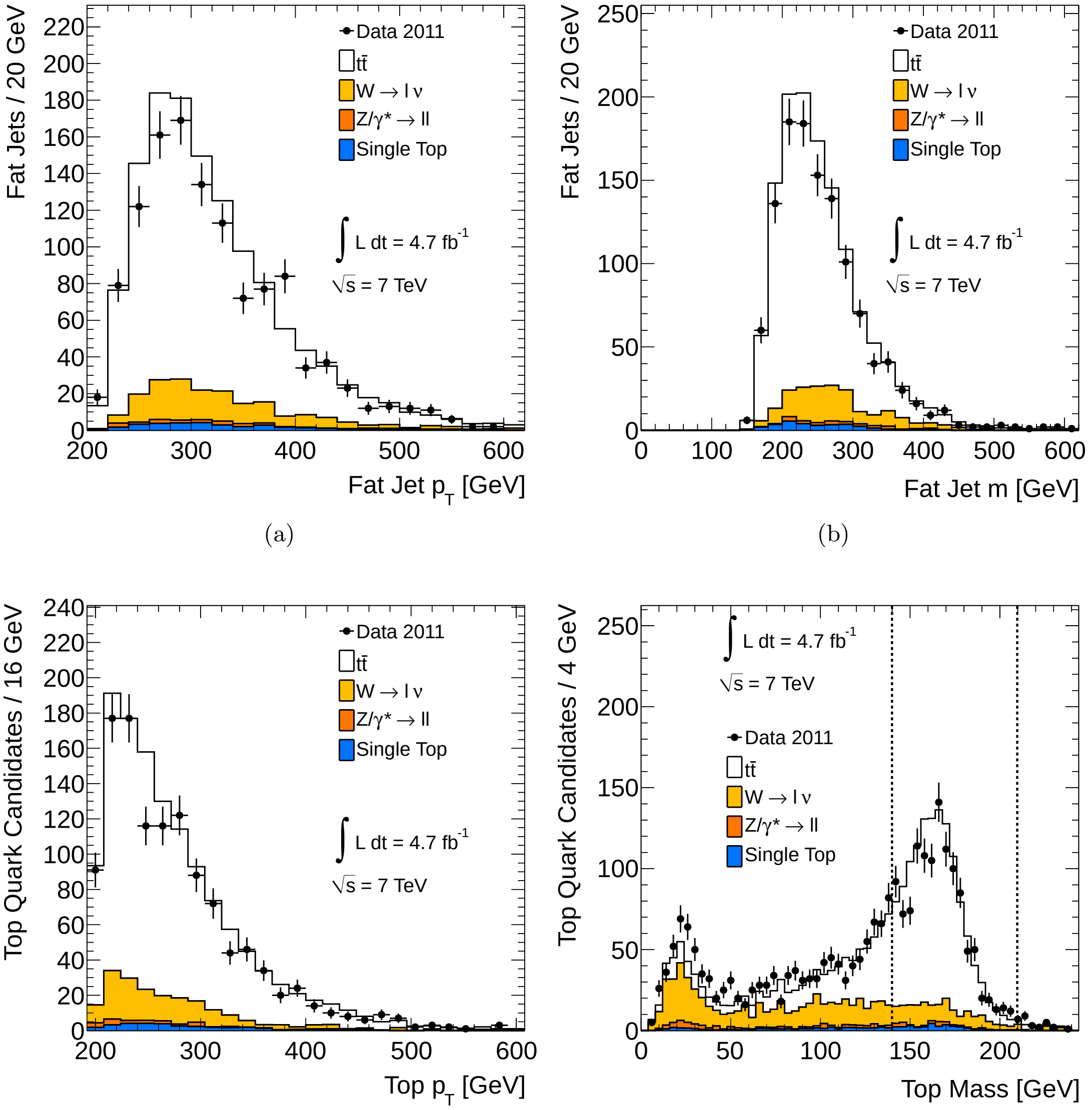

(a) (b)

(c) (d)

Figure 6.8: Distribution of (a) fat jet p_{T}, (b) the fat jet mass, (c) the top candidate p_{T} and (d) the top quark candidate mass in data after application of all selection criteria and the additional requirement of one HEPTopTagger top quark candidate. Also shown are the predicted SM $t\bar{t}$ production, contributions from W bosons or Z bosons produced in association with jets and single top production. For the distribution of the mass the requirement that the mass must lie between 140 GeV and 210 GeV is removed and the limits are indicated by vertical lines. The vertical bars represent the statistical uncertainty of the data events.

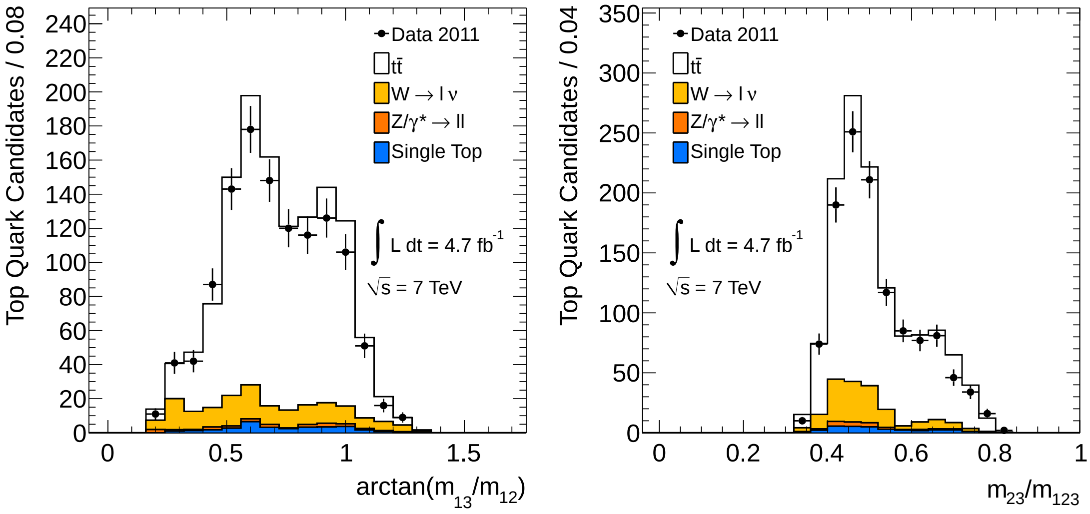

(a) (b)

Figure 6.9: Distribution of substructure variables (a) arctan m_{13}/m_{12} and (b) m_{23}/m_{123} after application of all selection criteria and the additional requirement of one HEPTopTagger top quark candidate. Also shown are the predicted SM $t\bar{t}$ production, contributions from W bosons or Z bosons produced in association with jets and single top production. The vertical bars represent the statistical uncertainty of the data events.

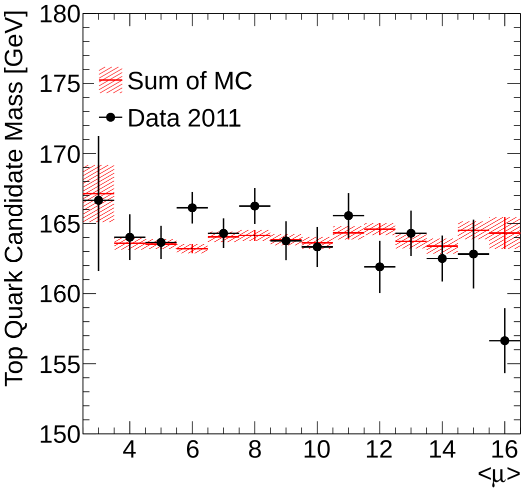

Figure 6.10: Distributions of the mean HEPTopTagger top-quark candidate mass as a function of the average number of interactions per bunch-crossing, $\langle\mu\rangle$, for data and the sum of simulated SM background $t\bar{t}$ events with the full selection applied. Only the statistical uncertainties are shown. The vertical bars represent the statistical uncertainty.

Chapter 7

Fully Hadronic Resonance Search

In this chapter, a search for new heavy resonances in the $t\bar{t}$ invariant mass spectrum is presented. Two models predicting such resonances are considered: Z' bosons and Kaluza-Klein (KK) gluons. The models are described in more detail in Sec. 2.3. An important difference between the two models is that they predict different relative decay-widths: $\Gamma/m = 1.2\%$ [47] for Z' bosons and $\Gamma/m = 15.3\%$ [24, 25] for Kaluza-Klein gluons.

Most previous searches considered either the di-leptonic or the lepton+jets final state of the $t\bar{t}$ system [121–126]. Recently, the ATLAS Collaboration [127, 128] was able to exclude Z' bosons (KK gluons) with masses between 0.50 and 1.15 TeV (0.5 and 1.5 TeV). Similar results [129] were presented by the CMS Collaboration, utilizing the fully hadronic final state and excluding at 95% C.L. masses up to 1.5 TeV (2.0 TeV) for narrow (broad) Z' signals and a region with a width of ≈ 50 GeV at 1.5 TeV for KK gluon signals.

For this thesis, the HEPTopTagger algorithm, described in Sec. 2.5, is utilized for a search in the fully hadronic final state. First the substructure of fat jets (C/A, $R = 1.5$) is tested for compatibility with the $t \to Wb \to qq'b$ decay chain. The invariant mass of the $t\bar{t}$ system is then calculated from the four-momenta of two such top-quark candidates and examined for resonant structures. In Sec. 6 the HEPTopTagger method has been shown to reliably reconstruct top quarks with $p_{\mathrm{T}} > 200$ GeV[1]. Additional comparisons between data and MC prediction show that its behavior is well modelled in the simulation and robust against pile-up.

The object definitions and event selection — requiring two b-tagged jets and two top-quark candidates — are given in Sec. 7.1. The data and Monte Carlo samples used in this analysis are described in Sec. 4.8. The two most important backgrounds for this study are SM $t\bar{t}$ production and QCD multijet events. The production of SM $t\bar{t}$ events which subsequently decay to the fully hadronic final state is an irreducible background.

Events with multiple jets from the production of gluons and non-top quarks (QCD multijet events) statistically dominate the fully hadronic final state. This background is estimated from data in signal-depleted control regions. For cross-checking this estimate, Pythia [103] Monte Carlo (MC) dijet simulated samples are used. Other backgrounds —

---

[1] The coordinate system is defined in Sec. 4.1.

such as the production of W and Z bosons in association with jets — have a much lower cross-section than QCD multijet production and are included in the estimation of that background. The estimation of the rates and shapes of the $t\bar{t}$ and multijet backgrounds is described in Sec. 7.2.

Systematic uncertanties — with the unertainty on the b-tagging efficiency having the largest impact on the expected exclusion range — are evaluated in Sec. 7.3. The resulting $t\bar{t}$ mass spectrum is presented in Sec. 7.4. As no significant excess is observed in data, exclusion limits on the two models are set.

7.1 Event Selection and Object Reconstruction

The ATLAS trigger menu for 2011 data taking provides trigger chains for jets with two different distance parameters: anti-k_t (R=0.4) and anti-k_t (R=1.0). For low $t\bar{t}$ invariant masses ($m_{t\bar{t}}$) jets from the top-quark decay are well separated and can be reconstructed individually at the trigger level. For these events a high-multiplicity jet trigger can be used: at least five anti-k_t (R=0.4) jets with $E_{\mathrm{T}} > 30$ GeV are required. With increasing $m_{t\bar{t}}$ the jets begin to merge and individual reconstruction becomes impossible. Using the aforementioned anti-k_t ($R = 1.0$) jet trigger is not possible because the jets used in this analysis are reconstructed with a larger distance parameter of $R = 1.5$ and therefore collect more energy. This means that a large fraction of events would be lost by using a high-threshold anti-k_t (R=1.0) trigger. Instead events are selected if at least one anti-k_t ($R = 0.4$) jet with $E_{\mathrm{T}} > 100$ GeV is found and the scalar sum of all jet transverse energies fulfills $\sum E_{\mathrm{T}} > 350$ GeV (> 400 GeV for later data-taking periods). This $\sum E_{\mathrm{T}}$ trigger is indifferent to the precise topology of the top-quark decay (which may change due to splitting and merging), as only the total energy deposited in the calorimeter is considered.

To suppress events from non-collision backgrounds, the primary event vertex is required to have at least five tracks with $p_{\mathrm{T}} > 0.4$ GeV associated to it. If more than one primary vertex candidate is found, the vertex that maximizes $\sum p_{\mathrm{T}}^2$ of the tracks associated with it is used.

The analysis uses various jet finder algorithms and distance parameters to reconstruct top-quark candidates and to suppress background. All jets are formed from topologically-related calorimeter energy deposits (topoclusters), as described in Sec. 4.7.5.

Events are only considered for analysis if at least two fat jets, reconstructed with the C/A algorithm (R=1.5), with $p_{\mathrm{T}} > 200$ GeV at the LCW scale and $|\eta| < 2.5$ are found. The HEPTopTagger algorithm, explained in Sec. 2.5, is then used to test if the substructure of these fat jets is compatible with a hadronic top-quark decay. In that case, an estimate of the top-quark four momentum is returned, otherwise the fat jet is discarded.

Events are required to contain at least two top-quark candidates. The invariant mass, $m_{t\bar{t}}$, is then calculated from the four-momenta of the two leading (in p_{T}) top-quark candidates.

Since the final state of $t\bar{t}$ decays almost always contains two b-quarks, b-tagging of jets can be used to further reduce backgrounds of multiple light quark and/or gluon jets.

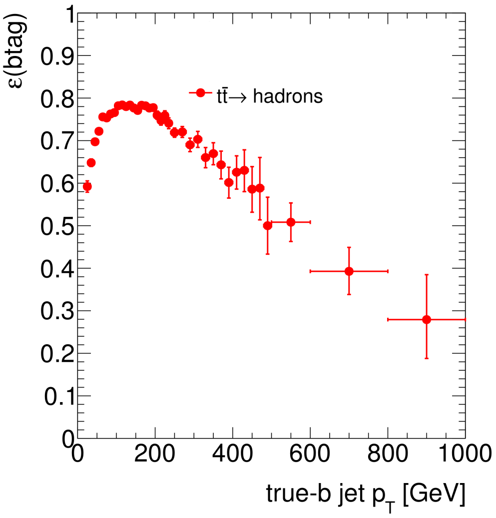

Figure 7.1: Efficiency for finding b-jets as a function of the jet anti-k_t (R=0.4) p_T in $t\bar{t}$ events where both top quarks decay hadronically and two fat jets are found (before top tagging).

The MV1 b-tagging algorithm [101], outlined in Sec. 4.7.6, is used and at least two b-jets are required.

As input to the b-tagging anti-k_t (R=0.4) jets, calibrated to the hadronic scale, are used. To be considered for b-tagging, these jets are required to have $p_{\mathrm{T}} > 25$ GeV and $|\eta| < 2.5$. A fraction of at least 75 % of the transverse momentum of the tracks with $p_{\mathrm{T}} > 0.5$ GeV inside the jet has to be associated to the primary vertex. The angular distance ΔR between b-jets and top-quark candidates cannot exceed 1.4 and only one b-jet can be associated to each top-candidate. The threshold in ΔR was chosen so that the center each b-jets is inside a fat jet.

The b-tagging algorithm is used at a working point with a nominal efficiency of 70 % (Sec. 4.7.6) in a simulated $t\bar{t}$ sample for jets with $p_{\mathrm{T}} > 15$ GeV and $|\eta| < 2.5$ [101]. The efficiency to correctly identify b-jets from decays of high p_{T} top quarks is shown in Figure 7.1 and depends on the jet p_{T}. The efficiency is defined as the number of true b-jets associated to a fat jet divided by the total number of true b-jets. The efficiency decreases for more boosted jets as the charged particles inside the jet become more collimated. The mis-tag rate for light quark and gluon jets was measured to be 2 ± 0.5 % for a jet with $p_{\mathrm{T}} = 200$ GeV and to increase with the p_{T} of the jet [130]. Evaluating the expected mis-tag rate for the pre-selection criteria of this analysis using a MC multijet sample leads to the slightly higher value of ≈ 3 % for a jet of $p_{\mathrm{T}} = 200$ GeV.

Events that contain anti-k_t $R = 0.4$ jets that are identified as resulting from instrumental failure or non-collision background (e.g. cosmic rays, beam gas and beam halo) [65] are rejected. If isolated electrons with $p_{\mathrm{T}} > 25$ GeV or muons with $p_{\mathrm{T}} > 20$ GeV are found, the event is rejected. This is done to veto events from semi-leptonic decays of the $t\bar{t}$ system.

The distributions of (a) the mean reconstructed top-quark candidate mass and (b)

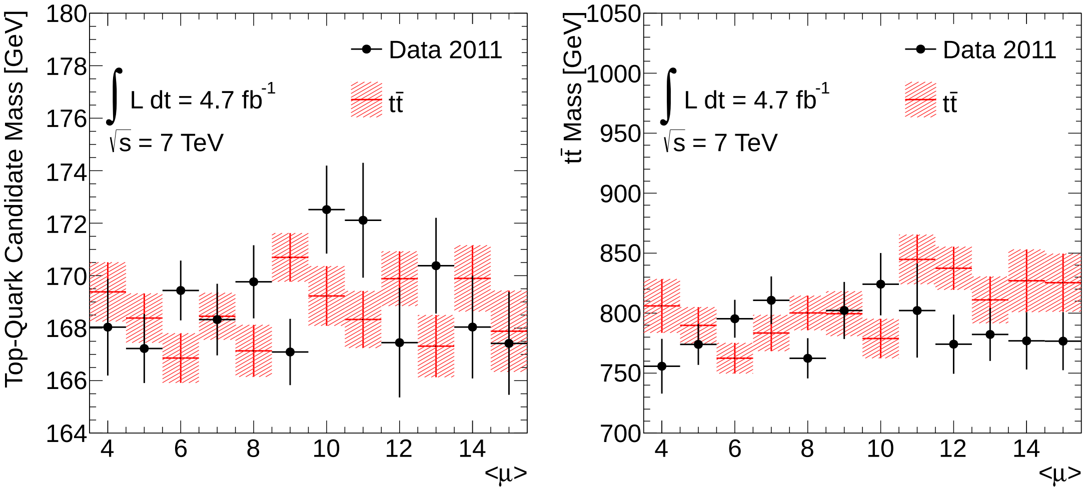

(a) (b)

Figure 7.2: The (a) mean HEPTopTagger top-quark candidate mass and (b) mean reconstructed $t\bar{t}$ mass. The quantities are shown as a function of the average number of interactions per bunch crossing ($\langle\mu\rangle$) for data and events from $t\bar{t}$ MC simulation. The full event selection is applied. Only statistical uncertainties are shown.

the mean reconstructed $t\bar{t}$ mass as a function of the average number of interactions per bunch crossing, $\langle\mu\rangle$, is shown in Fig. 7.2 for events statisfying all selection requirements. Within statistical uncertainties all masses are robust against increased pile-up.

In Fig. 7.3 the distribution of the reconstructed $t\bar{t}$ mass for Z' and KK gluon signal samples, assuming different masses, is presented. For signal masses below 2 TeV the reconstructed mass is well centered around the true value. For higher signal masses, the mass of the new particle is underestimated for a large fraction of events. This under-estimation is caused by two effects. First, as discussed in Sec. 6.2, the transverse momentum of high p_{T} top quarks is underestimated by up to 9 %. Second, the b-tagging efficiency decreases for boosted b-jets (Fig. 7.1) which affects the peak stronger than the (lower p_{T}) continuum tail.

In Table 7.1 the selection efficiency for various Z' boson and KK gluon mass points is listed for different selection criteria. All final states of the $t\bar{t}$ decay are included in the calculation of the efficiency. The efficiency with which at least two fat jets are found in an event increases from $\approx 33\,\%$ for the 0.8 TeV Z' sample to $\approx 60\,\%$ for higher signal masses. The 0.5 TeV Z' sample is practically inaccessible as only for $\approx 4\,\%$ of the events two fat jets are found.

When at least two b-tagged jets are required in addition to the fat jets, the efficiency for the 0.8 TeV Z' sample is $\approx 13\,\%$ and increases to up to $\approx 22\,\%$ for the 1.3 TeV Z' sample. For higher signal masses the efficiency with which b-jets are found decreases again. This happens because the b-tagging efficiency, as shown in Fig. 7.1, drops for boosted

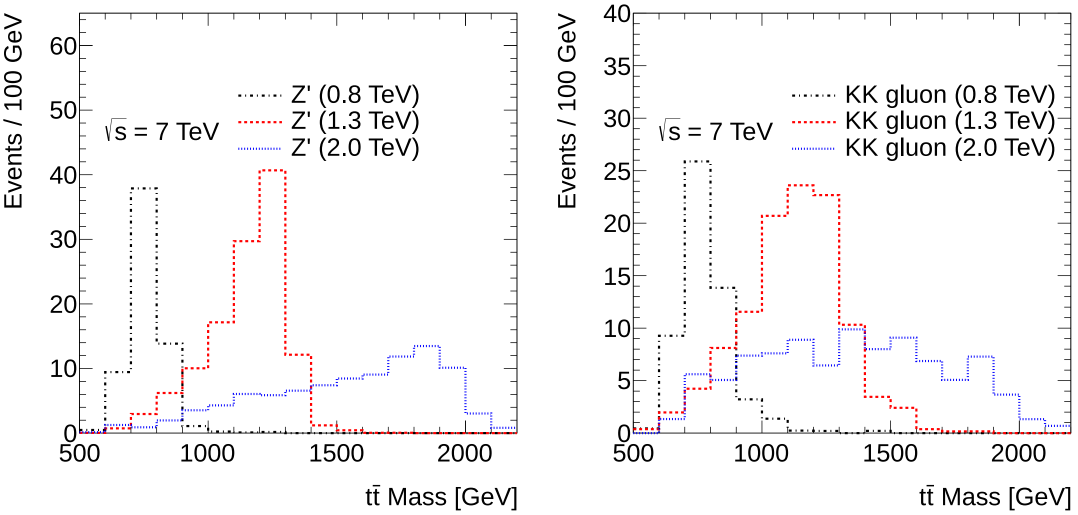

(a) (b)

Figure 7.3: Distributions of reconstructed $t\bar{t}$ mass for (a) Z' boson and (b) KK gluon models with masses of 0.8 TeV, 1.3 TeV and 2.0 TeV. The distributions correspond to an integrated luminosity of 4.7 fb^{-1} and $\sigma(pp \to Z'/\mathrm{KK\,gluon}) \times BR(Z'/\mathrm{KK\,gluon} \to t\bar{t}) = 1\,\mathrm{pb}$ is assumed.

b-jets. Requiring at least two top-quark candidates identified using the HEPTopTagger algorithm yields an efficiency that increases with the mass of the signal sample up to a maximum of $\approx 6\,\%$. The maximum total selection efficiency for the Z' sample is 2.6 % for a signal mass of 1.3 TeV. Dividing this number by the branching fraction of 46% for the fully hadronic final state yields a maximum total selection efficiency for the fully hadronic final state of 5.7 %.

For the KK gluon resonance the efficiencies are reduced by up to 20 % compared to Z' samples with the same mass. This effect is predominantly due to the larger width of the KK gluon resonance. The larger width means that the tail of the fat jet p_{T} distribution extends towards lower values, where the reconstruction efficiency drops sharply (Fig. 6.4). The difference in efficiency is largest between the efficieny of finding two fat jets in the event. After the full selection the maximum difference in efficiency between the two signals (for equal resonance masses) is 12 %. It is zero for a resonance mass of 2 TeV.

The two most important contributions to the efficiency are the top-tagging and b-tagging efficiencies which depend on the top-quark momentum. This leads to a maximum value of:

$$\varepsilon^2_{b\text{-tag, max}} \cdot \varepsilon^2_{\text{top-tag, max}} \approx 10\%. \tag{7.1}$$

Here $\varepsilon_{b\text{-tag, max}}$ is the maximal b-tagging efficiency of 80% and $\varepsilon_{\text{top-tag, max}}$ the maximal top-tagging efficiency of 40% for hadronically-decaying top quarks.

The event yields recorded in data after applying all selection criteria and various top-tagging and b-tagging requirements are presented in Table 7.2. Before selecting top quarks and b quarks, approximately 20 million events are found in data. Only ≈ 1000 events are found when two top-tags and two b-tags are required. Under the conservative assumption that a signal of new physics will only contribute a small overall number of events with respect to the backgrounds, the backgrounds are therefore reduced by a factor of 20000 while an efficiency of up to 5 % is maintained for signal samples.

Table 7.1: Selection efficiency (in %) for different selection criteria and resonance masses for Z' bosons and KK gluons (g_{KK}) that have decayed to $t\bar{t}$ pairs. All $t\bar{t}$ final states are included in the calculation of the efficiency. The statistical uncertainty on the efficiencies is included in the table.

Model	≥ 2 fat jets	≥ 2 fat jets ≥ 2 b-tags	≥ 2 top-tags	≥ 2 top-tags ≥ 2 b-tags
Z' (0.5 TeV)	3.64 ± 0.06	0.86 ± 0.03	0.05 ± 0.01	0.02 ± 0.00
Z' (0.8 TeV)	33.16 ± 0.18	13.45 ± 0.11	2.42 ± 0.05	1.36 ± 0.04
Z' (1.0 TeV)	44.99 ± 0.19	18.72 ± 0.12	4.02 ± 0.06	2.19 ± 0.04
Z' (1.3 TeV)	54.71 ± 0.24	21.83 ± 0.14	5.25 ± 0.07	2.61 ± 0.05
Z' (1.6 TeV)	60.19 ± 0.23	21.32 ± 0.13	5.85 ± 0.07	2.48 ± 0.04
Z' (2.0 TeV)	63.90 ± 0.25	19.07 ± 0.13	5.87 ± 0.08	2.04 ± 0.04
g_{KK} (0.7 TeV)	19.23 ± 0.31	7.57 ± 0.19	1.39 ± 0.08	0.78 ± 0.06
g_{KK} (1.0 TeV)	38.60 ± 0.44	16.35 ± 0.28	3.53 ± 0.13	1.90 ± 0.10
g_{KK} (1.3 TeV)	47.14 ± 0.49	18.77 ± 0.30	4.71 ± 0.15	2.37 ± 0.11
g_{KK} (1.6 TeV)	49.65 ± 0.50	18.54 ± 0.30	4.89 ± 0.16	2.17 ± 0.10
g_{KK} (2.0 TeV)	50.51 ± 0.51	17.02 ± 0.28	4.73 ± 0.15	2.04 ± 0.10

Table 7.2: Total number of events recorded in data for different b-tagging and top-tagging requirements. The events are required to pass the other event selection criteria (e.g. at least two fat jets with $p_{\mathrm{T}} > 200$ GeV need to be found) listed in the main text.

	before top-tagging	1 top-tag	≥ 2 top-tags
before b-tagging	$20.6 \cdot 10^6$	$671 \cdot 10^3$	$8.3 \cdot 10^3$
1 b-tag	$2.9 \cdot 10^6$	$129 \cdot 10^3$	$2.1 \cdot 10^3$
≥ 2 b-tags	$207 \cdot 10^3$	$15 \cdot 10^3$	$0.95 \cdot 10^3$

7.2 Background Estimates

The background contribution to the signal region is estimated using data control regions with relaxed requirements on the number of top-quark candidates and on the number of associated b-tagged jets. Six classes of events, as listed in Table 7.3, are used. In the table the estimated $t\bar{t}$ purities for each region are shown. The signal region F has a purity of $\approx 81\,\%$. The multijet background is dominant in the other regions. The most discernible contribution from signal samples is — similar to SM $t\bar{t}$ — expected in the region F. The estimation of the multijet background and the SM $t\bar{t}$ background are described in Sec. 7.2.1 and Sec. 7.2.2, respectively. The distributions of various control variables, showing a comparison of data and the estimated backgrounds, are presented in Sec. 7.2.3.

7.2.1 Multijet Estimate

The QCD multijet background shape and normalization are estimated from data, using the so-called *ABCD method*. The distribution of events in two variables x and y is termed independent if the probability density function $\rho(x, y)$ can be expressed using two functions $f(x)$ and $g(y)$:

$$\rho(x, y) = f(x)g(y).$$

The event counts in the regions — illustrated in Fig. 7.4 — can be calculated as:

$$n_I = \int_{x_1}^{x_2} \int_{y_1}^{y_2} dxdy\rho(x, y);$$

$$n_{II} = \int_{x_3}^{x_4} \int_{y_1}^{y_2} dxdy\rho(x, y);$$

$$n_{III} = \int_{x_1}^{x_2} \int_{y_3}^{y_4} dxdy\rho(x, y)$$

and

$$n_{IV} = \int_{x_3}^{x_4} \int_{y_3}^{y_4} dxdy\rho(x, y).$$

The central equation of the ABCD method is:

$$\frac{n_I}{n_{II}} = \frac{n_{III}}{n_{IV}},$$

the correctness of which can be shown by inserting the definitions of n_I to n_{IV}. This relation can be used to estimate the event count in a region where no direct measurement (e.g. due to the potential presence of a signal) is possible:

$$n_{IV,\text{est.}} = n_{III} \frac{n_{II}}{n_I}.$$

The multijet background is estimated under the assumption that for this background the probabilities for mis-tagging lighter quarks and gluons as top quarks with the HEP-TopTagger algorithm or as b quarks using the MV1 technique are independent and that

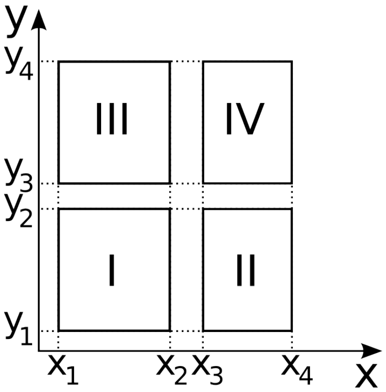

Figure 7.4: Illustration of the regions used in the ABCD method for the general case. The regions are named using roman numerals to avoid confusion with the regions used for the actual analysis which are denoted by the letters A to F.

Table 7.3: The six regions used for estimating the $t\bar{t}$ and multijet backgrounds. For each region the estimated purity of $t\bar{t}$ events is listed in parentheses. The purity is calculated as the expected number of events from SM $t\bar{t}$ production divided by the number of observed events in that region.

	1 top-tag	≥ 2 top-tags
no b-tag	A(0.3%)	B(2.4%)
1 b-tag	C(3.2%)	D(24.3%)
≥ 2 b-tags	E(22.5%)	F(80.9%)

the shape of distributions in the regions with the same numbers of top-quark candidates (B, D and F) is the same. Two initial observations support this assumption: firstly, the b-tagging information is not directly used in the HEPTopTagger and secondly the b- and top-tagging algorithms utilize different properties of the event. It is further supported by the agreement observed between data and prediction for various control variables which is presented in Sec. 7.2.3.

The multijet background in region F as function of a given variable (e.g. $m_{t\bar{t}}$) is estimated using the ABCD method twice, with different sets of regions. Firstly, the shape in region B ($\frac{\mathrm{d}n_B}{\mathrm{d}m_{t\bar{t}}}$) is normalized by the ratio of event counts in regions A and E:

$$\frac{\mathrm{d}n'_F}{\mathrm{d}m_{t\bar{t}}} = \frac{n_E}{n_A}\frac{\mathrm{d}n_B}{\mathrm{d}m_{t\bar{t}}}. \tag{7.2}$$

The n_i are the recorded event counts in different regions after subtracting the SM $t\bar{t}$ background. This subtraction leads to an anti-correlation of $t\bar{t}$ and multijet backgrounds. The second estimate is performed using regions D and C instead of B and A, respectively:

$$\frac{\mathrm{d}n''_F}{\mathrm{d}m_{t\bar{t}}} = \frac{n_E}{n_C}\frac{\mathrm{d}n_D}{\mathrm{d}m_{t\bar{t}}}. \tag{7.3}$$

The final prediction is calculated as the mean of these two estimates:

$$\frac{\mathrm{d}n_F}{\mathrm{d}m_{t\bar{t}}} = \frac{1}{2}\left(\frac{\mathrm{d}n'_F}{\mathrm{d}m_{t\bar{t}}} + \frac{\mathrm{d}n''_F}{\mathrm{d}m_{t\bar{t}}}\right). \tag{7.4}$$

Instead of using the arithmetic mean of the two estimates, n'_F and n''_F, to calculate the final estimate n_F, it is also possible to weight both estimates according to their respective statistical uncertainties. However, this would decrease the influence of the second estimate (n''_F), which is calculated using the regions (C, D) that resemble the signal region most closely, but contain fewer events than the regions A and B. The estimated number of multijet events is 132 for the signal region F.

7.2.2 $t\bar{t}$ Estimate

The distributions of all variables for the SM $t\bar{t}$ background are taken from MC simulation while the normalization is estimated using data from region E by utilizing the different shapes of the top quark candidate mass distribution for the $t\bar{t}$ and multijet backgrounds.

The top-quark candidate mass distribution in region E from the $t\bar{t}$ MC sample is used as the $t\bar{t}$ template. The multijet template is extracted from region C after subtracting the contribution expected from SM $t\bar{t}$ production in that region. The expected fraction of $t\bar{t}$ events in region C of $\approx 3\,\%$ (Table 7.3) is small. Region C is used for extracting the multijet template because it differs from region E (for which the fit is perfomed) only in the b-tag multiplicity and therefore the top-quark candidate mass distributions are expected to be similar. A comparison of the multijet template and the multijet MC prediction for region E for the top-quark candidate mass distribution is presented in Fig. 7.5a. The distributions agree within the statistical uncertainties of the multijet MC prediction.

The SM $t\bar{t}$ and multijet template distributions are shown in Fig. 7.5b. The normalization of SM $t\bar{t}$ production is then measured by fitting the $t\bar{t}$ and multijet templates to the data. A weight is assigned to each template and the weights are varied to minimize the error-weighted sum of the residual differences for each bin between the sum of the templates and the data.

Because the multijet template is estimated by subtracting the SM $t\bar{t}$ contribution from data in region C it is sensitive to the $t\bar{t}$ normalization. To ensure that the derived $t\bar{t}$ normalization is stable, the multijet template is updated using the new normalization and the fit is repeated until the relative change in the normalization from one iteration to the next is below 10^{-5}.

After five iterations, the fit results in a ratio of measured $t\bar{t}$ yield to the expected yield of 1.01. The statistical uncertainty on the the result of the fit is 0.09. This ratio is used to correct the normalization of the SM $t\bar{t}$ background when estimating the multijet background as described in Sec.7.2.1. The estimated SM $t\bar{t}$ yield in the signal region is 766 events.

7.2.3 Control Distributions

In the following, control distributions to verify that multijet and SM $t\bar{t}$ background predictions are consistent with data are presented. The sum of multijet and $t\bar{t}$ background

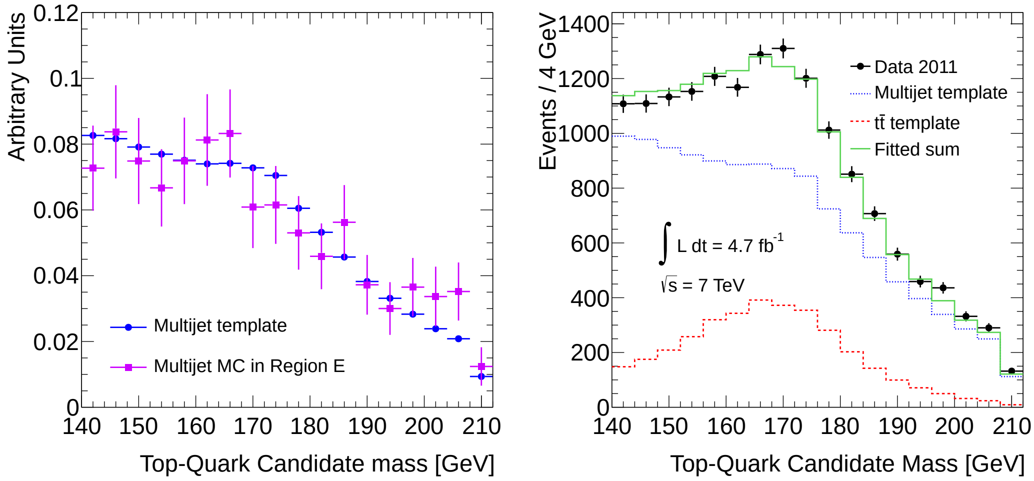

Figure 7.5: Distributions of the top-quark candidate mass in control-region E showing (a) a comparison of the mulijet template and the multijet MC predictions as well as (b) the data and the templates for multijet and SM $t\bar{t}$ production together with the fitted sum. For the left figure the distributions are weighted so that the area under each histogram equals one. The vertical bars represent the statistical uncertainty.

distributions for the jet mass (Fig. 7.6a) and the top-quark candidate mass (Fig. 7.6b) describe the distributions observed in data well, with a small upwards fluctuation for a fat jet mass around 250 GeV. The SM $t\bar{t}$ distribution shows a sharp peak around a top-quark candidate mass of 170 GeV whereas the distribution is flat for the multijet background. The fat jet p_{T} (Fig. 7.7a) and the top-quark candidate p_{T} (Fig. 7.7b) are well described with a small upwards fluctuation in data visible at a p_{T} of ≈ 300 GeV. For a large fraction of events the leading sub-jet p_{T} (Fig. 7.8a) is below 300 GeV, the sub-leading sub-jet p_{T} (Fig. 7.8b) is below 200 GeV and the sub-sub-leading sub-jet p_{T} (Fig. 7.8b) is below 150 GeV. The substructure variables m_{23}/m_{123} (Fig. 7.9a) and $\arctan(m_{13}/m_{12})$ (Fig. 7.9b) are described in Sec. 2.5. The agreement between data and the sum of multijet and SM $t\bar{t}$ background is good for all distribution.

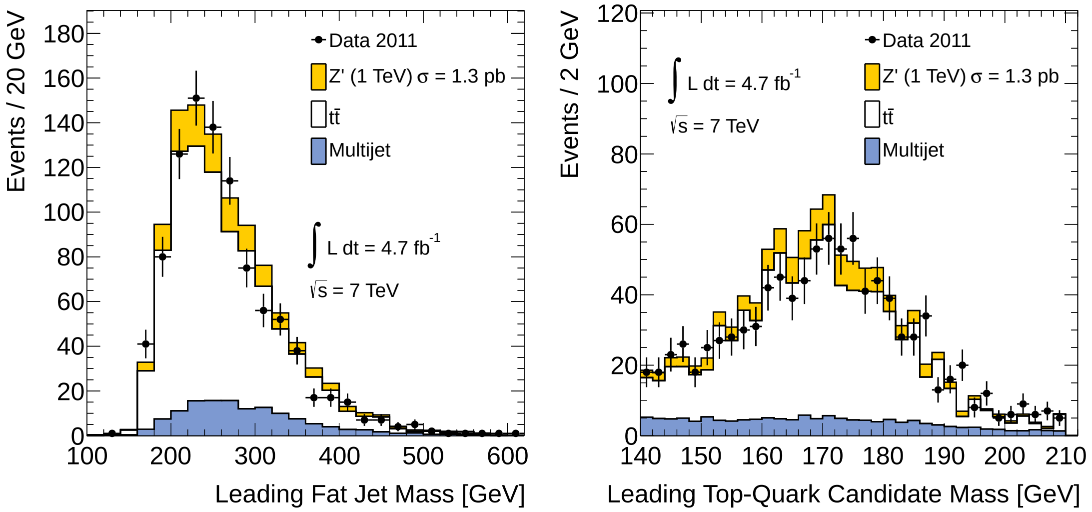

(a) (b)

Figure 7.6: Distribution of (a) the mass of the leading p_{T} fat jet and (b) the mass of the leading p_{T} top-quark candidate in the signal region together with the prediction for SM $t\bar{t}$ production, the multijet background contribution as estimated from data, and a hypothetical Z' boson signal. The vertical bars represent the statistical uncertainty of the data events.

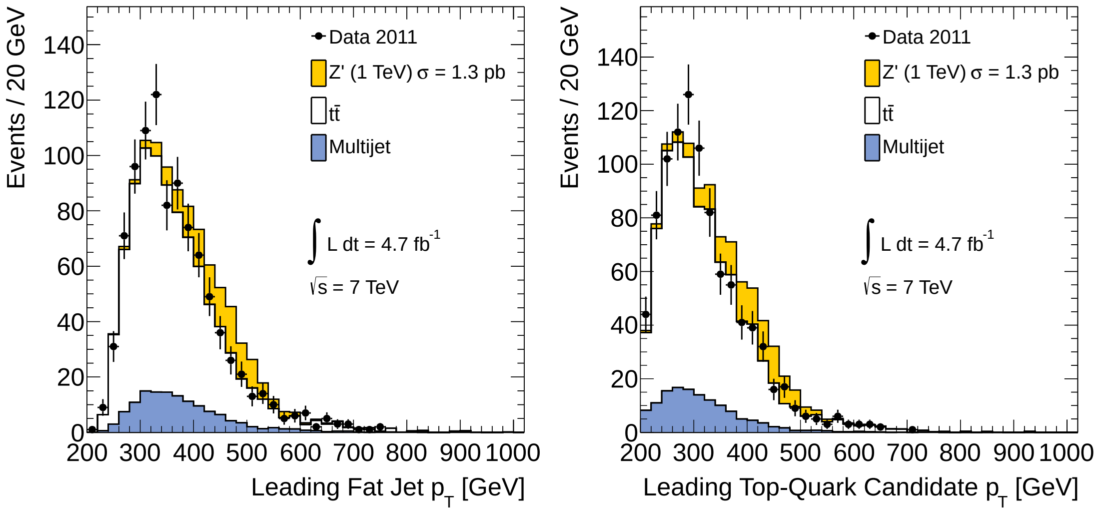

(a) (b)

Figure 7.7: Distribution of (a) the fat jet p_{T} and (b) HEPTopTagger top-quark candidate p_{T} in the signal region together with the prediction for SM $t\bar{t}$ production, the multijet background contribution as estimated from data, and a hypothetical Z' boson signal. The vertical bars represent the statistical uncertainty of the data events.

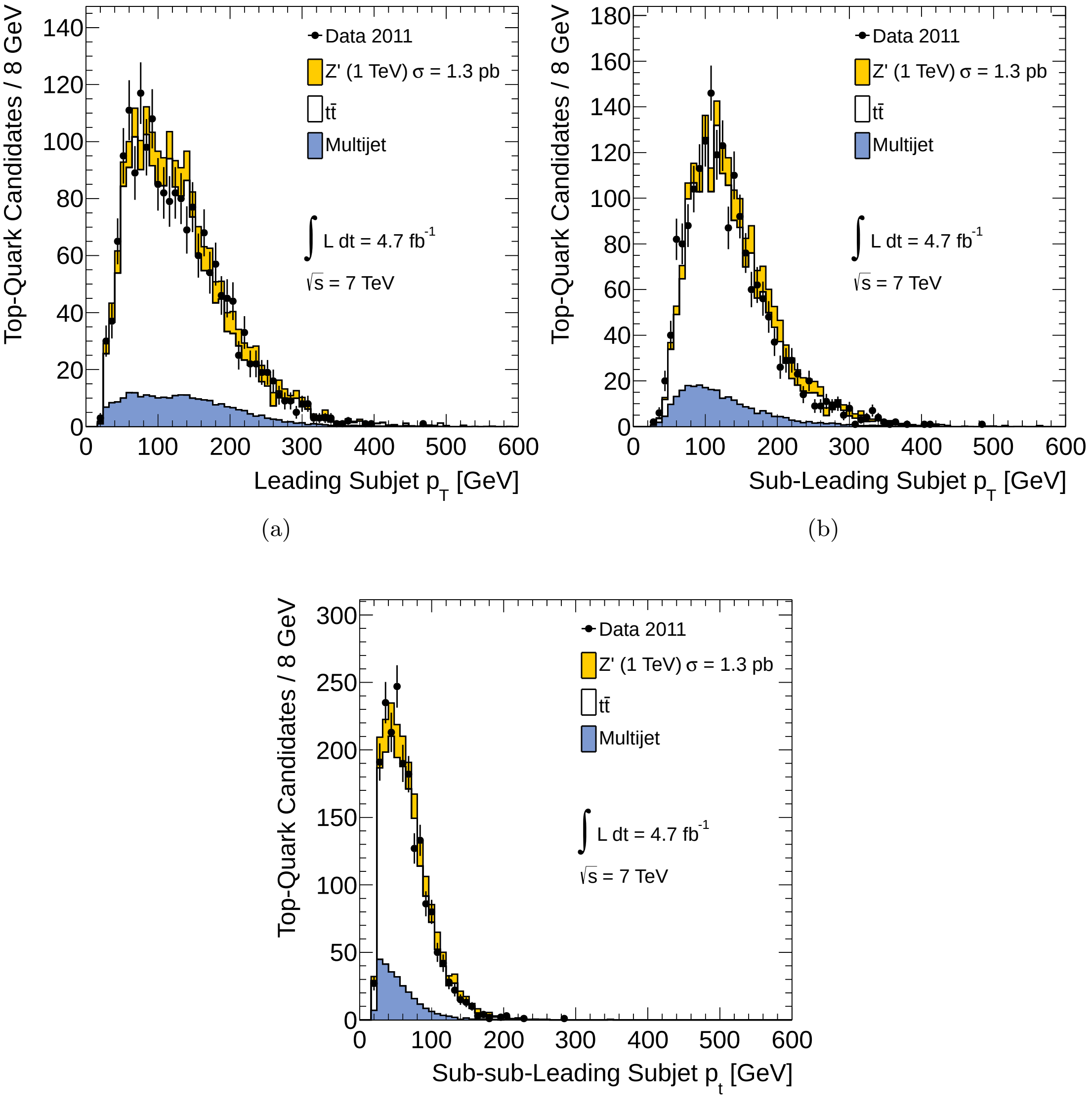

(a)

(b)

(c)

Figure 7.8: Distributions of the (a) leading, (b) sub-leading and (c) sub-sub-leading sub-jet p_{T} in the signal region together with the prediction for SM $t\bar{t}$ production, the multijet background contribution as estimated from data, and a hypothetical Z' boson signal. The vertical bars represent the statistical uncertainty of the data events.

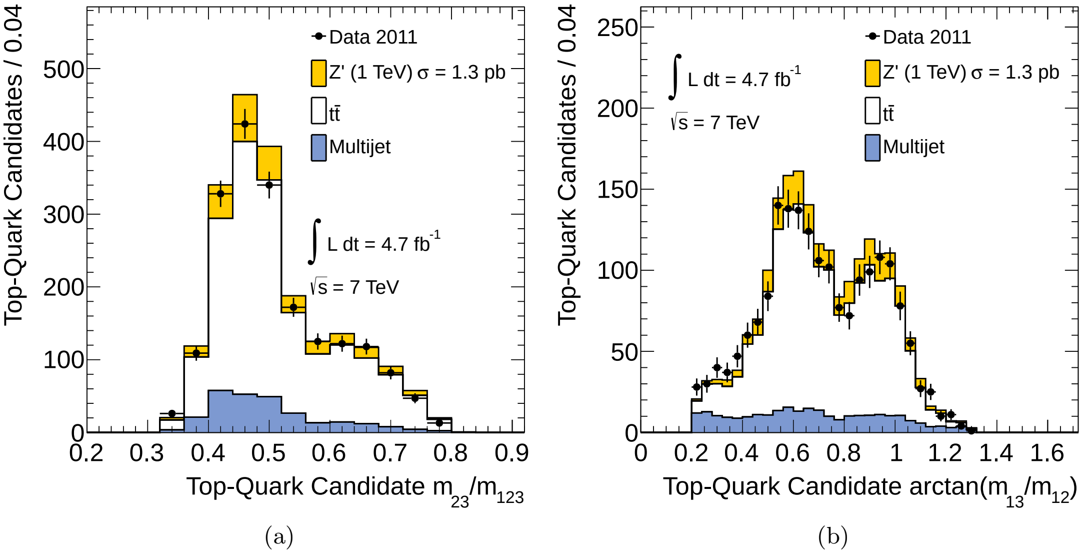

Figure 7.9: Distribution of the (a) substructure variables m_{23}/m_{123} and (b) $\arctan(m_{13}/m_{12})$ in the signal region together with the prediction for SM $t\bar{t}$ production, the multijet background contribution as estimated from data, and a hypothetical Z' boson signal. The vertical bars represent the statistical uncertainty of the data events.

7.3 Systematic Uncertainties

The estimated $m_{t\bar{t}}$ distribution for the backgrounds and various signal models is affected by systematic uncertainties. The sources of these uncertainties are described in the following.

The final normalization of the SM $t\bar{t}$ contribution is estimated in the limit setting procedure. This is explained in more detail in Sec. 7.4. This implies that for the SM $t\bar{t}$ sample only the shape and not the normalization is influenced by systematic uncertainties. The relative importance of the different systematic uncertainties on the final result is evaluated in Sec. 7.4.

The following systematic uncertainties are considered:

- b-tagging efficiency;
- Jet energy scales;
- Jet energy resolution;
- PDF uncertainties;
- Initial State Radiation/Final State Radiation;
- Integrated luminosity;
- Higher order QCD corrections;
- Higher order EW corrections;
- Parton Shower uncertainties;
- $t\bar{t}$ normalization and
- uncertainty on the multijet background estimate.

7.3.1 *b*-Tagging

The reconstruction of b-jets is described in Sec. 4.7.6. The b-tagging efficiency is measured using two different selections of events: one sample containing jets and a muon [101] and a sample of $t\bar{t}$ events [131]. The mis-tag rate is determined using a sample of multijet events [130]. By comparing the measured efficiencies and mis-tag rates with the predictions obtained using MC simulation, scale factors to correct the MC prediction are derived. The scale factors are calculated as a function of the jet p_{T} and η. For all except the highest efficiency b-tagging configurations, the scale factors are $\approx 10\,\%$ below unity.

The limited numbers of events in the MC samples leads to a statistical uncertainty on the b-tagging efficiency scale factors. Dominant effects contributing to the systematic uncertainty on the scale factors are the uncertainty on the ratio of charm quarks to light quarks in jets, the jet-vertex-fraction, the jet-energy resolution and the simulation of jet-fragmentation. Results from different event samples and estimation methods for the scale factors — such as the kinematic fit method and the tag counting method [131] —

are combined to derive the final numbers. In Fig. 7.10 the b-tagging scale factors and uncertainties estimated using a single lepton and a di-lepton $t\bar{t}$ event sample are shown as an example.

The total uncertainty on the scale factors for the MV1 [101] algorithm is $5 - 15\,\%$ for a jet p_{T} of up to 300 GeV and reaches $\approx 36\,\%$ for a jet p_{T} above 500 GeV. The uncertainties are extrapolated towards higher jet p_{T} using a sample of MC simulated $t\bar{t}$ events. The uncertainty on the scale factors for the mis-tag rates is larger, ranging from $18\,\%$ to $48\,\%$, depending on the jet p_{T} and η.

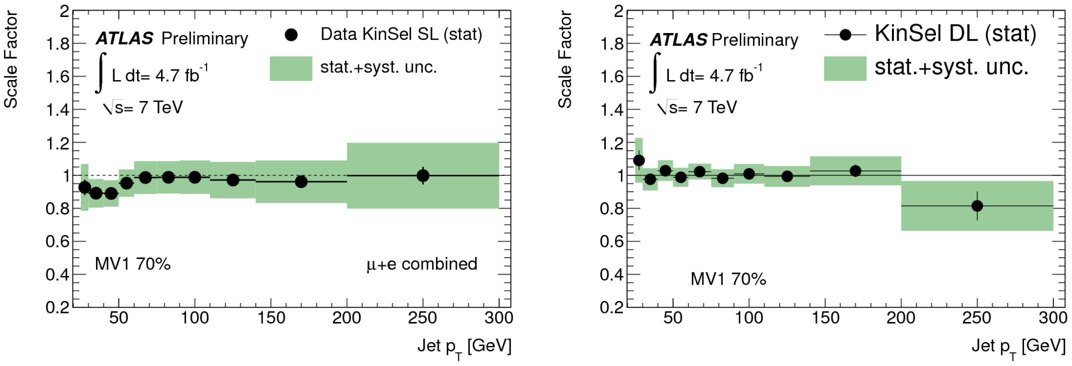

(a) (b)

Figure 7.10: Scale factors for the b-tagging efficiency estimated in a (a) single lepton $t\bar{t}$ event sample and (b) a di-lepton $t\bar{t}$ sample using the kinematic selection method. The statistical uncertainties are indicated by error bars and the green band shows the total uncertainty [131].

The effects of the uncertainties on the b-tagging efficiency and mis-tag rates on the event selection are estimated by re-weighting the events with the scale factors increased and decreased by one standard deviation. Three different factors are considered: the uncertainty on tagging efficiency and mis-tag rate for:

- true b-jets;
- true c-jets and
- true light-quark and gluon jets.

Two per-jet weights are calculated for each of the three uncertainties: one each for the one standard deviation increase and decrease of the tagging efficiency. An event-weight is calculated as the product of the per-jet weights for all jets considered as input to b-tagging.

The resulting change in the $m_{t\bar{t}}$ distribution is shown in Figure 7.11. The SM $t\bar{t}$ distribution, the multijet estimate (via $t\bar{t}$ subtraction) and the Z' and KK gluon signals are affected by this uncertainty.

7.3.2 Jet Energy Scale and Resolution

Two different samples are used to determine the difference in the jet energy scale (JES) between data and simulation [66]. One sample consists mainly of QCD dijet events where light quarks and gluons give rise to jets. The second sample is enriched in $t\bar{t}$ events and was selected using the same criteria as described in Sec. 6.1. As shown in Sec. 6.3 the estimated purity of $t\bar{t}$ events in this sample is $\approx 40\,\%$. The main non-top-quark background is due to the production of W bosons in association with light quark and gluon jets. This sample is well suited for estimating the JES for this analysis as it contains many jets from hadronic decays of top quarks. The uncertainties found using both samples are very similar and the maximum uncertainty is used.

The JES uncertainty is determined by comparing the double ratio of data and simulation and energy of jets constructed from topoclusters and tracks using the same jet-clustering algorithm. It varies as a function of the distance parameter, jet p_{T} and jet η. The difference between data and simulation lies between 2.3% and 6.8%

The jet energy resolution (JER) was determined using the p_{T} asymmetry in dijet events [132]. Because the resolution in simulated events was better than what was observed in data the simulated resolution is accordingly worsened.

The JES uncertainty is considered to be fully correlated between signal and background samples and between subjets and fat jets. Four different regions in jet p_{T} are chosen between which the uncertainty is independently varied up or down by one standard deviation. For the subjets the regions are: $p_{\mathrm{T}} < 50$ GeV, $50 < p_{\mathrm{T}} < 150$ GeV, $150 < p_{\mathrm{T}} < 300$ GeV, $300 < p_{\mathrm{T}} < 500$ GeV and $p_{\mathrm{T}} > 500$ GeV. In Fig. 7.12 the effect of these uncertainties on $m_{t\bar{t}}$ for the $t\bar{t}$ sample is presented. The SM $t\bar{t}$ distribution, the multijet estimate (via $t\bar{t}$ subtraction) and the Z' and KK gluon signals are affected by this uncertainty.

7.3.3 Parton Distribution Functions

The uncertainty on the $m_{t\bar{t}}$ distribution due to the uncertainties on the PDF is determined using the the eigenvector approach [133]. First the variations within three PDF sets (intra-PDF uncertainty) are evaluated. In a second step these are combined to yield the final PDF uncertainty. The method follows the recommendation of the PDF4LHC working group [134]. The following PDF sets are considered:

- CT10 [108] (53 variations)
- MSTW2008nlo68cl [135] (41 variations)
- NNPDF2.1 [38] (101 variations)

For the CT10 set the uncertainty is calculated as the symmetric Hessian of the varied distributions:

$$\Delta X = 0.5 \cdot \sqrt{\sum_i \left(X_{i+} - X_{i-}\right)^2}$$

Here ΔX is the resulting uncertainty and X_{i+} (X_{i+}) and are one standard deviation up (down) shifts of individual parameters of the PDF set.

The intra-PDF uncertainty for the MSTW2008nlo68cl PDF set is evaluated using an asymmetric Hessian approach:

$$\Delta X_{+} = \sqrt{\sum_i (X_i - X_0)^2} \text{ if } X_i - X_0 > 0$$

$$\Delta X_{-} = \sqrt{\sum_i (X_i - X_0)^2} \text{ if } X_i - X_0 < 0$$

where ΔX_{+} (ΔX_{-}) is the resulting one standard deviation up (down) shift and X_0 the central value. For the NNPDF2.1 set the variation is taken to be the standard deviation of the ensemble of individual variations.

The inter-PDF uncertainty is then derived as the envelope of the three intra-PDF uncertainties. For each bin in $m_{t\bar{t}}$ the maximum difference between up- and down-variations is calculated and the uncertainty is taken to be half this difference. For the signal samples the same procedure is used. The importance of the uncertainty depends very much on the mass of the new resonance.

The impact of this uncertainty on the $m_{t\bar{t}}$ distribution in Figure 7.14. For a low-mass signal (Fig. 7.14a) the difference between the 1-σ upwards- and downwards-variations is negligible. It increases with the mass of the hypothetical new particle and is $\approx 20\,\%$ for a Z' mass of 2 TeV (Fig. 7.14b). The increase of the PDF uncertainty with the invariant mass for $t\bar{t}$ events is presented in Fig. 7.14c.

The large PDF uncertainty for high invariant masses is one of the main reasons that no signal samples with masses above 2 TeV are used for this analysis. The PDF uncertainty at high $m_{t\bar{t}}$ is due to the large uncertainty on PDFs at large values of the momentum fraction x. As an example the uncertainty on the CT10 gluon-PDF is shown in Fig. 7.13 as a function of x.

Similar searches for new particles in the future can be improved by using updated PDF sets which include measurements made using LHC data and therefore have a reduced uncertainty at high x [136, 137].

The SM $t\bar{t}$ distribution, the multijet estimate (via $t\bar{t}$ subtraction) and the Z' and KK gluon signals are affected by this uncertainty.

7.3.4 Initial State Radiation/Final State Radiation

The effect of QCD initial state and final state radiation (ISR/FSR) on the simulated SM $t\bar{t}$ sample is estimated. Two $t\bar{t}$ samples are created using the AcerMC [138] MC generator interfaced to Pythia [103] for simulating the parton shower. For one sample the parameters affecting the simulation of ISR/FSR are increased, for the other one these are decreased.

Four different parameters are varied: a variable that controls high-p_{T} ISR branching (named PARP(67) in Pythia), the multiplicative factor of the momentum scale squared when calculating the scale-evolution of α_S for ISR (PARP(64)), the multiplicative factor for the evolution of λ_{QCD} with α_S for FSR (PARP(72)) and the the FSR low-p_{T} cutoff parameter (PARP(82)). The variation is derived using a comparison of data and MC prediction for the jet gap fraction — the fraction of events that pass a selection vetoing

Table 7.4: Values of Pythia steering parameters used to derive the uncertainty on the simulation of ISR/FSR for the $t\bar{t}$ sample. The default values are for the AUET2B Pythia tune. The effect of the different parameters is explained in the main text.

Parameter	Less ISR/FSR	Default	More ISR/FSR
PARP(67)	0.7	1.0	1.75
PARP(64)	3.6	0.6	0.6
PARP(72)	0.215	0.43	0.645
PARJ(82)	1.66	0.83	0.5

additional jet activity in the event — in di-lepton $t\bar{t}$ events and of jet shapes in QCD multijet events. In Table 7.4 the used parameter variations are listed.

The relative variation is calculated as

$$\Delta_{\text{rel}} = \frac{|n_{\text{more}} - n_{\text{less}}|}{n_{\text{more}} + n_{\text{less}}}$$

where n_{more} (n_{less}) is the number of events from the distribution with more (less) ISR/FSR. For each bin in $m_{t\bar{t}}$ the resulting uncertainty is

$$n_{\text{Central}} \cdot (1 \pm \Delta_{\text{rel}})$$

Here n_{Central} is the per-bin event count from a MC@NLO $t\bar{t}$ sample. The effect on the $m_{t\bar{t}}$ distribution for the $t\bar{t}$ sample is shown in Figure 7.15b. The ISR/FSR uncertainty leads to an uncertainty on the event yield for the $t\bar{t}$ sample of $-3\,\%$ to $5.5\,\%$. The SM $t\bar{t}$ distribution and the multijet estimate (via $t\bar{t}$ subtraction) are affected by this uncertainty.

7.3.5 Luminosity

The measurement of the luminosity in ATLAS is described in Sec. 4.5. Important contributions to the systematic uncertainty are due to uncertainties on effects that influence the results of the the van-der-Meer scans: correlations between the beam positions in the x-y-plane, variation of the emittance during the scan, changes in the observed cross-section from bunch-to-bunch, dependence on μ and beam-beam effects.

A total uncertainty of $3.9\,\%$ [87] on the integrated luminosity is used. The normalization of $t\bar{t}$ is estimated independently in the limit setting and the multijet background is completely estimated from data. Therefore only the signal yield is affected by this uncertainty.

7.3.6 Higher Order QCD Corrections

The effect of higher order QCD corrections on the $t\bar{t}$ background is estimated similarly to the ISR/FSR uncertainty. Two samples are created using the MC@NLO program. One with each the renormalization and factorization scales both increased and decreased by a factor of 2. The di-top invariant mass distributions for generated top-quarks are compared between the two variations and the central distribution and two per-event weights are calculated by dividing the scale increased (decreased) samples by the central distribution. The resulting weights are presented in Figure 7.16 while the resulting uncertainty on $m_{t\bar{t}}$ for the $t\bar{t}$ sample is shown in Figure 7.15c. The SM $t\bar{t}$ distribution and the multijet estimate (via $t\bar{t}$ subtraction) are affected by this uncertainty.

7.3.7 Parton Shower Model

The uncertainty associated with the modelling of the parton shower is evaluated by using two samples of $t\bar{t}$ events simulated using the POWHEG MC generator interfaced to two different programs for simulating the parton shower: PYTHIA and HERWIG. The differences between these two distributions are symmetrized and taken as the systematic uncertainty. The relative difference is calculated per bin in the di-top invariant mass distribution as:

$$\Delta_{\text{rel}} = \frac{2 \cdot (|n_{\textsc{Herwig}} - n_{\textsc{Pythia}}|)}{n_{\textsc{Herwig}} + n_{\textsc{Pythia}}}$$

where $n_{\textsc{Herwig}}$ ($n_{\textsc{Pythia}}$) is the number of events from the distribution using HERWIG (PYTHIA) for simulating the parton shower. The uncertainty is then derived by moving the central distribution up/down in each $m_{t\bar{t}}$ bin:

$$n_{\text{Central}} \cdot (1 \pm \Delta_{\text{rel}})$$

Here n_{Central} is the event yield for the MC@NLO/HERWIG $m_{t\bar{t}}$ distribution. The resulting uncertainty is presented in Figure 7.15a. The SM $t\bar{t}$ distribution and the multijet estimate (via $t\bar{t}$ subtraction) are affected by this uncertainty.

7.3.8 Higher Order Electroweak Corrections

The shape of the $m_{t\bar{t}}$ distribution for the SM $t\bar{t}$ sample is also affected by higher order electroweak corrections. In Ref. [139] scale factors for the electroweak virtual corrections are given. The factors range from 0.98 for a di-top invariant mass of 400 GeV to 0.90 for a di-top invariant mass of 2000 GeV. Because the total correction (real+virtual) is assumed to be smaller than the virtual-only correction the scale factors are not used to shift the central value but to estimate a one standard deviation systematic uncertainty on the higher order EW corrections. This is done by dividing/multiplying the $m_{t\bar{t}}$ spectrum with the factors given in Table III, Ref. [139]. This uncertainty leads to an uncertainty in the $t\bar{t}$ event yield of $\approx 4\,\%$. The effect on the $m_{t\bar{t}}$ distribution is shown in Figure 7.15d for for the $t\bar{t}$ sample. The SM $t\bar{t}$ distribution and the multijet estimate (via $t\bar{t}$ subtraction) are affected by this uncertainty.

7.3.9 $t\bar{t}$ Normalization

The effects of different systematic uncertainties on the expected event yield for the SM $t\bar{t}$ background as well as two hypothetical signal samples are listed in Table 7.5. Adding the different contributions in quadrature — including an additonal uncertainty of $\approx 10\,\%$ on the $t\bar{t}$ normalization as was derived by measuring the normalization in a data-control region (Sec. 7.2) — leads to a total uncertainty on the event yield of $\approx 30\,\%$ for the SM $t\bar{t}$ background.

As will be explained in more detail in Sec. 7.4, all uncertainties (except the $t\bar{t}$ normalization) are assumed to only affect the shape (instead of shape and event yield) of the SM $t\bar{t}$ distribution to avoid over-constraining the nuisance parameters in the limit setting. An a-priori normalization uncertainty of $^{+100\%}_{-50\%}$ is assumed. This a-priori uncertainty is chosen to be larger than the expected total uncertainty so it can be constrained to the real value in the limit-setting procedure. The final uncertainty on the normalization of the SM $t\bar{t}$ background, as estimated in the limit-setting step, is $\approx 30\,\%$. The SM $t\bar{t}$ distribution and the multijet estimate (via $t\bar{t}$ subtraction) are affected by this uncertainty.

7.3.10 Multijet Background Estimates

The data-based estimation of the multijet background is outlined in Sec. 7.2. As the subtraction of the SM $t\bar{t}$ background is a part of this estimation procedure, all systematic uncertainties on the $t\bar{t}$ prediction are propagated to the multijet estimate.

An additional uncertainty on the multijet distribution is due to the used method for estimating this background. The difference between the predictions from regions A-B-E and C-D-E is taken as an uncertainty. The resulting uncertainty on the multijet event yield is $\pm 14\,\%$ and the effect on the $m_{t\bar{t}}$ distribution is presented in Fig. 7.17. It is larger than all uncertainties propagated from the $t\bar{t}$ MC sample.

7.3.11 Trigger Efficiency

To guarantee a sufficiently large number of events even at low $m_{t\bar{t}}$, the trigger is also used in the turn-on region. For simulated events the trigger decision in MC is utilized. The trigger efficiency for data and MC is shown in Fig. 7.18a for the first part of the data taking period and in Fig. 7.18b for the second part. The efficiencies for the two time periods are displayed separately because the threshold for $\sum E_{\mathrm{T}}$ used for the combined single-jet and $\sum E_{\mathrm{T}}$-trigger was $\sum E_{\mathrm{T}} > 350$ GeV for the first and $\sum E_{\mathrm{T}} > 400$ GeV for the second period.

Also shown is the effect of shifting the JES for the MC simulated events. Within the uncertainty on the JES the distribution in data is well modelled by MC. For top quarks from a signal sample the efficiency is presented in Fig. 7.18c and Fig. 7.18d. The triggers are fully efficient at the plateau. No uncertainty due to the simulation of the trigger is included.

7.3.12 Color Structure

The color structure of the new resonance (singlet or octet) can affect the efficiency with which top quarks are identified [140] by the HEPTopTagger method. The sensitivity for a KK photon and KK gluon of same mass and width will differ by $\approx 10\,\%$. No uncertainty due to this effect is assumed, but the results are only valid for the stated color structures: the color-singlet Z' boson and the color-octet KK gluon.

Table 7.5: Estimated relative change in event yield due to systematic uncertainties for the $t\bar{t}$, $Z'(m = 1.3$ TeV) and KK gluon ($m = 1.15$ TeV) samples. The numbers for the $t\bar{t}$ sample are only included for comparison, in the limit setting a total uncertainty on the yield is used and the other uncertainties are only taken to influence the shape of the $t\bar{t}$ distribution.

uncertainty	$t\bar{t}$	$m_{Z'} = 1.3$ TeV	$m_{g_{KK}} = 1.15$ TeV
b-tagging (true b-jets)	$^{+18.8\%}_{-17.2\%}$	$^{+24.5\%}_{-21.9\%}$	$^{+25.2\%}_{-22.5\%}$
b-tagging (true c-jets)	$\pm 1.1\%$	$^{1.1\%}_{-1.0\%}$	$^{+0.5\%}_{-0.3\%}$
b-tagging (true light-jets)	$^{+0.9\%}_{-0.8\%}$	$^{+0.7\%}_{-0.6\%}$	$^{+2.8\%}_{-1.6\%}$
luminosity	$\pm 3.9\%$	$\pm 3.9\%$	$\pm 3.9\%$
JES uncertainty for a subjet p_{T} of:			
< 50 GeV	$^{+4.1\%}_{-3.2\%}$	$^{+2.5\%}_{-2.9\%}$	$^{-0.3\%}_{-1.1\%}$
$50 - 150$ GeV	$^{+6.7\%}_{-8.2\%}$	$^{+4.3\%}_{-4.7\%}$	$^{+3.6\%}_{-4.3\%}$
$150 - 300$ GeV	$^{+0.0\%}_{-0.7\%}$	$^{+0.8\%}_{-1.2\%}$	$^{-1.3\%}_{-1.4\%}$
$300 - 500$ GeV	$^{+0.4\%}_{-0.2\%}$	$^{+0.2\%}_{-0.7\%}$	$^{+0.1\%}_{-1.3\%}$
subjet energy resolution	$^{+0.7\%}_{1.8\%}$	$\pm 3.2\%$	$\pm 8.1\%$
PDF	$\pm 3.0\%$	$\pm 1.3\%$	$\pm 1.9\%$
$t\bar{t}$ higher-order EW corrections	$^{+4.3\%}_{-4.1\%}$	-	-
$t\bar{t}$ higher-order QCD corrections	$^{+12.3\%}_{-7.5\%}$	-	-
$t\bar{t}$ ISR/FSR	$^{+5.5\%}_{-3.0\%}$	-	-
$t\bar{t}$ parton shower modelling	$^{+4.6\%}_{-2.1\%}$	-	-

7.3.13 Summary

The changes to the event yield for the SM $t\bar{t}$ sample, a Z' ($m = 1.3$ TeV) signal and a KK gluon ($m = 1.15$ TeV) sample due to different systematic uncertainties are listed in Table 7.5. The following uncertainties are only estimated for the $t\bar{t}$ sample: higher order EW corrections, higher order QCD corrections, ISR/FSR and parton shower modelling. The largest change for all samples is due to the uncertainty on the tagging-efficiency for true b-jets. Changes in the expected yields for the multijet sample are not included in the table because these are small for all uncertainties except the uncertainty on the multijet background estimate which leads to a change of $\pm 14\,\%$ on the event yield.

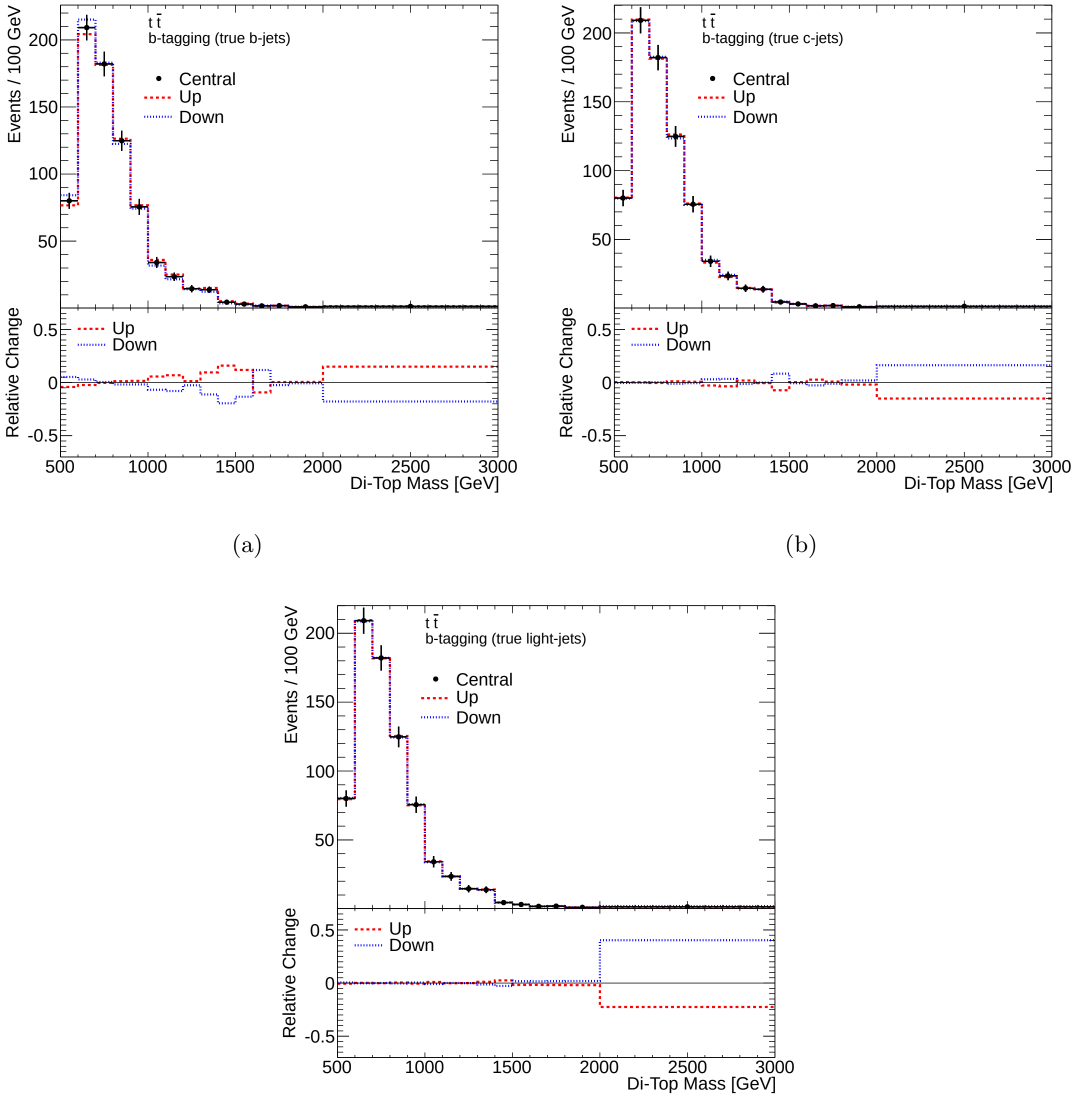

(a)

(b)

(c)

Figure 7.11: Effect of the uncertainty on tagging efficiency and inefficiency for (a) b-jets, (b) c-jets and (c) light jets on the $m_{t\bar{t}}$ distribution for the $t\bar{t}$ sample. In the top section of each figure the $m_{t\bar{t}}$ distributions corrseponding to an integrated luminosity of $4.7\,\mathrm{fb}^{-1}$ are shown. The nominal distribution (without changes due to systematic uncertainties) is labelled *Central*. Also included are distributions corresponding to a 1-σ upwards (*Up*) and downwards (*Down*) variation of the systematic uncertainty. In the bottom section the relative differences $\frac{\mathrm{Up}-\mathrm{Central}}{\mathrm{Central}}$ (labelled *Up*) and $\frac{\mathrm{Down}-\mathrm{Central}}{\mathrm{Central}}$ (labelled *Down*) are shown.

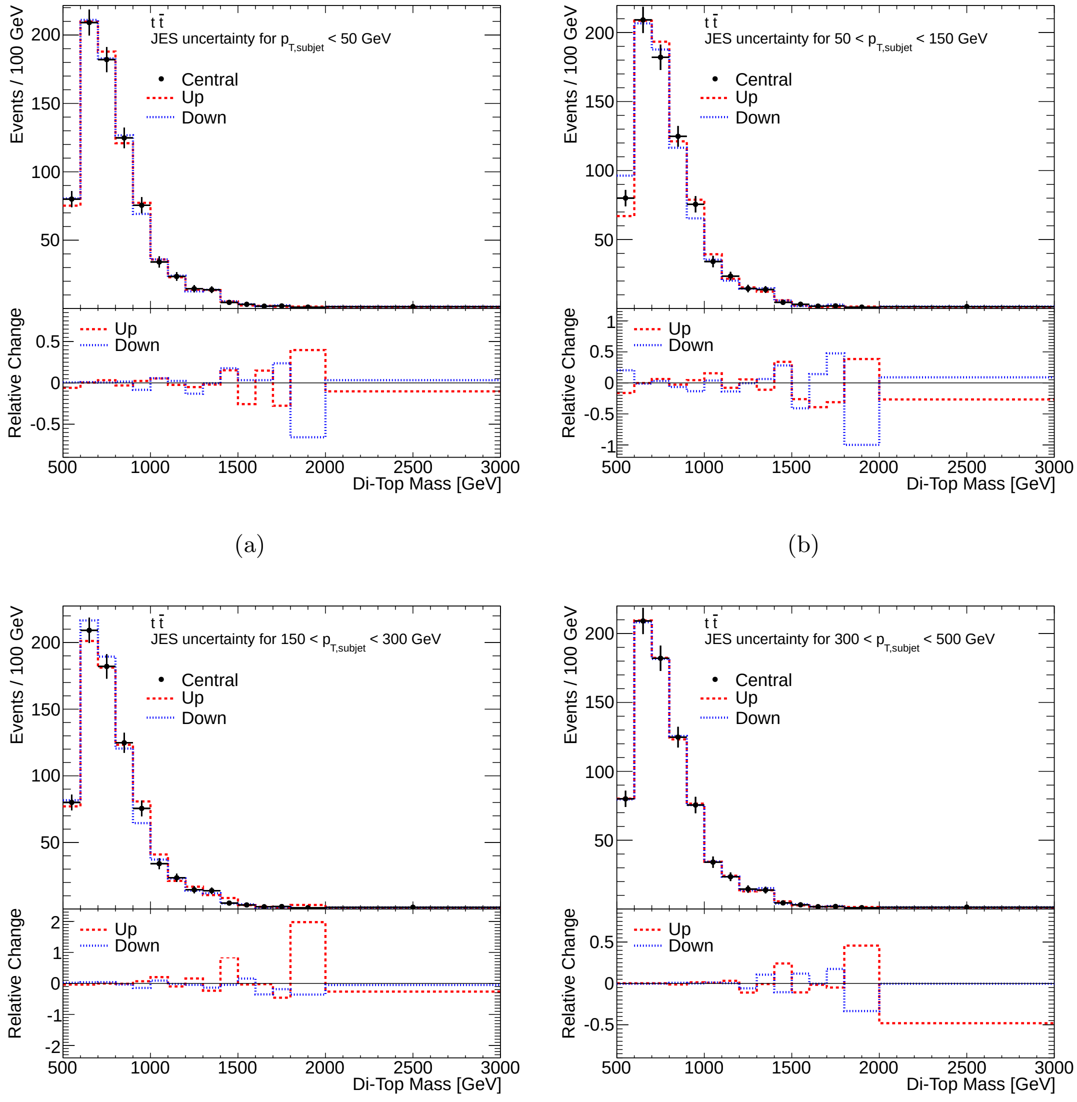

(a)

(b)

(c)

(d)

Figure 7.12: Effect of the uncertainty on the subjet energy scale for (a) $p_{\mathrm{T}} <$ 50 GeV, (b) $50 < p_{\mathrm{T}} < 150$ GeV, (c) $150 < p_{\mathrm{T}} < 300$ GeV and (d) $300 < p_{\mathrm{T}} < 500$ GeV on the $m_{t\bar{t}}$ distribution for the $t\bar{t}$ sample. The distributions are explained in detail in the caption of Fig. 7.11.

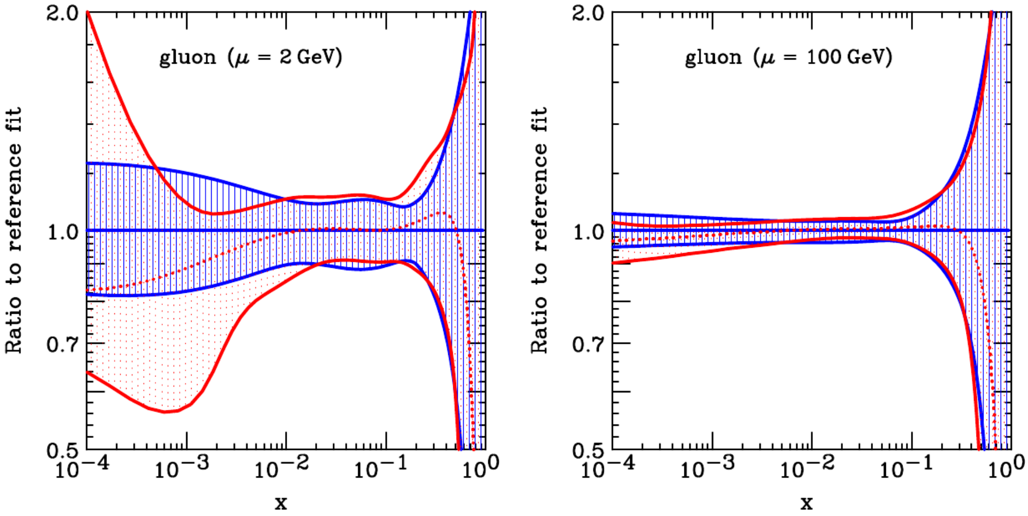

Figure 7.13: Ratio of the CT10 gluon-PDF (in red) to the previous CTEQ6.6 [37] best-fit result (in blue) as function of Bjorken x. The colored bands indicate the uncertainties on the ratios. The left (right) figure shows the PDFs for a scale of $\mu = 2$ GeV ($\mu = 100$ GeV) [108].

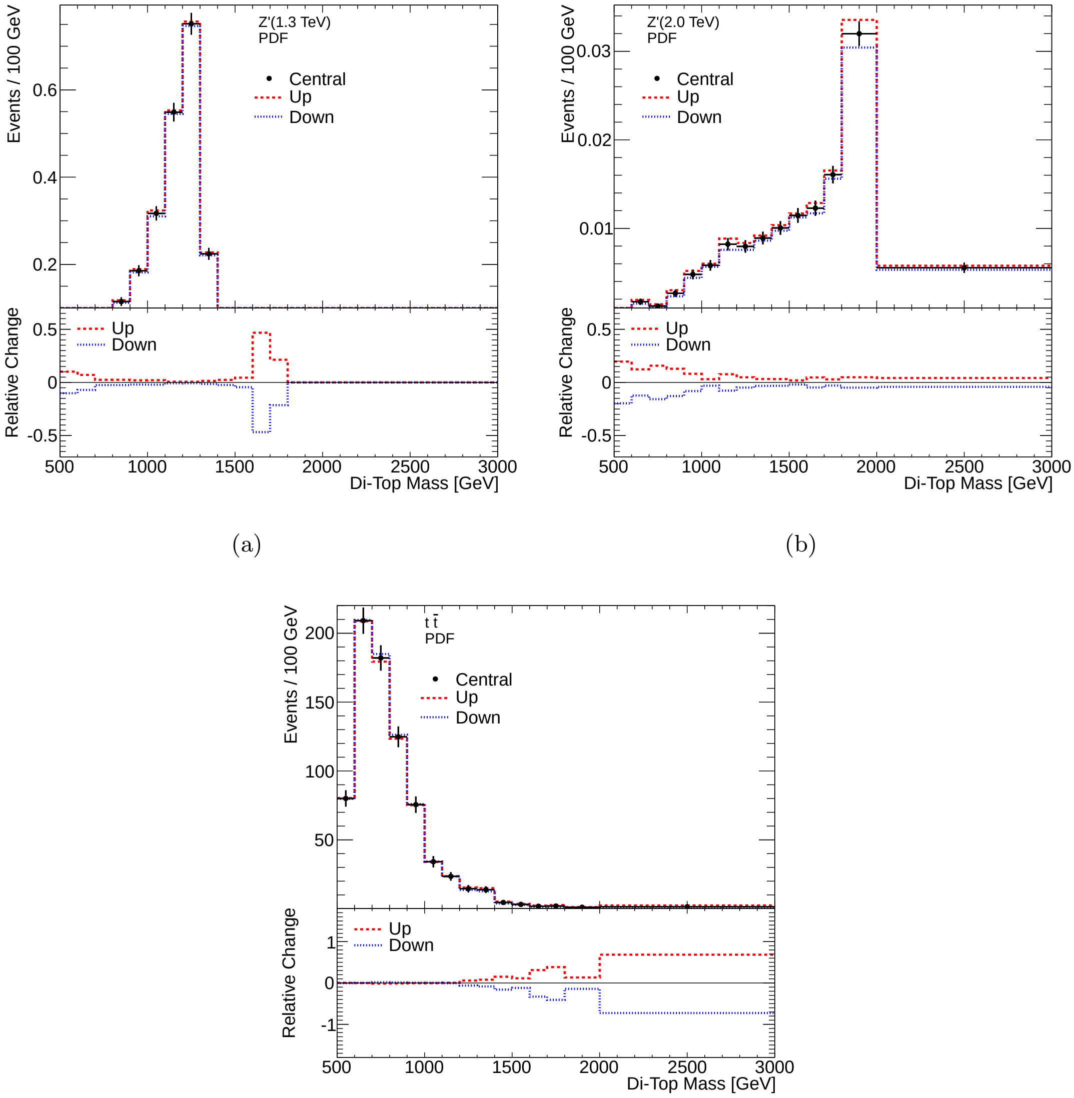

(a)

(b)

(c)

Figure 7.14: Effect of the PDF uncertainty on the $m_{t\bar{t}}$ distribution for (a) a Z' ($m = 1.3$ TeV) signal, (b) a Z' ($m = 2.0$ TeV) signal and (c) the SM $t\bar{t}$ sample. The distributions are explained in detail in the caption of Fig. 7.11.

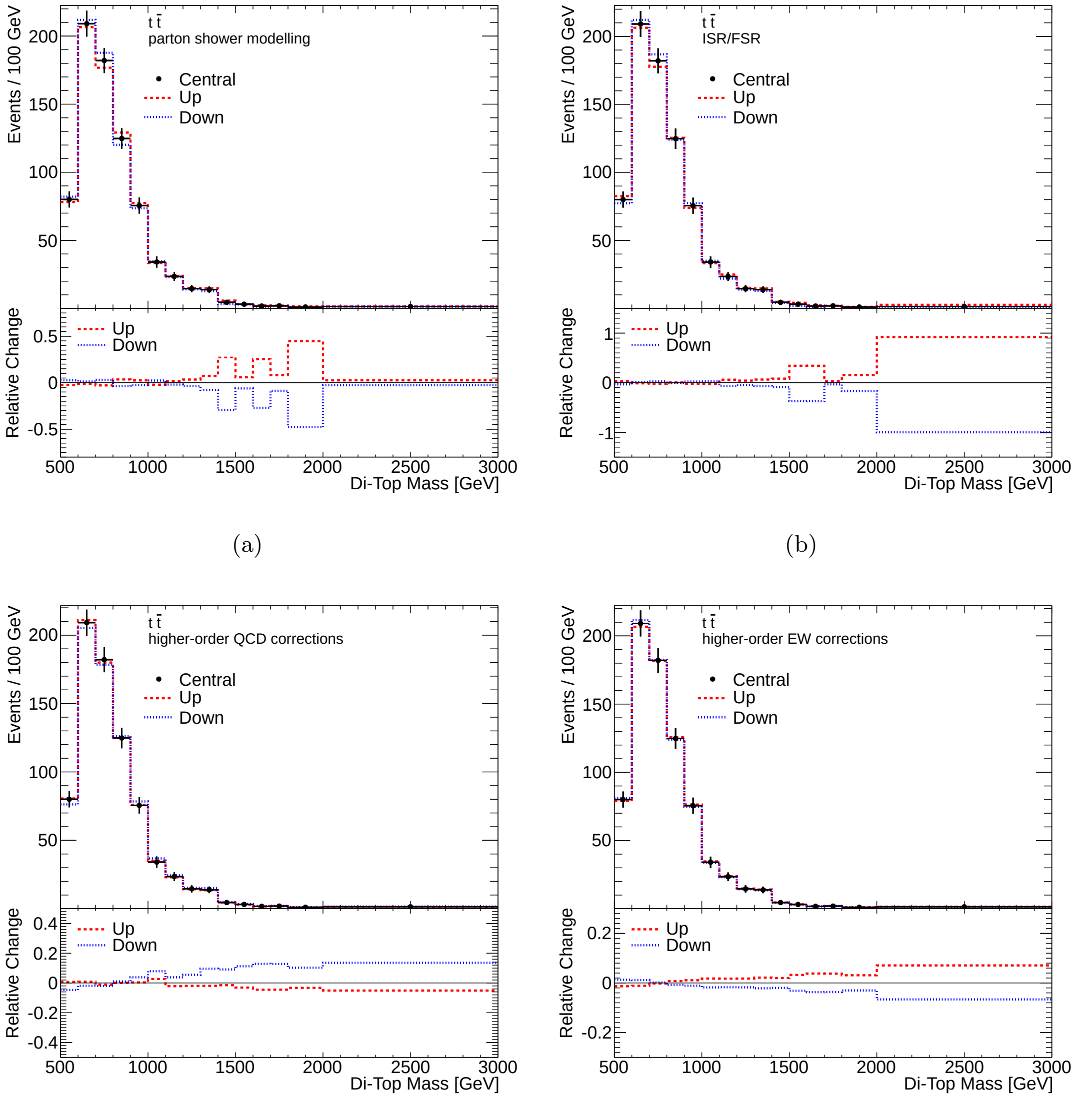

(a) (b)

(c) (d)

Figure 7.15: Effect of the uncertainty on (a) parton shower modelling, (b) ISR/FSR conditions, (c) higher order QCD corrections and (d) higher order electroweak corrections on the $m_{t\bar{t}}$ distribution for the $t\bar{t}$ sample. The distributions are explained in detail in the caption of Fig. 7.11.

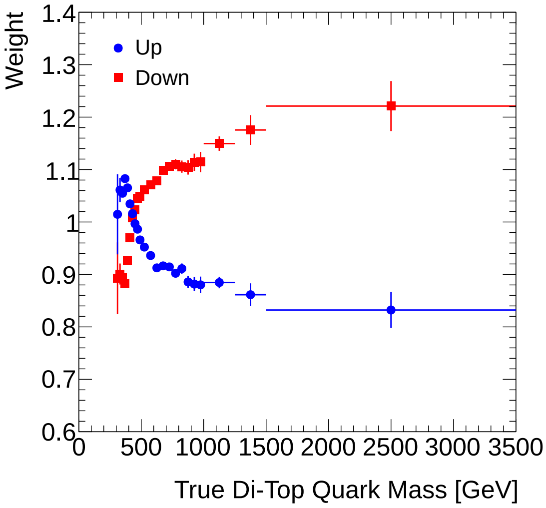

(a)

Figure 7.16: Per-event weight due to uncertainties on higher order QCD corrections as a function of truth-level $m_{t\bar{t}}$ estimated for the SM $t\bar{t}$ sample.

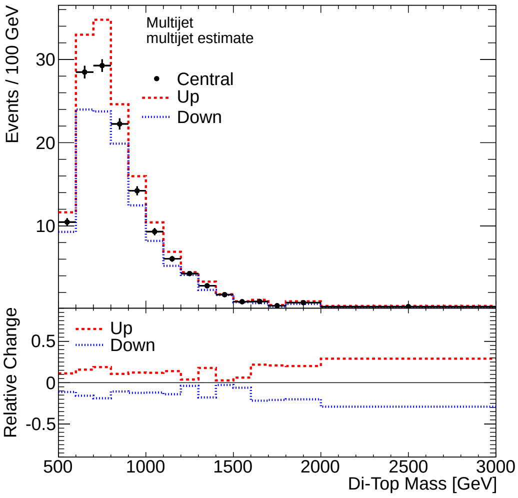

Figure 7.17: Uncertainty on the $m_{t\bar{t}}$ distribution for the multijet background due to the multijet background estimation method. The distributions are explained in detail in the caption of Fig. 7.11.

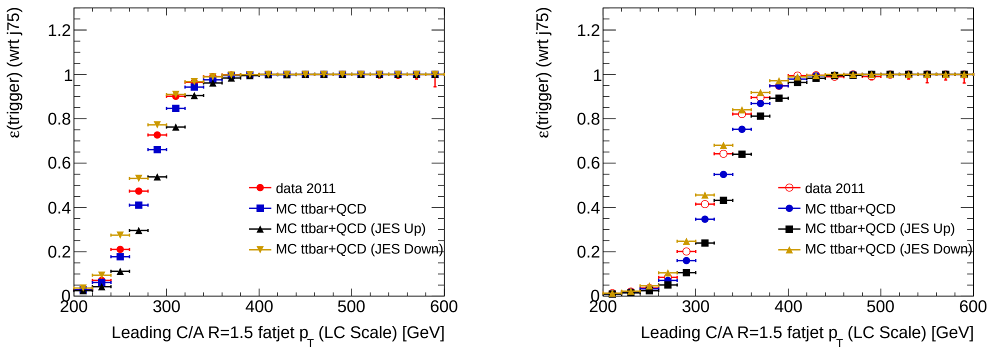

(a) ≤ Period J (b) > Period J

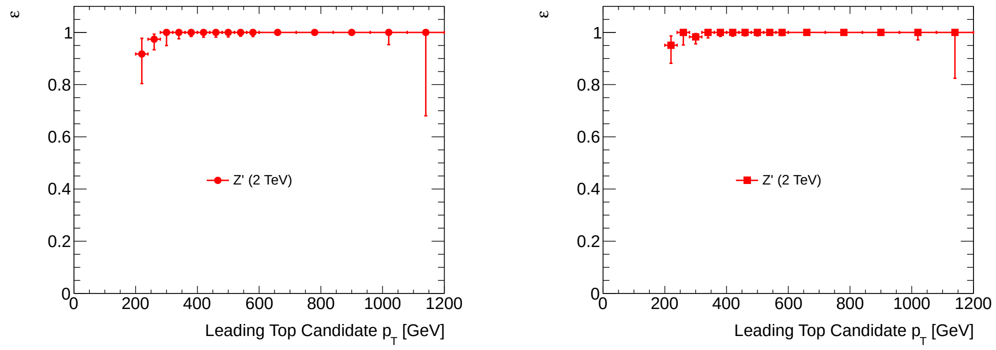

(c) ≤ Period J (d) > Period J

Figure 7.18: Trigger efficiency for the (a) first part and (b) second part of data taking during 2011 as a function of the p_{T} of the leading fat jet in the event. The efficiency is measured with respect to the fully efficient trigger requiring one anti-k_t(R=0.4) jet with $p_{\mathrm{T}} > 75$ GeV. The simulated distributions are shifted by the JES. The trigger efficiency for the (c) first part and (d) second part of data taking as function of the p_{T} of the leading, reconstructed top-quark candidate p_{T} for simulated events from the 2 TeV Z' sample after applying the full analysis selection.

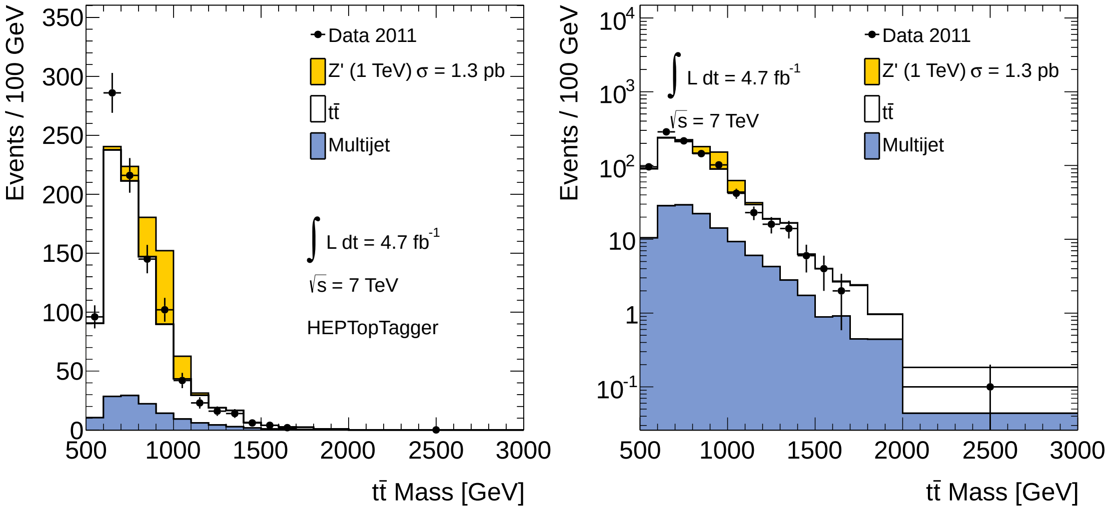

(a) (b)

Figure 7.19: Distributions of $m_{t\bar{t}}$ in the signal region on (a) a linear scale and (b) a logarithmic scale. Superimposed are the SM $t\bar{t}$ and multijet background predictions as well as a hypothetical Z' signal with $m_{Z'} = 1$ TeV. The vertical bars represent the statistical uncertainty of the data events.

7.4 Results

In Sec. 7.2 the $t\bar{t}$ background in the signal region was estimated to 770^{+220}_{-180} events and the multijet background to 130 ± 70 (stat.+syst.) events. A total of 953 events are observed in data.

The $m_{t\bar{t}}$ distribution for data and the predicted backgrounds is presented in Fig. 7.19. A hypothetical Z' signal with a mass of 1 TeV is shown for illustration. There is no significant excess over the SM $t\bar{t}$ and multijet background estimations at any mass value.

In the absence of a signal, a Bayesian approach is used to set upper limits at 95% confidence level on the production cross section times branching ratio to $t\bar{t}$ final states for Z' and KK gluon models. This method is explained in detail in Sec. 2.6.

Limits are calculated for resonance masses between 0.5 and 2.0 TeV for the Z' boson model and between 0.7 and 2.0 TeV for the KK gluon model. The systematic uncertainties are included as nuisance parameters and Gaussian distributions with widths determined as described in Sec. 2.6 are used as prior probability distributions. These nuisance parameters are then marginalized to derive confidence intervals.

The large a-priory uncertainty on the $t\bar{t}$ normalization avoids over-constraining other nuisance parameters which are sensitive to the normalization. This procedure corresponds to a measurement of the normalization of the SM $t\bar{t}$ background in data using the bins in $m_{t\bar{t}}$ where no signal is expected. Using five uncorrelated regions in jet p_{T} for the JES uncertainty avoids that regions with low $m_{t\bar{t}}$, where high event yields result in small statistical uncertainties, constrain regions with high $m_{t\bar{t}}$. As will be shown in the following, the nuisance parameters corresponding to the $t\bar{t}$ normalization and the subjet-JES uncertainties are indeed constrained but due to the separation by regions in subjet p_{T} no cross-constraining occurs.

The sensitivity of this search is estimated by using O(100) pseudo-experiments for each mass-point. The distributions are drawn from the background-only predictions and all nuisance parameters are allowed to fluctuate in a way that is consistent with their respective prior distributions.

The expected limit is defined as the median of the ensemble of predictions. The 68% and 95% confidence level envelope of limits are similarly defined utilizing the width of the distribution of limits for each resonance mass.

The exclusion limits at 95% C.L. on the cross section times branching ratio for the two models are presented in Fig. 7.20. By comparing the measured cross-section limits to theoretical cross section calculations for benchmark models, these can be interpreted as mass limits.

For the calculation of the Z' boson model cross-section the PYTHIA v6.421 MC generator is used. The result is then multiplied with an additional k-factor of 1.3 to account for next-to-leading order (NLO, described in Sec. 4.8) effects [112]. Kaluza-Klein Gluons are predicted by the bulk Randall-Sundrum model (RS) [24–26] and the cross-section is calculated with the PYTHIA v8.1 MC [141] generator. In Table 7.6 the expected and observed mass limits are shown. The analysis is able to exclude Z' boson resonances over parts of the mass range between 0.70 and 1.32 TeV and KK gluons with masses between 0.70 and 1.48 TeV.

To assess which systematic uncertainties have the strongest effect on the limits, the nuisance parameter corresponding to an uncertainty is removed, and the limit-setting procedure is re-run. Table 7.7 shows the expected limit on $\sigma \times BR$ for one KK gluon and Z' mass point. Also listed is the relative improvement due to excluding selected, single systematic uncertainties as well as the expected limit derived without any nuisance parameters corresponding to systematic uncertainties (stat. only). The systematic uncertainty on the b-tagging efficiency clearly dominates the limits. This uncertainty — as shown in Table 7.5 — also has the largest effect on the event yield, leading to a change of up to $\approx 25\,\%$ for the signal samples. The total change in the limit with and without systematic uncertainties included is sligthly above $50\,\%$ for both the KK gluon and Z' sample.

The expected posterior distributions for two different signal masses are presented in Fig. 7.21. A set of random numbers, following a Gaussian distribution with a mean of 0 and an RMS of 1, are generated. The expected posteriors are calculated by weighting the distributions by the integral of all systematic likelihoods by using the sum-of-backgrounds as pseudo-data. The horizontal lines in Fig. 7.21 are used to indicate the mean of the weighted distributions and the vertical band indicates the RMS. For most of the systematic uncertainties the mean is close to 0 and the RMS is 1, indicating that the modelling is consistent. The RMS of the uncertainty on the normalization of $t\bar{t}$ is much smaller than one. This means that the nuisance parameter, corresponding to the $t\bar{t}$ normalization is strongly constrained with respect to the initial assumption, as was intended. The resulting, total, uncertainty on the $t\bar{t}$ normalization is $\approx 30\,\%$. The nuisance parameters for the subjet-JES are also constrained.

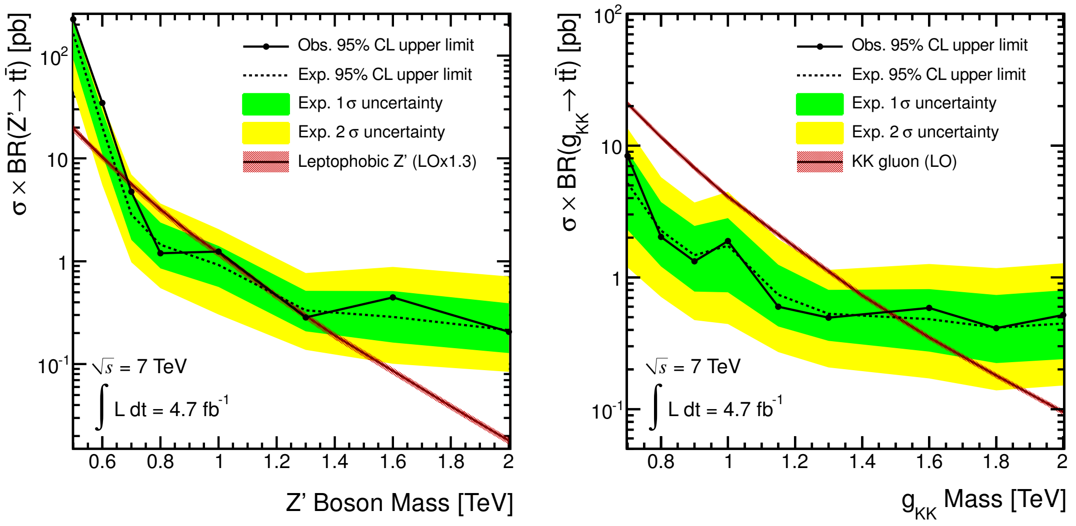

(a) (b)

Figure 7.20: Upper limits at 95% C.L. on the production cross section times branching fraction $\sigma \times BR$ as a function of the resonance mass for (a) Z' boson and (b) KK gluon models. The expected and observed limits are shown. The model predictions and uncertainties are represented by the red bands. The theoretical cross-section prediction for Z' bosons is made at NLO (using a k-factor of 1.3) and at LO for KK gluons.

Table 7.6: Exclusion regions on the mass of new resonances for leptophobic Z' bosons and RS KK gluons.

Model	Obs. Limit (TeV)	Exp. Limit (TeV)
Z'	$0.70 < m_{Z'} < 1.00$	$0.68 < m_{Z'} < 1.16$
	$1.28 < m_{Z'} < 1.32$	
KK gluon	$0.70 < m_{g_{KK}} < 1.48$	$0.70 < m_{g_{KK}} < 1.52$

Recalculating the limit for KK gluon signals with masses of 0.9 GeV, 1 TeV and 1.15 TeV excluding individual systematic uncertainties shows that the kink in the KK gluon limit distribution — Fig. 7.20 b — at 1 TeV is caused by the subjet-JES. The subjet-JES is treated as independent between different regions in jet p_{T}. Therefore the limits are also recalculated without the uncertainty on individual regions in subjet p_{T} to make sure the bump is not due to a region (or a pair of regions) alone. Table 7.8 shows that the limit for the 1 TeV KK gluon sample is affected more strongly by each of the subjet-JES uncertainties than its neighbours leading to the observed bump in the limit distribution.

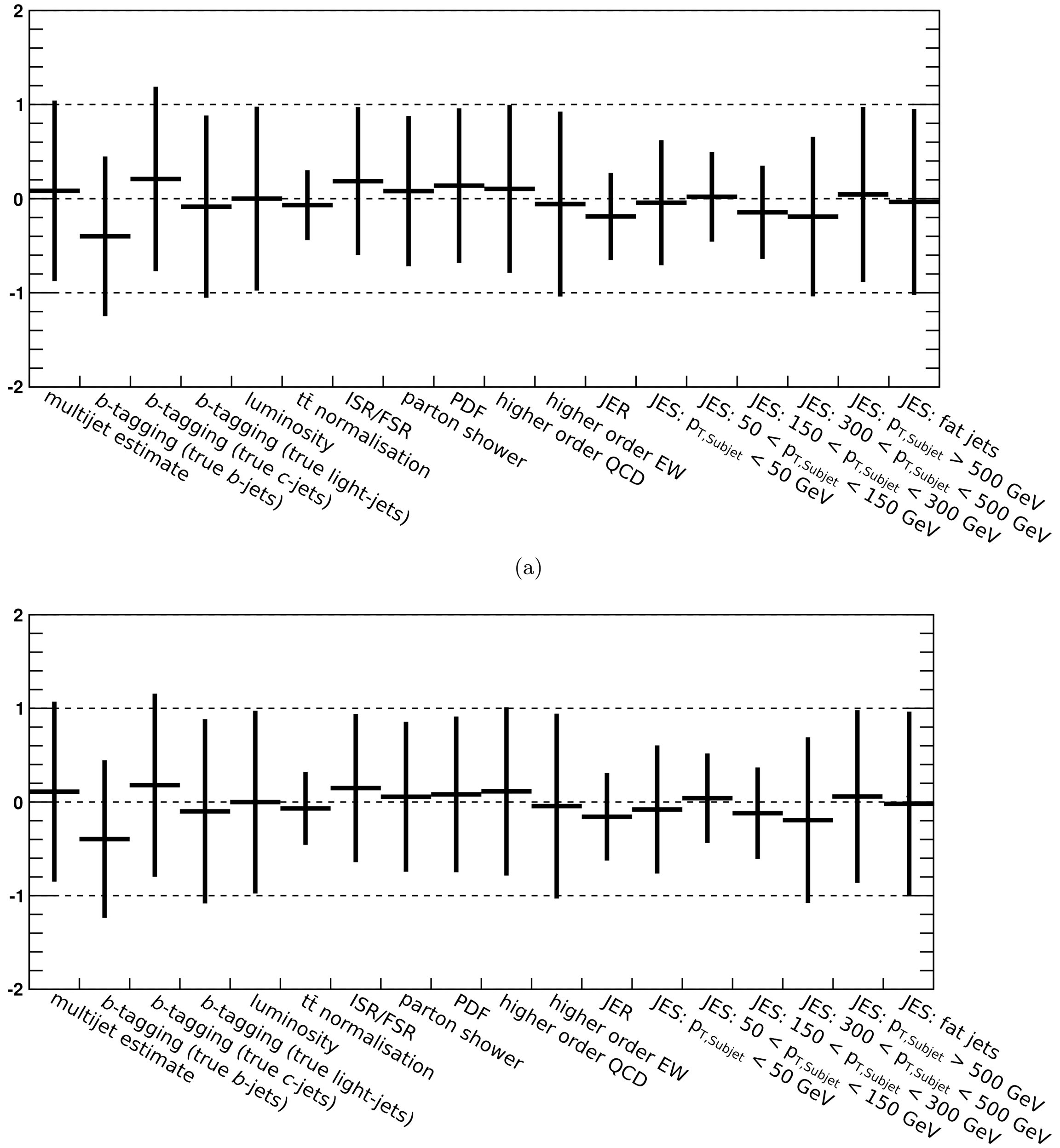

(a)

(b)

Figure 7.21: Summary of expected posterior distribution of the systemtaic uncertainties for (top) a hypothetical 1.15 TeV KK gluon and (bottom) a 1.3 TeV Z' signal. The positions of the horizontal (lengths of the vertical) lines indicate the mean (RMS) of the posterior distributions for each systematic uncertainty.

Table 7.7: Expected limit on $\sigma \times BR$ for a hypothetical 1.15 TeV KK gluon and a 1.3 TeV Z' signal. To assess the effect of different systematic uncertainties the relative improvement when individual systematic uncertainties are not included in the estimation of the expected limit is shown. The relative improvement is calculated as the difference of the two limits divided by the default expected limit. The signs are chosen so that a positive relative change corresponds to a smaller (*better*) number for the expected limit. Only the three dominant uncertainties for each sample are listed. The relative improvement when calculating the limit without systematic uncertainties (statistical unertainty only) is also presented.

	$m_{g_{KK}} = 1.15$ TeV	$m_{Z'} = 1.3$ TeV
expected limit	0.77 pb	0.33 pb
rel. change (without b-tagging unc.)	37 %	24 %
rel. change (without JES unc.)	17 %	2 %
rel. change (without parton-shower unc.)	4 %	0.5 %
rel. change (without PDF unc.)	1 %	3 %
rel. change (stat. only)	45 %	44 %

Table 7.8: Relative improvement of the cross section limit (in %) for three different KK gluon mass points when calculating the limit excluding the subjet-JES uncertainty for different ranges of the subjet p_{T}.

Subjet p_{T}[GeV]	$m_{g_{KK}} = 0.9$ TeV	$m_{g_{KK}} = 1$ TeV	$m_{g_{KK}} = 1.15$ TeV
$p_{\mathrm{T}} < 50$	0.04	0.10	0.02
$50 < p_{\mathrm{T}} < 150$	0.08	0.13	0.05
$150 < p_{\mathrm{T}} < 300$	0.06	0.15	0.11
$300 < p_{\mathrm{T}}$	0.00	0.03	0.02

Chapter 8

Conclusions and Outlook

In this thesis the first study of the HEPTopTagger algorithm using collision data is presented. By selecting isolated muons and missing transverse energy an event sample, enriched in lepton+jets $t\bar{t}$ final states is created. The HEPTopTagger method is tested on this sample and all distributions indicate that the HEPTopTagger algorithms efficiently identifies top quarks and is robust against effects of pile-up. The data is well modelled by predictions from MC simulations.

A search for new resonances, Z' bosons or KK gluons, decaying into the fully hadronic $t\bar{t}$ final state that uses the 2011 LHC pp collision data at a center-of-mass energy of 7 TeV, recorded by the ATLAS detector and corresponding to an integrated luminosity of $4.7\,\mathrm{fb}^{-1}$ is shown. Using the HEPTopTagger algorithms events with two hadronically decaying top quarks are identified. These top-quarks are boosted and have a transverse momentum between 200 GeV and approximately 1 TeV.

The $m_{t\bar{t}}$ spectrum is reconstructed from the top-quark four-momenta and compared to predictions for SM $t\bar{t}$ and multijet production. The observed spectrum is compatible with SM predictions. Models for Z' bosons with masses $0.70 < m_{Z'} < 1.00$ TeV and $1.28 < m_{Z'} < 1.32$ TeV, and KK gluons with masses $0.70 < m_{g_{KK}} < 1.48$ TeV, are excluded at 95% C.L.

The results of this search are published in Ref. [23] together with a complementary analysis, using the Top Templating method [142, 143] for the identification of hadronically decaying top quarks. This second technique improves the measured limit for KK gluon production to 1.62 TeV while providing weaker limits at lower mass values. The limits obtained in the fully-hadronic final state limits are compatible with results in the lepton+jets channel where the ATLAS Collaboration [127, 128] excluded Z' bosons (KK gluons) with masses between 0.50 and 1.15 TeV (0.5 and 1.5 TeV).

As this analysis was the first use of an advanced, substructure-based, top-quark reconstruction technique in a search for new physics, many improvements are possible. In addition to reduced statistical uncertainties due to larger event numbers, the performance at higher top-quark p_{T} can be improved by optimizing the parameters of the HEPTopTagger or the distance parameter used for reconstructing the initial fat jet as a function of the fat jet p_{T}. As the signal-to-background ratio for events with two highly boosted, tagged, top-quarks is large, efficiency gains by weakening the b-tagging requirements — either by choosing a more efficient b-tagging configuration or requiring fewer tags — for such events are possible. Searches for signals with masses at and above

≈ 1.6 TeV will also benefit from reductions on the uncertainty on the parton distribution functions due to measurements at the LHC.

The improved understanding in substructure reconstruction can also be used for other analyses such a searches for supersymmetric partners of the top quark [21] or a measurement of the coupling between top-quarks and the Higgs boson [20].

Acknowledgments

For the help and support I received by many individuals over the past three years I am truly grateful – without it, the completion of this thesis would not have been possible.

I would like to thank Prof. Dr. André Schöning, my thesis adviser, for sharing his guiding wisdom and clear vision with me. Dr. Sebastian Schätzel helped me to turn ideas into concrete results and took on the task of calibrating and determining the uncertainty of substructure objects used in this thesis.

My warm thanks go to Dr. Christoph Anders and Sebastian Schmitt who shared office with me during the critical stages of this work and were always willing to exchange ideas. I am thankful to the current and former members of our group in Heidelberg, especially Rohin Narayan, David Sosa, Maddalena Giulini and Dr. Tatsiana Klimkovich, for many fruitful discussions over the last months and years. I was always able to rely on the great experience and perspective on critical issues of Dr. Niklaus Berger and Dr. Dirk Wiedner.

I am very happy for the opportunity to collaborate with outstanding theorists and would like to thank Prof. Dr. Tilman Plehn, Dr. Michael Spannowsky and Dr. Michihisa Takeuchi for supporting the use of their algorithm and providing deep insights into the theory of jet substructure and searches at the LHC.

Being part of the ATLAS collaboration was a great experience and I am truly thankful for meeting many friends and colleagues in this exceptional endeavor. Special thanks go to Prof. Dr. Beate Heinemann who served as the head of our Editorial Board and her strong support was essential in publishing the fully hadronic resonance search paper. Prof. Dr. Lucia Masetti and Dr. Weina Ji provided important help in understanding statistical issues related to the analysis. I would like to thank Prof. Dr. Pekka Sinervo and his group for the fruitful collaboration as well as the ATLAS substructure group, especially Dr. David Miller, for providing a stimulating environment in which new techniques could be discussed. For introducing me to the details of the jet trigger, I would like to thank Dr. Michael Begel and Dr. Mario Campanelli as well as Dr. Mark Sutton who also worked tirelessly with me on the performance study.

My final thanks go to my friends and family for their immeasurable support over the years. I am deeply thankful to my parents who always encouraged and enabled me to follow my ideas and to my girlfriend Gizem Yildirim who patiently shares my life.

Bibliography

The bibliography is sorted in citation order.

[1] Steven Weinberg "A Model of Leptons" in: *Phys. Rev. Lett.* 19 (21 Nov. 1967) DOI: `10.1103/PhysRevLett.19.1264` (cited on pages 9, 13).

[2] S.L. Glashow "Partial Symmetries of Weak Interactions" in: *Nucl. Phys.* 22 (1961), pp. 579–588 DOI: `10.1016/0029-5582(61)90469-2` (cited on pages 9, 13).

[3] A. Salam "Elementary Particle Theory: Proceedings of the Eighth Nobel Symposium. Edited by Nils Svartholm." Almqvist & Wiksell, 1968 (cited on pages 9, 13).

[4] S. L. Glashow, J. Iliopoulos, and L. Maiani "Weak Interactions with Lepton-Hadron Symmetry" in: *Phys. Rev. D* 2 (7 Oct. 1970), pp. 1285–1292 DOI: `10.1103/PhysRevD.2.1285` (cited on pages 9, 13).

[5] Peter W. Higgs "Broken Symmetries and the Masses of Gauge Bosons" in: *Phys. Rev. Lett.* 13 (16 Oct. 1964), pp. 508–509 DOI: `10.1103/PhysRevLett.13.508` (cited on pages 9, 13).

[6] F. Englert and R. Brout "Broken Symmetry and the Mass of Gauge Vector Mesons" in: *Phys. Rev. Lett.* 13 (9 Aug. 1964), pp. 321–323 DOI: `10.1103/PhysRevLett.13.321` (cited on pages 9, 13).

[7] G. S. Guralnik, C. R. Hagen, and T. W. B. Kibble "Global Conservation Laws and Massless Particles" in: *Phys. Rev. Lett.* 13 (20 Nov. 1964), pp. 585–587 DOI: `10.1103/PhysRevLett.13.585` (cited on pages 9, 13).

[8] ATLAS Collaboration "Observation of a new particle in the search for the Standard Model Higgs boson with the ATLAS detector at the LHC" in: *Phys. Lett. B* 716.1 (2012), pp. 1–29 DOI: `10.1016/j.physletb.2012.08.020` (cited on pages 9, 21, 44).

[9] CMS Collaboration "Observation of a new boson at a mass of 125 GeV with the CMS experiment at the LHC" in: *Phys. Lett. B* 716.1 (2012), pp. 30–61 DOI: `10.1016/j.physletb.2012.08.021` (cited on pages 9, 21, 44).

[10] K. Kodama et al. “Observation of tau neutrino interactions” in: *Phys. Lett. B* 504.3 (2001), pp. 218–224 DOI: `10.1016/S0370-2693(01)00307-0` (cited on page 9).

[11] CDF Collaboration “Observation of Top Quark Production in $\overline{p}p$ Collisions with the Collider Detector at Fermilab” in: *Phys. Rev. Lett.* 74 (14 Apr. 1995), pp. 2626–2631 DOI: `10.1103/PhysRevLett.74.2626` (cited on page 9).

[12] D0 Collaboration “Search for High Mass Top Quark Production in $p\overline{p}$ Collisions at $\sqrt{s} =$ 1.8 TeV” in: *Phys. Rev. Lett.* 74 (13 Mar. 1995), pp. 2422–2426 DOI: `10.1103/PhysRevLett.74.2422` (cited on page 9).

[13] LEP Electroweak Working Group “Precision electroweak measurements on the Z resonance” in: *Phys. Rept.* 427 (2006), pp. 257–454 DOI: `10.1016/j.physrep.2005.12.006` arXiv:`hep-ex/0509008 [hep-ex]` (cited on pages 9, 44).

[14] LEP Electroweak Working Group “Precision Electroweak Measurements and Constraints on the Standard Model” 2007 arXiv:`0712.0929 [hep-ex]` (cited on pages 9, 44).

[15] J. Beringer and others (Particle Data Group) “The Review of Particle Physics” in: *Phys. Rev. D* 86 (2012) (cited on pages 10, 15, 17, 22–24, 26, 27, 38, 41, 102).

[16] L Evans and P Bryant “LHC Machine” in: *JINST* 3 (2008), S08001 (cited on pages 10, 44, 51).

[17] ATLAS Collaboration “ATLAS Experiment at the CERN Large Hadron Collider” in: *JINST* 3 (2008), S08003 (cited on pages 10, 44, 51, 58–60, 73).

[18] CMS Collaboration “The CMS experiment at the CERN LHC” in: *JINST* 3 (2008), S08004 (cited on pages 10, 44).

[19] A. Altheimer et al. “Jet Substructure at the Tevatron and LHC: New results, new tools, new benchmarks” in: *J. Phys. G* 39 (2012), p. 063001 DOI: `10.1088/0954-3899/39/6/063001` arXiv:`1201.0008 [hep-ph]` (cited on page 10).

[20] Tilman Plehn, Gavin P. Salam, and Michael Spannowsky “Fat Jets for a Light Higgs” in: *Phys. Rev. Lett.* 104 (2010), p. 111801 DOI: `10.1103/PhysRevLett.104.111801` arXiv:`0910.5472 [hep-ph]` (cited on pages 10, 36, 142).

[21] Tilman Plehn et al. “Stop Reconstruction with Tagged Tops” in: *JHEP* 1010 (2010), p. 078 DOI: `10.1007/JHEP10(2010)078` arXiv:`1006.2833 [hep-ph]` (cited on pages 10, 36–38, 40, 142).

[22] Y.L. Dokshitzer et al. “Better Jet Clustering Algorithms” in: *JHEP* 9708 (1997), p. 001 DOI: `10.1088/1126-6708/1997/08/001` arXiv:`hep-ph/9707323` (cited on page 10).

[23] ATLAS Collaboration "Search for resonances decaying into top-quark pairs using fully hadronic decays in pp collisions with ATLAS at $\sqrt{s} = 7$ TeV" in: *JHEP* 1301 (2013), p. 116 DOI: `10.1007/JHEP01(2013)116` arXiv:`1211.2202 [hep-ex]` (cited on pages 11, 141).

[24] Kaustubh Agashe et al. "LHC Signals from Warped Extra Dimensions" in: *Phys. Rev. D* 77 (2008), p. 015003 DOI: `10.1103/PhysRevD.77.015003` arXiv:`0612015 [hep-ph]` (cited on pages 11, 32, 33, 107, 136).

[25] Ben Lillie, Lisa Randall, and Lian-Tao Wang "The Bulk RS KK-gluon at the LHC" in: *JHEP* 0709 (2007), p. 074 DOI: `10.1088/1126-6708/2007/09/074` arXiv:`hep-ph/0701166 [hep-ph]` (cited on pages 11, 32, 107, 136).

[26] Ben Lillie, Jing Shu, and Timothy M.P. Tait "Kaluza-Klein Gluons as a Diagnostic of Warped Models" in: *Phys. Rev. D* 76 (2007), p. 115016 DOI: `10.1103/PhysRevD.76.115016` arXiv:`0706.3960 [hep-ph]` (cited on pages 11, 32, 136).

[27] Antonio Pich "The Standard model of electroweak interactions" 2007 arXiv:`0705.4264 [hep-ph]` (cited on page 13).

[28] S.F. Novaes "Standard model: An Introduction" 1999 arXiv:`hep-ph/0001283 [hep-ph]` (cited on page 13).

[29] J. Goldstone "Field Theories with Superconductor Solutions" in: *Nuovo Cim.* 19 (1961), pp. 154–164 DOI: `10.1007/BF02812722` (cited on page 19).

[30] Antonio Pich "Aspects of quantum chromodynamics" 1999 arXiv:`hep-ph/0001118 [hep-ph]` (cited on page 21).

[31] Sven-Olaf Moch and Klaus Rabbertz "Physics at the Terascale" in: *Physics at the Terascale* Wiley-VCH, 2011 chap. Hard QCD: Still Going Strong DOI: `10.1002/9783527634965.ch4` (cited on page 21).

[32] John M. Campbell, J.W. Huston, and W.J. Stirling "Hard Interactions of Quarks and Gluons: A Primer for LHC Physics" in: *Rept. Prog. Phys.* 70 (2007), p. 89 DOI: `10.1088/0034-4885/70/1/R02` arXiv:`hep-ph/0611148 [hep-ph]` (cited on page 21).

[33] George Sterman, John Smith, John C. Collins, et al. "Handbook of perturbative QCD" in: *Rev. Mod. Phys.* 67 (1 Jan. 1995), pp. 157–248 DOI: `10.1103/RevModPhys.67.157` (cited on page 21).

[34] Murray Gell-Mann "Quarks" in: *Acta Phys. Austriaca Suppl.* 9 (1972), pp. 733–761 (cited on page 23).

[35] M.Y. Han and Yoichiro Nambu "Three Triplet Model with Double SU(3) Symmetry" in: *Phys. Rev. B.* 139 (1965), pp. 1006–1010 DOI: `10.1103/PhysRev.139.B1006` (cited on page 23).

[36] A.D. Martin et al. "Parton distributions for the LHC" in: *Eur. Phys. J. C* 63 (2009), pp. 189–285 DOI: `10.1140/epjc/s10052-009-1072-5` arXiv:`0901.0002 [hep-ph]` (cited on pages 27, 28, 69).

[37] J. Pumplin et al. "New generation of parton distributions with uncertainties from global QCD analysis" in: *JHEP* 0207 (2002), p. 012 DOI: `10.1088/1126-6708/2002/07/012` (cited on pages 27, 69, 130).

[38] NNPDF Collaboration "Unbiased global determination of parton distributions and their uncertainties at NNLO and at LO" in: *Nucl. Phys. B* 855 (2012), pp. 153–221 DOI: `10.1016/j.nuclphysb.2011.09.024` arXiv:`1107.2652 [hep-ph]` (cited on pages 27, 122).

[39] H1 and ZEUS Collaborations "Combined measurement and QCD analysis of the inclusive $e^{\pm}p$ scattering cross sections at HERA" in: *JHEP* 2010 (1 2010), pp. 1–63 DOI: `10.1007/JHEP01(2010)109` (cited on page 27).

[40] Stephen P. Martin "A Supersymmetry primer" 1997 arXiv:`hep-ph/9709356 [hep-ph]` (cited on page 28).

[41] Christopher T. Hill and Elizabeth H. Simmons "Strong dynamics and electroweak symmetry breaking" in: *Phys. Rept.* 381 (2003), pp. 235–402 DOI: `10.1016/S0370-1573(03)00140-6` arXiv:`hep-ph/0203079 [hep-ph]` (cited on page 29).

[42] Nima Arkani-Hamed, Savas Dimopoulos, and G.R. Dvali "The Hierarchy problem and new dimensions at a millimeter" in: *Phys. Lett. B* 429 (1998), pp. 263–272 DOI: `10.1016/S0370-2693(98)00466-3` arXiv:`hep-ph/9803315 [hep-ph]` (cited on page 29).

[43] Lisa Randall and Raman Sundrum "A Large mass hierarchy from a small extra dimension" in: *Phys. Rev. Lett.* 83 (1999), pp. 3370–3373 DOI: `10.1103/PhysRevLett.83.3370` arXiv:`hep-ph/9905221 [hep-ph]` (cited on pages 29, 31).

[44] Christopher T. Hill "Topcolor assisted technicolor" in: *Phys. Lett. B* 345.4 (1995), pp. 483 –489 DOI: `10.1016/0370-2693(94)01660-5` (cited on page 29).

[45] Christopher T. Hill "Topcolor: Top quark condensation in a gauge extension of the standard model" in: *Phys. Lett. B* 266 (1991), pp. 419–424 DOI: `10.1016/0370-2693(91)91061-Y` (cited on page 29).

[46] William A. Bardeen, Christopher T. Hill, and Manfred Lindner
"Minimal dynamical symmetry breaking of the standard model"
in: *Phys. Rev. D* 41 (5 Mar. 1990), pp. 1647–1660
DOI: `10.1103/PhysRevD.41.1647`
URL: `http://link.aps.org/doi/10.1103/PhysRevD.41.1647`
(cited on page 29).

[47] Robert M. Harris, Christopher T. Hill, and Stephen J. Parke
"Cross-section for topcolor Z' decaying to $t\bar{t}$: Version 2.6" 1999
arXiv:`hep-ph/9911288 [hep-ph]` (cited on pages 30, 107).

[48] Bogdan A. Dobrescu and Christopher T. Hill
"Electroweak symmetry breaking via top condensation seesaw"
in: *Phys. Rev. Lett.* 81 (1998), pp. 2634–2637
DOI: `10.1103/PhysRevLett.81.2634` arXiv:`hep-ph/9712319 [hep-ph]`
(cited on page 30).

[49] R. Sekhar Chivukula et al.
"Top quark seesaw theory of electroweak symmetry breaking"
in: *Phys. Rev. D* 59 (1999), p. 075003 DOI: `10.1103/PhysRevD.59.075003`
arXiv:`hep-ph/9809470 [hep-ph]` (cited on page 30).

[50] Gerhard Buchalla et al.
"GIM violation and new dynamics of the third generation"
in: *Phys. Rev. D* 53 (1996), pp. 5185–5200 DOI: `10.1103/PhysRevD.53.5185`
arXiv:`hep-ph/9510376 [hep-ph]` (cited on page 30).

[51] T. Kaluza "Zum Unitätsproblem der Physik"
in: *Sitz. Preuss. Akad. Wiss. Phys. Math. K* 1 (1921), p. 966 (cited on page 30).

[52] O. Klein "Quantentheorie und fünfdimensionale Relativitätstheorie"
in: *Zeitschrift für Physik* 37.12 (1926), pp. 895–906 (cited on page 30).

[53] Lisa Randall and Raman Sundrum "An Alternative to compactification"
in: *Phys. Rev. Lett.* 83 (1999), pp. 4690–4693
DOI: `10.1103/PhysRevLett.83.4690` arXiv:`hep-th/9906064 [hep-th]`
(cited on page 31).

[54] Gerald C. Blazey et al. "Run II jet physics" 2000
arXiv:`hep-ex/0005012 [hep-ex]` (cited on pages 32–34).

[55] (Ed.) Berger Edmond L.
"Research directions for the decade. Proceedings, 1990 Summer Study on High-Energy Physics, Snowmass, USA, June 25 - July 13, 1990" 1992
(cited on pages 34, 73).

[56] G. P. Salam and G. Soyez
"A practical Seedless Infrared-Safe Cone jet algorithm"
in: *JHEP* 0705 (2007), p. 086 arXiv:`hep-ph/0704.0292` (cited on pages 34, 35).

[57] M. Cacciari, G. P. Salam, and G. Soyez "The anti-k_t Jet Clustering Algorithm"
in: *JHEP* 0804 (2008), p. 063 arXiv:`hep-ph/0802.1189`
(cited on pages 34–36, 73, 75).

[58] Stephen D. Ellis and Davison E. Soper
"Successive combination jet algorithm for hadron collisions"
in: *Phys. Rev. D* 48 (1993), pp. 3160–3166 DOI: `10.1103/PhysRevD.48.3160`
arXiv:`hep-ph/9305266 [hep-ph]` (cited on page 35).

[59] S. Catani et al.
"Longitudinally invariant K_t clustering algorithms for hadron hadron collisions"
in: *Nucl. Phys. B* 406 (1993), pp. 187–224
DOI: `10.1016/0550-3213(93)90166-M` (cited on page 35).

[60] Yuri L. Dokshitzer et al. "Better jet clustering algorithms"
in: *JHEP* 9708 (1997), p. 001 arXiv:`hep-ph/9707323 [hep-ph]`
(cited on pages 35, 38).

[61] Tilman Plehn and Michael Spannowsky "Top Tagging"
in: *J. Phys. G* 39 (2012), p. 083001 DOI: `10.1088/0954-3899/39/8/083001`
arXiv:`1112.4441 [hep-ph]` (cited on page 35).

[62] CDF Collaboration "Studying the Underlying Event in Drell-Yan and High Transverse Momentum Jet Production at the Tevatron"
in: *Phys. Rev. D* 82 (2010), p. 034001 DOI: `10.1103/PhysRevD.82.034001`
arXiv:`1003.3146 [hep-ex]` (cited on pages 37, 69).

[63] S. Catani et al.
"Longitudinally-invariant k_t-clustering algorithms for hadron-hadron collisions"
in: *Nucl. Phys. B* 406.1–2 (1993) DOI: `10.1016/0550-3213(93)90166-M`
(cited on page 38).

[64] CDF Tevatron Electroweak Working Group and D0 Collaborations
"Combination of CDF and D0 results on the mass of the top quark using up to 5.8 fb-1 of data" 2011 arXiv:`1107.5255 [hep-ex]` (cited on page 38).

[65] ATLAS Collaboration "Jet energy measurement with the ATLAS detector in proton-proton collisions at $\sqrt{s} = 7$ TeV" in: *Submitted to Eur. Phys. J. C* (2011)
arXiv:`1112.6426 [hep-ex]` (cited on pages 40, 66, 109).

[66] Sebastian Schätzel "Calibration of HEPTopTagger Jets in ATLAS"
tech. rep. ATL-COM-PHYS-2012-1461 Oct. 2012
URL: `https://cdsweb.cern.ch/record/1483209` (cited on pages 40, 122).

[67] David Sosa "HEPTopTagger Parameter Optimization"
Master Thesis, Universität Heidelberg, 2012
URL: `http://www.physi.uni-heidelberg.de/Publications/`
(cited on pages 40, 102).

[68] D0 Collaboration "A Recipe for the construction of confidence limits"
in: *FERMILAB-TM-2104* (2000) (cited on page 41).

[69] R.J. Barlow
"Statistics: A Guide to the Use of Statistical Methods in the Physical Sciences"
Manchester Physics Series John Wiley & Sons, 1994 (cited on page 41).

[70] CERN - AC Team "The four main LHC experiments" June 1999
URL: `http://cdsweb.cern.ch/record/40525` (cited on page 43).

[71] Helmut Burkhardt, Dalahaye Jean-Pierrre, and Geschonke Günther "Physics at the Terascale" in: *Physics at the Terascale* Wiley-VCH, 2011 chap. Accelerators: the Particle Smashers DOI: `10.1002/9783527634965.ch4` (cited on page 44).

[72] ALEPH Collaboration "ALEPH: A detector for electron-positron annnihilations at LEP" in: *Nucl. Instrum. Meth. A* 294 (1990), pp. 121–178 DOI: `10.1016/0168-9002(90)91831-U` (cited on page 44).

[73] DELPHI Collaboration "The DELPHI detector at LEP" in: *Nucl. Instrum. Meth. A* 303 (1991), pp. 2330–276 DOI: `10.1016/0168-9002(91)90793-P` (cited on page 44).

[74] LEP Working Group for Higgs boson searches "Search for the standard model Higgs boson at LEP" in: *Phys. Lett. B* 565 (2003), pp. 61–75 DOI: `10.1016/S0370-2693(03)00614-2` arXiv:`hep-ex/0306033 [hep-ex]` (cited on page 44).

[75] CDF and D0 Collaborations and the Tevatron New Physics and Higgs Working Group "Updated Combination of CDF and D0 Searches for Standard Model Higgs Boson Production with up to 10.0 fb^{-1} of Data" 2012 arXiv:`1207.0449 [hep-ex]` (cited on page 44).

[76] LEP/TEV Electroweak Working Group "Plots for Winter 2012" [Online; accessed 13-December-2012] 2012 URL: `http://lepewwg.web.cern.ch/LEPEWWG/plots/winter2012/` (cited on page 44).

[77] LHCb Collaboration "The LHCb Detector at the LHC" in: *JINST* 3.08 (2008), S08005 (cited on page 44).

[78] LHCb Collaboration "First evidence for the decay $B_s \to \mu^+\mu^-$" in: (2012) arXiv:`1211.2674 [hep-ex]` (cited on page 44).

[79] ALICE Collaboration "The ALICE experiment at the CERN LHC" in: *JINST* 3.08 (2008), S08002 (cited on page 44).

[80] Peter Braun-Munzinger and Johanna Stachel "The quest for the quark-gluon plasma" in: *Nature* 448 (2007), pp. 302–309 DOI: `10.1038/nature06080` (cited on page 44).

[81] Wikipedia "CERN accelerator complex — Wikipedia, The Free Encyclopedia" 2011 URL: `http://en.wikipedia.org/wiki/File:Cern-accelerator-complex.svg` (visited on 02/11/2013) (cited on page 45).

[82] Klaus Hanke, Michel Chanel, and Karlheinz Schindl "The PS Booster hits 40" in: *CERN Courier* 52 (7 2012) URL: `http://cerncourier.com/cws/article/cern/50562` (cited on page 44).

[83] Günther Plass "CERN's heart beats as strong as ever" in: *CERN Courier* 44 (1 2011) URL: `http://cerncourier.com/cws/article/cern/29009` (cited on page 45).

[84] G. Acquistapace et al. "The CERN neutrino beam to Gran Sasso (NGS)" tech. rep. CERN-98-02, INFN-AE-98-05, CERN-YELLOW-98-02 1998 (cited on page 45).

[85] CERN - AC Team "Diagram of an LHC dipole magnet. Schéma d'un aimant dipôle du LHC" June 1999 URL: `http://cdsweb.cern.ch/record/40524` (cited on page 46).

[86] "Summary of the analysis of the 19 September 2008 incident at the LHC." tech. rep. Geneva: CERN, Oct. 2008 URL: `http://cdsweb.cern.ch/record/1135729/` (cited on page 47).

[87] ATLAS Collaboration "Improved Luminosity Determination in *pp* Collisions at $\sqrt{s}$=7 TeV using the ATLAS Detector at the LHC" in: *ATLAS-CONF-2012-080* (2012) URL: `https://atlas.web.cern.ch/Atlas/GROUPS/PHYSICS/CONFNOTES/ATLAS-CONF-2012-080/` (cited on pages 47, 62, 68, 124).

[88] ATLAS Collaboration "Luminosity Public Results" 2012 URL: `https://twiki.cern.ch/twiki/bin/view/AtlasPublic/LuminosityPublicResults` (visited on 11/15/2012) (cited on pages 48, 49).

[89] ATLAS - Joao Pequenao "Computer generated image of the whole ATLAS detector" Mar. 2008 URL: `https://cdsweb.cern.ch/record/1095924` (cited on page 52).

[90] ATLAS - Joao Pequenao "Computer generated image of the ATLAS inner detector" Mar. 2008 URL: `https://cdsweb.cern.ch/record/1095926` (cited on pages 53, 54).

[91] ATLAS - Joao Pequenao "Computer generated image of the ATLAS calorimeter" Mar. 2008 URL: `http://cdsweb.cern.ch/record/1095927` (cited on page 56).

[92] ATLAS - Joao Pequenao "Computer generated image of the ATLAS calorimeter" Mar. 2008 URL: `http://cdsweb.cern.ch/record/1095929` (cited on page 60).

[93] ATLAS Collaboration "Luminosity determination in pp collisions at $\sqrt{s} = 7$ TeV using the ATLAS detector at the LHC" in: *Eur. Phys. J. C* 71 (2011), p. 1630 arXiv:`1101.0070 [hep-ex]` (cited on pages 62, 68).

[94] ATLAS Collaboration "Expected Performance of the ATLAS Experiment - Detector, Trigger and Physics" 2009 arXiv:`0901.0512 [hep-ex]` (cited on pages 64, 73).

[95] ATLAS Collaboration "Performance of the ATLAS Inner Detector Track and Vertex Reconstruction in the High Pile-Up LHC Environment" tech. rep. ATLAS-CONF-2012-042 Geneva: CERN, Mar. 2012 URL: `http://cdsweb.cern.ch/record/1435196` (cited on page 64).

[96] W Lampl et al. "Calorimeter clustering algorithms: description and performance" in: *ATL-LARG-PUB-2008-002* (Apr. 2008) (cited on page 66).

[97] Matteo Cacciari and Gavin P. Salam
"Dispelling the N^3 myth for the k_t jet-finder"
in: *Phys. Lett. B* 641 (2006), pp. 57–61
DOI: `10.1016/j.physletb.2006.08.037` arXiv:`0802.1189 [hep-ph]`
(cited on page 66).

[98] Matteo Cacciari, Gavin P. Salam, and Gregory Soyez "FastJet"
`http://fastjet.fr` (cited on page 66).

[99] ATLAS Collaboration
"Properties of Jets and Inputs to Jet Reconstruction and Calibration with the ATLAS Detector Using Proton-Proton Collisions at $\sqrt{s} = 7$ TeV"
in: *ATLAS-CONF-2010-053* (2010) (cited on page 66).

[100] ATLAS Collaboration "Commissioning of the ATLAS high-performance b-tagging algorithms in the 7 TeV collision data" tech. rep. URL:
`https://atlas.web.cern.ch/Atlas/GROUPS/PHYSICS/CONFNOTES/ATLAS-CONF-2011-102/` (cited on page 67).

[101] ATLAS Collaboration "Measurement of the b-tag Efficiency in a Sample of Jets Containing Muons with 5 fb^{-1} of Data from the ATLAS Detector" tech. rep.
URL:
`https://atlas.web.cern.ch/Atlas/GROUPS/PHYSICS/CONFNOTES/ATLAS-CONF-2012-043/` (cited on pages 67, 68, 109, 120, 121).

[102] ATLAS Collaboration "Performance of Missing Transverse Momentum Reconstruction in ATLAS with 2011 Proton-Proton Collisions at $\sqrt{s} = 7$ TeV"
tech. rep. ATLAS-CONF-2012-101 2012
URL: `https://cds.cern.ch/record/1463915` (cited on page 67).

[103] Torbjorn Sjostrand, Stephen Mrenna, and Peter Z. Skands
"PYTHIA 6.4 Physics and Manual" in: *JHEP* 05 (2006), p. 026
arXiv:`hep-ph/0603175` (cited on pages 69, 70, 88, 107, 123).

[104] Michelangelo L. Mangano et al.
"ALPGEN, a generator for hard multiparton processes in hadronic collisions"
in: *JHEP* 2003.07 (2003), p. 001 (cited on page 69).

[105] Johan Alwall et al. "MadGraph/MadEvent v4: The New Web Generation"
in: *JHEP* 0709 (2007), p. 028 DOI: `10.1088/1126-6708/2007/09/028`
arXiv:`0706.2334 [hep-ph]` (cited on page 69).

[106] S. Frixione and B.R. Webber
"Matching NLO QCD computations and parton shower simulations"
in: *JHEP* 0206 (2002), p. 029 eprint: `hep-ph/0204244` (cited on page 69).

[107] S. Frixione and P. Nason and B.R. Webber
"Matching NLO QCD and parton showers in heavy flavour production"
in: *JHEP* 0308 (2003), p. 007 eprint: `hep-ph/0305252` (cited on page 69).

[108] Hung-Liang Lai et al. "New parton distributions for collider physics"
in: *Phys. Rev. D* 82 (2010), p. 074024 DOI: `10.1103/PhysRevD.82.074024`
arXiv:`1007.2241 [hep-ph]` (cited on pages 69, 122, 130).

[109] G. Corcella et al. "HERWIG 6.5 release note" 2002 arXiv:`0210213 [hep-ph]` (cited on page 69).

[110] J. M. Butterworth, Jeffrey R. Forshaw, and M. H. Seymour "Multiparton interactions in photoproduction at HERA" in: *Z. Phys. C* 72 (1996), pp. 637–646 DOI: `10.1007/s002880050286` arXiv:`hep-ph/9601371` (cited on page 69).

[111] M. Aliev et al. "HATHOR: HAdronic Top and Heavy quarks crOss section calculatoR" in: *Comput. Phys. Commun.* 182 (2011), pp. 1034–1046 DOI: `10.1016/j.cpc.2010.12.040` arXiv:`1007.1327 [hep-ph]` (cited on page 69).

[112] Jun Gao et al. "Next-to-leading order QCD corrections to the heavy resonance production and decay into top quark pair at the LHC" in: *Phys. Rev. D* 82 (2010), p. 014020 DOI: `10.1103/PhysRevD.82.014020` arXiv:`1004.0876 [hep-ph]` (cited on pages 69, 136).

[113] S. Agostinelli et al. "Geant4 – A Simulation Toolkit" in: *Nucl. Instr. and Meth.* A506 (2003), p. 250 (cited on page 70).

[114] ATLAS Collaboration "ATLAS Simulation Infrastructure" in: *Eur. Phys. J. C* 70 (2010), p. 823 arXiv:`1005.4568 [hep-ph]` (cited on page 70).

[115] "ATLAS tunes of PYTHIA 6 and Pythia 8 for MC11" tech. rep. ATL-PHYS-PUB-2011-009 Geneva: CERN, July 2011 URL: `http://cdsweb.cern.ch/record/1363300` (cited on page 70).

[116] Peter Jenni et al. "ATLAS high-level trigger, data-acquisition and controls: Technical Design Report" Technical Design Report ATLAS Geneva: CERN, 2003 URL: `https://cds.cern.ch/record/616089` (cited on page 73).

[117] L Ancu et al. "The Design and Performance of the ATLAS Jet Trigger for the Event Filter" tech. rep. ATL-COM-DAQ-2011-048 Geneva: CERN, June 2011 URL: `https://cds.cern.ch/record/1357014` (cited on pages 73, 74, 91).

[118] "Data-Quality Requirements and Event Cleaning for Jets and Missing Transverse Energy Reconstruction with the ATLAS Detector in Proton-Proton Collisions at a Center-of-Mass Energy of $\sqrt{s} = 7$ TeV" tech. rep. ATLAS-CONF-2010-038 Geneva: CERN, July 2010 URL: `https://cds.cern.ch/record/1277678` (cited on page 76).

[119] ATLAS Collaboration "Performance of large-R jets and jet substructure reconstruction with the ATLAS detector" in: *ATLAS-CONF-2012-065* (June 2012) (cited on page 93).

[120] "Selection of jets produced in proton-proton collisions with the ATLAS detector using 2011 data" tech. rep. ATLAS-CONF-2012-020 Geneva: CERN, Mar. 2012 URL: `https://cdsweb.cern.ch/record/1430034` (cited on page 93).

[121] CDF Collaboration "Limits on the production of narrow $t\bar{t}$ resonances in $p\bar{p}$ collisions at $\sqrt{s} = 1.96$ TeV" in: *Phys. Rev. D* 77 (2008), p. 051102 DOI: `10.1103/PhysRevD.77.051102` arXiv:`0710.5335 [hep-ex]` (cited on page 107).

[122] CDF Collaboration "Search for resonant $t\bar{t}$ production in $p\bar{p}$ collisions at $\sqrt{s} = 1.96$ TeV" in: *Phys. Rev. Lett.* 100 (2008), p. 231801 DOI: `10.1103/PhysRevLett.100.231801` arXiv:`0709.0705 [hep-ex]` (cited on page 107).

[123] D0 Collaboration "Search for $t\bar{t}$ resonances in the lepton plus jets final state in $p\bar{p}$ collisions at $\sqrt{s} = 1.96$ TeV" in: *Phys. Lett. B* 668 (2008), pp. 98–104 DOI: `10.1016/j.physletb.2008.08.027` arXiv:`0804.3664 [hep-ex]` (cited on page 107).

[124] CDF Collaboration "Search for New Color-Octet Vector Particle Decaying to $t\bar{t}$ in $p\bar{p}$ Collisions at $\sqrt{s} = 1.96$ TeV" in: *Phys. Lett. B* 691 (2010), pp. 183–190 DOI: `10.1016/j.physletb.2010.06.036` arXiv:`0911.3112 [hep-ex]` (cited on page 107).

[125] CDF Collaboration "A search for resonant production of $t\bar{t}$ pairs in 4.8 fb^{-1} of integrated luminosity of $p\bar{p}$ collisions at $\sqrt{s} = 1.96$ TeV" in: *Phys. Rev. D* 84 (2011), p. 072004 DOI: `10.1103/PhysRevD.84.072004` arXiv:`1107.5063 [hep-ex]` (cited on page 107).

[126] D0 Collaboration "Search for a Narrow $t\bar{t}$ Resonance in $p\bar{p}$ Collisions at $\sqrt{s} = 1.96$ TeV" in: *Phys. Rev. D* 85 (2012), p. 051101 DOI: `10.1103/PhysRevD.85.051101` arXiv:`1111.1271 [hep-ex]` (cited on page 107).

[127] ATLAS Collaboration "A search for $t\bar{t}$ resonances with the ATLAS detector in 2.05 fb^{-1} of proton-proton collisions at $\sqrt{s} = 7$ TeV" in: *Eur.Phys.J.* C72 (2012), p. 2083 DOI: `10.1140/epjc/s10052-012-2083-1` arXiv:`1205.5371 [hep-ex]` (cited on pages 107, 141).

[128] ATLAS Collaboration "A search for $t\bar{t}$ resonances in lepton+jets events with highly boosted top quarks collected in pp collisions at $\sqrt{s} = 7$ TeV with the ATLAS detector" in: (2012)Submitted to JHEP arXiv:`1207.2409 [hep-ex]` (cited on pages 107, 141).

[129] CMS Collaboration "Search for anomalous $t\bar{t}$ production in the highly-boosted all-hadronic final state" in: *JHEP* 1209 (2012), p. 029 DOI: `10.1007/JHEP09(2012)029` arXiv:`1204.2488 [hep-ex]` (cited on page 107).

[130] ATLAS "Measurement of the Mistag Rate of b-tagging algorithms with 5 fb^{-1} of Data Collected by the ATLAS Detector" tech. rep. ATL-CONF-2012-040 Geneva: CERN, Mar. 2012 URL: `https://atlas.web.cern.ch/Atlas/GROUPS/PHYSICS/CONFNOTES/ATLAS-CONF-2012-040/` (cited on pages 109, 120).

[131] ATLAS Collaboration “Measuring the b-tag efficiency in a top-pair sample with 4.7 fb^{-1} of data from the ATLAS detector” tech. rep. URL: `https://atlas.web.cern.ch/Atlas/GROUPS/PHYSICS/CONFNOTES/ATLAS-CONF-2012-097/` (cited on pages 120, 121).

[132] Sebastian Schätzel “Jet p_T resolution for HEPTopTagger Jets in ATLAS” tech. rep. ATL-COM-PHYS-2012-1463 Oct. 2012 URL: `https://cdsweb.cern.ch/record/1483229` (cited on page 122).

[133] J. Pumplin et al. “New Generation of Parton Distributions with Uncertainties from Global QCD Analysis” in: *JHEP* 0207 (2002), p. 012 arXiv:`hep-ph/0201195` (cited on page 122).

[134] Michiel Botje et al. “The PDF4LHC Working Group Interim Recommendations” 2011 arXiv:`1101.0538 [hep-ph]` (cited on page 122).

[135] A.D. Martin et al. “Uncertainties on α_S in global PDF analyses and implications for predicted hadronic cross sections” in: *Eur. Phys. J. C* 64 (2009), pp. 653–680 DOI: `10.1140/epjc/s10052-009-1164-2` arXiv:`0905.3531v2 [hep-ph]` (cited on page 122).

[136] ATLAS Collaboration “Determination of the strange quark density of the proton from ATLAS measurements of the $W \to l\nu$ and $Z \to ll$ cross sections” in: *Phys. Rev. Lett.* 109 (2012), p. 012001 DOI: `10.1103/PhysRevLett.109.012001` arXiv:`1203.4051 [hep-ex]` (cited on page 123).

[137] ATLAS Collaboration “Measurement of the inclusive jet cross section in pp collisions at $\sqrt{s} = 2.76$ TeV and comparison to the inclusive jet cross section at $\sqrt{s} = 7$ TeV using the ATLAS detector” tech. rep. 2012 URL: `https://cds.cern.ch/record/1477535` (cited on page 123).

[138] Borut Paul Kersevan and Elzbieta Richter-Was “The Monte Carlo event generator AcerMC version 2.0 with interfaces to PYTHIA 6.2 and HERWIG 6.5” 2004 arXiv:`hep-ph/0405247` (cited on page 123).

[139] Aneesh V. Manohar and Michael Trott “Electroweak Sudakov Corrections and the Top Quark Forward-Backward Asymmetry” in: *Phys. Lett. B* 711 (2012), pp. 313–316 DOI: `10.1016/j.physletb.2012.04.013` arXiv:`1201.3926 [hep-ph]` (cited on page 125).

[140] Kiran Joshi, Andrew D. Pilkington, and Michael Spannowsky “The dependency of boosted tagging algorithms on the event colour structure” in: *Phys. Rev. D* 86 (2012), p. 114016 DOI: `10.1103/PhysRevD.86.114016` arXiv:`1207.6066 [hep-ph]` (cited on page 126).

[141] Torbjorn Sjostrand, Stephen Mrenna, and Peter Z. Skands "A Brief Introduction to PYTHIA 8.1" in: *Comput. Phys. Commun.* 178 (2008), pp. 852–867 DOI: `10.1016/j.cpc.2008.01.036` arXiv:`0710.3820 [hep-ph]` (cited on page 136).

[142] Leandro G. Almeida et al. "Template overlap method for massive jets" in: *Phys. Rev. D* 82 (5 Sept. 2010), p. 054034 DOI: `10.1103/PhysRevD.82.054034` arXiv:`hep-ph/1006.2035` (cited on page 141).

[143] L. G. Almeida et al. "Three-particle templates for boosted Higgs" 2011 arXiv:`1112.1957 [hep-ph]` (cited on page 141).